POLITECNICO DI MILANO

Facoltà di Ingegneria Industriale e dell'Informazione

Corso di Laurea in Ingegneria Fisica

Tesi di laurea magistrale

TOWARDS A MAGNETORESISTIVE PLATFORM FOR DETECTION OF DNA PATHOGENS IN AGRIFOOD INDUSTRIES

Relatore:
Dott.ssa Daniela PETTI

Correlatore:
Prof. Riccardo BERTACCO

Candidato:
Chiara LA TORRE
matr. 771182

Anno Accademico 2012-2013

Contents

Sommario xvi

Abstract xix

1 Introduction 1

1.1 Biosensors . . . 1
1.2 Lab on a chip . . . 3
1.3 Biomolecular recognition experiments . . . 4
1.3.1 Detection methods . . . 5
1.3.2 Limit of Detection and the Polymerase Chain Reaction 11
1.4 Magnetoresistive biosensors . . . 13
1.5 Thesis project . . . 17
1.6 Thesis outlook . . . 18

2 Magnetic Biosensors 20

2.1 MTJ sensors . . . 21
2.1.1 Jullier's model . . . 22
2.1.2 I-V characteristic . . . 24
2.1.3 Parameters influencing the TMR . . . 25
2.2 Sensor engineering . . . 28
2.2.1 Exchange Bias . . . 29
2.2.2 Bilinear Coupling . . . 30
2.2.3 Néel Coupling . . . 35
2.3 Linearization of a MTJ sensor . . . 36
2.3.1 Parallel and crossed anisotropies . . . 37
2.3.2 Superparamagnetism . . . 40
2.4 MTJ Sensor Noise . . . 43

3 Experimental methods **46**
3.1 Instruments and methods for sample preparation 46
3.1.1 AJA Magnetron Sputtering 46
3.1.2 Optical Litography 50
3.1.3 Ion Beam Etching 54
3.1.4 Electron beam evaporator 56
3.1.5 Field Annealing 57
3.1.6 Process flow 58
3.2 Sample characterization 66
3.2.1 Atomic Force Microscopy 66
3.2.2 Vibrating Sample Magnetometer 68
3.2.3 Magneto-Optic Kerr Effect 70
3.2.4 TMR Measurements 72
3.2.5 Noise Measurements 74
3.3 Biological experiments 75
3.3.1 Instrumental apparatus 75
3.3.2 Methods 78

4 Platform layout **82**
4.1 Sample holder and microchip 86
4.2 The Electromagnet 91
4.3 Microfluidic cell 93
4.4 Electronic platform 97

5 Sensors optimization and characterization **99**
5.1 Sensor's optimization 100
5.1.1 Roughness optimization of the substrate and MgO . . 100
5.1.2 Exchange Bias 103
5.1.3 Optimization of the Synthetic antiferromagnet 104
5.2 Sensors characterization 113
5.3 Noise vs MgO thickness 123
5.4 Summary 130

6 Biological experiments **132**
6.1 Study of bio-functionalized surfaces labeled with magnetic nanospheres 132
6.2 Biomolecular recognition with magnetic sensors 140

6.2.1 Beads detection 141
6.2.2 Molecular recognition of synthetic DNA 143
6.2.3 Molecular recognition of Hepatitis E virus 148
6.3 Summary 152

Conclusions and perspectives **153**

Bibliography **155**

List of Figures

1.1 (a) Graph of the publications in biosensors during the period from 1980 to 2011; (b) Graph of the world market for biosensors estimated from various commercial sources and predicted for the future in US$ millions. [2] 1
1.2 (a) All-printed biosensing system: glucose concentration can be measured in few seconds and observed via the printed display; (b) Implantable biosensors for continuous glucose monitoring [1]. 2
1.3 (a) A schematic of the hybridization process. (b) Binding of markers to hybridized target DNA. 6
1.4 DNA microarray spotters producing thousand of spots on the surface. The amplified DNA strands are labeled with fluorophores and fuorescence scanner detects the light emitted by the labels; the different colours indicate that different biomolecules have been detected. 8
1.5 Sketch of magnetic bead formed by magnetic nanoparticles in a non-magnetic matrix/shell. 10
1.6 Schematic representation of the two different procedures for magnetic labeling of hybridization events: post-hybridization and pre-hybridization magnetic labeling. In the former, first probe DNA is immobilized (1), then target DNA hybridizes (2) and finally labeling of pre-hybridized target DNA occurs. In the latter, first target DNA and magnetic particles are concentrated (1) in order to enable streptavidin-biotin bonds (2), then the labels coated by target DNA are placed onto the sensor so that hybridization occurs (3). 13

1.7 Schematic representation of the detection process of a magnetic bead: when an external field is applied the bead is magnetized and the MR sensor detects the fringe field generated from it. 14
1.8 Probe length and packing configuration influencing biotin-streptavidin binding. 16

2.1 Tunneling current flowing perpendicular to the layers of a MTJ. 21
2.2 Valence bands illustration of spin-dependent tunneling across an insulating barrier, in case of antiparallel and parallel alignment. The arrows in the boxes show the majority spin in the two electrodes. 23
2.3 I-V characteristics at T = 13 K for a tunnel junction of the type CrO_2/barrier layer/Co fitted to the Simmons model (solid black line) [10]. 25
2.4 MgO-thickness dependence of resistance-area (RA) product for parallel (R_P) and antiparallel (R_{AP}) configuration at T = 20 K for an epitaxial Fe/MgO/Fe junction. Adapted from[125]. 26
2.5 Typical stack of a TMR junction. 28
2.6 Schematic diagram of the spin configuration of a FM/AFM bilayer at the different stages (1-5) of an exchange biased hysteresis loop. 29
2.7 Critical spanning vectors for Cu in the 100 direction. The right panel shows a representation of the Cu Fermi surface and a rectangular slice (solid line) through it. The necks in the (111) directions are indicated in gray. The dashed lines indicate the bulk Brillouin zone. In the left panel, the rectangular slice from the right panel is repeated periodically. There, the heavy curves show the Fermi surface of Cu in that slice. The white arrow gives a 1-dimensional reciprocal lattice vector in the interface direction. The gray arrows give the critical spanning vectors (for both the long (l) and short (s) period). . 31

2.8 Quantum wells used to compute interlayer exchange coupling. On the right, the two panels give typical band structures for free electron models of interlayer exchange coupling. On the left, the four panels give the quantum wells for spin up and spin down electrons for parallel and antiparallel alignment of the magnetizations. 32
2.9 Evolution of quantum well resonances with spacer layer thickness. The lines are the bound states, and the fuzzy ellipses are the resonances for quantum wells of increasing thickness. . 33
2.10 In (a), total energy change due to a quantum well filled to the Fermi level. The solid line shows the energy, the dotted line shows the approximated form for large D in eq. 2.12. In (b), illustration of an integration of sinusoids with different periods. The peaks in the heavy curve come from constructive interference among some of the light curves [108]. 34
2.11 Orange peel coupling from correlated roughness. Fringe field and magnetic "charges" in case of a rough surface (a), of two separated magnetic layers with parallel magnetizations (low energy configuration) (b) and of two separated magnetic layers with antiparallel magnetizations (high energy configuration) (c) [14]. 35
2.12 Scheme of the sensor composed by a pinned layer and a free layer with (a) parallel anisotropies and (b) crossed anisotropies. 38
2.13 Transfer curves of the sensor in case of (a) parallel anisotropies and $H_k > N_{xx}M_s^f$, (b) parallel anisotropies and $H_k < N_{xx}M_s^f$, (c) crossed anisotropies. 40
2.14 (a) Magnetization flipping by thermal fluctuations; (b) observation window for having the particle blocking in one of its magnetic states; (c) $\log(\tau)$ versus $\frac{1}{T}$ for two values of particle volume V. 41
2.15 (a) Comparison between the curves M(H) of a paramagnet and a superparamagnet and (b) size effect on the magnetic behaviour for different materials [65]. 42

3.1 Schematic of the magnetron sputtering process. 47

3.2 Our AJA ATC Orion sputtering system. A is the deposition chamber, B the load-lock, C the transfer arm, D the generators which power the sources located under the deposition chamber [60]. 48
3.3 (a) Positive and negative resist after development. (b) Positive and negative resist exposure characteristics. 51
3.4 Mask aligner Karl Suss MA56. 52
3.5 The two final phases of the photolithographic process. 53
3.6 Inverse lithography process steps. 54
3.7 Visual method based on the use of flags for determining when to stop the etching. 55
3.8 Schematic of the ion beam etching experimental apparatus. . 56
3.9 Our high vacuum magnetic field annealing system. A is the turbopump; in B, connection for the thermocouple (white wire) and the filament (blue and red wires); C is the vacuometer controller, D is the DC current generator, E is the permanent magnet; F is the sample holder; G is the vacuometer. 57
3.10 (a) Mask pattern and (b) picture of the final device after the fabrication process. 59
3.11 3D view of the sputtered sensor stack after the lithographic patterning process. 60
3.12 MESA definition. Bottom contact areas of a) $20 \times 150\mu m^2$, b) $40 \times 150\mu m^2$. On the right, zoom of the optical microscope images for the two pattern. 62
3.13 Second step of lithography: junction definition. The SiO_2 is deposited everywhere except for the junctions and the bottom contacts (black features in the pattern). In the lower panel, zoomed images of optical microscope of the junction area a) $2.5 \times 30\mu m^2$, b) $2.5 \times 50\mu m^2$. 63
3.14 (a) Pattern of the third step of lithography. In the left panel the two kinds of contact areas are showed. (b) In the left panel a zoomed optical microscope image of the patterned structure before contacts deposition, and on the right a 3D view of the sensor. 64
3.15 3D view of one sensor after the lithographic process. 65

3.16 (a) Sketch of an AFM measuring process; (b) Our Veeco AFM system, where A is the optical camera for centering the desired sample zone and B is the core of the AFM, which includes the AFM tip, the laser and the partioned photodiode; C is the sample holder. 67
3.17 Tipical VSM measurement configuration. The facing down sample is put within a uniform magnetic field, generated by an elecromagnet, and a pair of pick-up coils. The sample is attached to a sample holder, that is connected to a mechanical system that makes the sample vibrate transversely. 68
3.18 Vibrating sample magnetometer (MicroSense Easy (EZ9)). A is the system sketched in figure 3.17, B the mechanical system that makes the sample vibrate, including an anti-vibration component to minimize the vibration noise, and C the generators, amplifiers, and computer interface. 70
3.19 Schematic configurations of the sample magnetization for the polar, longitudinal, and transverse magneto-optical Kerr effects. 71
3.20 Sketch of our longitudinal MOKE experimental setup. 71
3.21 (a) Sketch of a two point-system for TMR mesurements; (b) Two-points probe; (c) Photo of the sample placed between the poles of the electromagnet during the two-points measurement. 73
3.22 Working principle of a cross-correlation spectrum analyzer. . . 75
3.23 Circuit diagram of the instrumental apparatus used for the experiments of detection beads with a double modulation technique. In the inset (a) the multiplexer and series resistances of 1kΩ and (b) Vin and Vout with only one enable sensor. . . 76
3.24 (a) Optical microscope image of the chip containing 8 sensors and (b) zoom image of one sensor with the directions of the two components of the magnetic field; (c) sketch of the microfluidic system with also the electrical contact to the array of eight sensors. 77
3.25 Transfer curve R(H) of a TMR sensor grown at LNESS (MgO thickness = 1.23nm) (a) and second derivative of the forward half-loop (b). 80

4.1 Layout of the platform for magnetic biosensing including the microchip, electromagnet, microfluidics and front-end electronics. 82
4.2 Sketch of the optolithographic process for the selective biofunctionalization. 84
4.3 View of the microchip and of the sample holder with the integrated heater. 86
4.4 First step of lithography: (a) MESA definition for the 12 sensors and (b) zoomed image of the single structure. 87
4.5 (a) Pattern of the second step of lithography. For the sensor number 12, designed for the microchip's temperature control, this step is a reply of the first one. (b) zoomed image of the single pillar: junction size of $3 \times 40\mu m^2$. 88
4.6 Third step of lithography: contacts definition. 89
4.7 (a) 3D view of the patterned chip and (b) zoomed image of one sensor. 90
4.8 Sketch of the optolithographic process for the biofunctionalization of the sensors. 91
4.9 (a) Electromagnet with a horseshoe shape. All the dimensions are indicated. (b) On the left, side view of the distribution of the intensity of the magnetic field H calculated by FEMM; on the right, top view of the same distribution, only in the region of interest, where the sensors are positioned. The simulations and calculations have been carried out by Andrea Fogliani, for his thesis work [34]. 92
4.10 (a) Picture of the final electromagnet to be integrated into the platform. (b) Characterization curve of the electromagnet varying the current from -1.2 A to 1.2 A: a magnetic field of 50 Oe is obtained with a current of 300 mA. The electromagnet shows a remanence field of 10 Oe, which has to be compensated during all the calibrations and experiments, automatically via software. 93
4.11 Microfluidic system with the two chambers in polycarbonate. 94
4.12 Side and top view of the microfluidic system. All the dimensions are indicated. 95

4.13 (a) 3D representation of the microfluidic channel. Color map of the velocity (b) and of the shear stress (c) onto the sensors' surface (Courtesy of E. Bianchi, F. Nason and G. Dubini (CMIC)). 96
4.14 Schematic diagram of the electronic platform designed for the biological assay with the magnetoresistive sensors. 97
4.15 (a) Picture of the final electronic platform connected with our instrumental apparatus for the experiment of sedimentation beads: 1 is the electronic platform, 2 is the microfluidic system with the magnetic chip inserted between the poles of the electromagnet, 3 is the multiplexer, 4 the syringe pump. (b) Sedimentation beads signal which demonstrates the operation of the electronic platform. 98

5.1 AFM image and 3D view of MgO of Sample R1 (a), Sample R2 (b), Sample R3 (c) and Sample R4 (d). 102
5.2 Hysteresis loops (black dots) and fitting of the data (solid red line), for Ta(5nm)/Ru(18nm)/Ta(3nm)/IrMn(20nm)/CoFe(2nm)/Ru(1.3nm) before (a) and after (b) field cooling. 104
5.3 Hysteresis loops of SAF structures: Ta(5nm)/Ru(18nm)/Ta (3nm)/IrMn(20nm)/CoFe(2nm)/Ru(x)/CoFeB(3nm)/MgO(2nm), with different Ru thicknesses x=0.7 (a), 0.9 (c), 1.1 (b), 0.13 (d) nm, measured after a field annealing at T=300 °C. The arrows indicate the orientation of the magnetic moments of the two layers, CoFe and CoFeB. 106
5.4 (a) Definition of the angles with respect to the applied field H and the pinning direction of the bottom CoFe layer. (b) Variation of the angle of the bottom CoFe (blu line) and of the top CoFeB (red line) as a function of the applied field. (c) Hysteresis loop of SAF structure (Ru=0.9 nm), corresponding to the rotation of the magnetic moments depicted in the upper panel. 109
5.5 Hysteresis loops of SAF structures recorded by VSM: Ta(5nm)/Ru(18nm)/Ta (3nm)/IrMn(20nm)/CoFe(2nm)/Ru(0.9nm)/CoFeB (3nm)/MgO (2nm) annealed at 270 (a), 300 (b), 320 (c) °C. . 110

5.6 Hysteresis loops of SAF samples measured by VSM: Sample S1 (a), Sample S2 (b), Sample S3 (optimal condition) (c). . . 112
5.7 RA product versus junction area for Samples (a) 1, 2, 3, 4 (all with 2nm thick MgO) (b) 5, 6 (with 1.23nm thick MgO) (c) 7 (0.9nm thick MgO). 115
5.8 TMR ratios as a function of RA product for as-deposited Samples 1, 2, 3, 4, 5, 6 (a) and after annealing (all samples annealed at 300 °C except for Sample 6 annealed at 270 °C). (c) Average TMR ratios with the annealing temperature. 116
5.9 TMR ratios as a function of RA product for Sample 7 before (red squares) and after (blue squares) annealing at 300 °C. . . 118
5.10 TMR loops of the junctions which provided the highest TMR values: (a) Sample 1 (b) Sample 2 (c) Sample 3 (d) Sample 4 (e) Sample 5 (f) Sample 6. 119
5.11 TMR loops of the most performing junction of sample 7 in terms of coercivity and reduced stray field. 120
5.12 TMR loops of the sensors of sample 4 enabled for the experiment of molecular recognition (COCU). 122
5.13 (a) Noise power density V^2/Hz varying the current flowing through one sensor of Sample 1. All the other sensors are kept to ground; (b) Noise power density V^2/Hz, as a function of the current, measured at two different frequencies, 50 Hz and 10 kHz. 125
5.14 (a) Simplified model of the single sensor with the parasitic capacitances (C_{par}) and the substrate resistance ($R_{silicon}$). (b) Simplified model of a chip with only two sensors that have a common substrate. 126
5.15 Noise power density V^2/Hz varying the current flowing through Sample 7: (a) withouth applying magnetic field and (b) applying magnetic field (linear region of the transfer curve). For a direct comparisong the cases of 0 and 100μA in absence of magnetic field have been shown (black and gray curves). . . . 128

6.1 Fluorescence image of the sample spotted with Enterobacter faecalis. The bottom left part of the image, and the top right, show respectively the positive and negative control of the sample. . . . 134
6.2 Optical microscope images of the DNA spots (Enterobacter F.). The figure on the left shows a bright field image of the sample and figure on the right a dark field image of a single spot. . . . 135
6.3 (a) AFM image of magnetic particles immobilized inside and outside (b) the spot. (c) AFM image of magnetic particles immobilized inside the spot in the positive control. The panels on the right show the height profiles measured along the white lines of the figures on the left. . . . 136
6.4 Fluorescence image of the positive control of the sample spotted with HEV. . . . 137
6.5 (a) Optical microscopic image of the HEV spot in bright field. (b) AFM images of magnetic particles immobilized inside the spots. The panel on the right shows the height profiles measured along the white lines of the figure on the left. . . . 138
6.6 Fluorescence image of the sample spotted with Staphylococcus Aureus. . . . 139
6.7 Typical experiment of molecular recognition: signal from one sensor (left panel) and from a reference (right panel) sensor [4]. 140
6.8 (a) Sensor response to the external magnetic field (R(H)) (Sample 2 of table 5.3) (b) Optical microscope image of the MTJ-based sensor, the sensing direction (i.e. the direction of the applied magnetic field) is shown. . . . 142
6.9 Output signal from one sensor as a function of time during the experiment of beads detection: beads injection is around t = 500 s, washing is around t = 950 s. . . . 142
6.10 (a) Sensor response to the external magnetic field (R(H)) (Sample 4 of table 5.3). (b) Optical microscope image of the MTJ-based sensor, the sensing direction (i.e. the direction of the applied magnetic field) is shown. . . . 144

6.11 (a), (b) Sensor and control signals, respectively, as a function of time: bead injection is around t = 2200 s, the first washing is around t = 3400 s, the second around t = 4000 s. 146
6.12 Microscope images before (on the left) and after (on the right) the molecular recognition experiment of synthetic DNA: (a), (b) bio-functionalized sensor chip; (c), (d) positive sensor; (e), (f) control sensor. 147
6.13 (a) Sensor response to the external magnetic field (R(H)). (b) Optical microscope image of the MTJ-based sensor, the sensing direction (i.e. the direction of the applied magnetic field) is shown. 148
6.14 (a), (b) Sensor and control signals, respectively, as a function of time: bead injection is around t = 2000 s, washing is around t = 3400 s. 149
6.15 Microscope images before (on the left) and after (on the right) the molecular recognition experiment of HEV virus: (a), (b) bio-functionalized sensor chip; (c), (d) positive sensor; (e), (f) control sensor. 151

List of Tables

3.1 Magnetron sputtering parameters for each layer and the relative deposition rates. 60
3.2 Optimized parameters of the first step of lithography. V_{dis} and V_{acc} stand for respectively discharge voltage and acceleration voltage. 62
3.3 Optimized parameters of the second step of lithography. . . . 63
3.4 Optimized parameters of the third step of lithography. 66
3.5 Parameters used in the evaporation process and relative deposition rate. The E-beam power is normalized to the full scale. 66

5.1 Samples grown and characteristics, including the SiO_2 and MgO thicknesses, the substrate cleaning and the roughness rms obtained. 101
5.2 SAF samples grown and relative thicknesses of CoFe and CoFeB. In red the optimal condition. 111
5.3 Samples grown and critical parameters: SiO_2 substrate thickness, MgO thickness, SAF structure, sensors and contacts area, annealing temperature. In red the optimal condition of the SAF structure. 114
5.4 Average RA product and corresponding error bar for the three values of the barrier thickness. 114
5.5 Summary of sample 1 and sample 7. 124

Sommario

Questa tesi si colloca nell'ambito di un progetto di ricerca volto allo sviluppo di una piattaforma, basata su biosensori spintronci, per il riconoscimento molecolare di DNA patogeno negli alimenti e nell'ambiente di lavoro della filiera agroalimentare. In particolare il progetto prevede la realizzazione di un sistema lab-on-chip che permetta il riconoscimento di molecole biologiche grazie all'uso di microarray di sensori magnetici ad effetto tunnel (MTJ) ad alta sensitività (limiti di detezione – LOD – inferiori al fM).
I biosensori spintronici hanno attratto una notevole attenzione negli ultimi anni poiché combinano elevata sensitività, alta portabilità e bassi costi di produzione. In questi dispositivi il riconoscimento di una particolare molecola (target) avviene facendo in modo che una particella magnetica (marker) si leghi alla molecola stessa, permettendo così la sua rivelazione tramite una variazione della resistenza elettrica del sensore (magnetoresistenza). L'area attiva del biosensore viene opportunamente funzionalizzata con la molecola sonda complementare (probe), per catturare tramite ibridazione le molecole target precedentemente legate alle sferette magnetiche.
L'inizio di questa tesi è coinciso con l'avvio del progetto stesso, e mi ha reso possibile seguirne l'evoluzione sin dalla nascita. Il lavoro sperimentale é stato realizzato sotto la supervisione del Professore Riccardo Bertacco, responsabile del gruppo NaBiS presso il centro LNESS-Dipartimento di Fisica del Politecnico di Milano, Polo Regionale di Como.
La prima parte del lavoro ha riguardato principalmente l'ottimizzazione dei sensori magnetici ad effetto tunnel con barriera di MgO, allo scopo di migliorarne le prestazioni in vista dell'alta sensitività richiesta dal progetto. Diversi dispositivi sono stati fabbricati e caratterizzati, ottenendo dei buoni risultati in termini di TMR, di affidabilità e ripetibilità del processo di fabbricazione. La seconda parte della tesi ha riguardato la progettazione dei

vari componenti della piattaforma con particolare attenzione al design del microchip contenente il microarray di sensori magnetici. La parte conclusiva del lavoro di tesi ha riguardato gli esperimenti biologici, che hanno permesso di dimostrare la possibilità di applicazione dei sensori magnetici fabbricati durante il lavoro di tesi ad un sistema biologico reale.
Le seguenti tematiche verranno affrontate nel corso dell'elaborato:

- Ottimizzazione della struttura del sensore: caratterizzazione di superfici con AFM e studio di eterostrutture magnetiche tramite misure MOKE e VSM.
- Fabbricazione dei sensori: deposizione della struttura tramite "magnetron sputtering" e litografia ottica.
- Caratterizzazione dei sensori con misure di magnetoresistenza e misure di rumore.
- Design della maschera optolitografica del microarray di sensori compatibile con la nuova piattaforma da sviluppare.
- Bio-funzionalizzazione dei sensori e *labeling* con nanoparticelle magnetiche.
- Riconoscimento molecolare su DNA sintetico e naturale.

Hanno collaborato a questo progetto: per la parte che riguarda la biofunzionalizzazione dei sensori l'Istituto di Chimica del Riconoscimento Molecolare (ICRM), per le misure di rumore il Dipartimento di Elettronica ed Infomazione del Politecnico di Milano, e per il progetto del sistema microfluidico il dipartimento CMIC del Politecnico di Milano (Department of Chemistry, Materials and Chemical Engineering, Giulio Natta).
La tesi é organizzata in sei diversi capitoli. Il primo capitolo tratta del background tecnologico su cui si fonda il lavoro ed in particolare fornisce una panoramica sui biosensori utilizzati attualmente, con particolare attenzione a quelli magnetoresistivi. Il secondo capitolo descrive i principi fisici su cui si basano i sensori magnetici ad effetto tunnel. Il terzo capitolo si occupa delle tecniche e dei metodi sperimentali utilizzati in questo lavoro. Nel quarto capitolo sono descritti i vari componenti della piattaforma lab-on-chip del progetto. Il quinto capitolo presenta i risultati sperimentali della fase di

ottimizzazione e caratterizzazione dei sensori MTJ fabbricati. Nel sesto capitolo sono presentati i risultati degli esperimenti biologici di riconoscimento molecolare. Infine sono discusse le conclusioni del lavoro e le prospettive future.

Abstract

This thesis work is part of a research project aimed at the development of a spintronic-based platform for the molecular recognition of DNA pathogens in foods and agrifood industries. In particular, the project involves the realization of a lab-on-chip system which allows the recognition of biological molecules exploiting a microarray of MTJ based sensors with high sensitivity (detection limits – LOD – less than fM).
Spintronic biosensors have attracted considerable attention in recent years because they combine high sensitivity, high portability and low production costs. In these devices the recognition of a particular biomolecule (target) occurs binding a magnetic particle (marker) to the molecule itself, thus allowing its detection by means of a variation in the electrical resistance of the sensor (magnetoresistance). The active area of the biosensor is suitably functionalized with the complementary probe molecules, in order to capture by hybridization the target molecules, previously labeled with magnetic beads.
The beginning of this thesis work occurred in conjunction with the project, allowing me to follow its evolution. The experimental work has been carried out under the supervision of Professor Riccardo Bertacco, responsible for the NaBiS group at the LNESS Center-Dipartimento di Fisica of the Politecnico di Milano, Polo Regionale di Como.
The first part of the work has dealt with the optimization of the MTJ sensors with MgO insulating barrier, in order to improve their performance in view of the high sensitivity required by the project. Several devices have been fabricated and characterized, obtaining satisfactory results in terms of TMR ratio, reliability and repeatability of the manufacturing process. The second part of the thesis has focused on the project of the prototype of the platform, with particular attention to the microchip design and the microarray of magnetic sensors. The final part of the work has concerned the biological

experiments, which have demonstrated the possible application of the magnetic sensors developed during the thesis work to a real biological system. The following topics have been addressed during the work:

- Optimization of the sensor's structure: atomic force microscopy characterization of layers' surface and characterization of magnetic heterostructures by means of magneto-optic Kerr effec and vibrating sample magnetometer.
- Fabrication of MTJ sensors: deposition of the multilayered stack by magnetron sputtering and optolithographic patterning.
- Sensors' characterization through tunnelling magnetoresistance measurements and noise measurements.
- Optolithographic mask design of the microchip for the new platform development.
- Bio-functionalization of the sensors' active area and labeling with magnetic beads.
- Molecular recognition of synthetic and natural DNA using MTJ sensors.

The bio-functionalization of the sensors has been performed at the "Istituto di Chimica del Riconoscimento Molecolare" ICRM. The noise measurements have been executed in collaboration with the "Dipartimento di Elettronica ed Informazione" of the Politecnico di Milano, while the microfluidic project of the new platform has been developed by the "Department of Chemistry, Materials and Chemical Engineering, Giulio Natta".
This thesis is organized in 6 chapters. In the first chapter, an oveview of the technological background concerning the state of the art of biosensors and magnetoresistive biosensors is illustrated. The second chapter discusses the physical principles of magnetic tunnel junctions. The third chapter explains the experimental methods which have been employed during this thesis work. In the fourth chapter the design of the lab-on-chip platform and its main components are described. The fifth chapter explains the results related to the optimization and characterization of the fabricated sensors. In the final chapter the experiments of biomolecular recognition are illustrated and, finally, the conclusions and the future perspectives are presented.

Chapter 1

Introduction

1.1 Biosensors

A biosensor can be defined as a compact analytical device or unit incorporating a biological or biologically-derived sensitive element. Nowadays bio-sensing technologies are of increasing importance in healthcare, agri-food, enviromental and security sectors, and this is reflected in the continued growth of global markets for such technologies. The biosensors research field is indeed very vast, [50] [30], and one of the contributing factors is the continued development of microfabrication technologies, since 1990s [55].

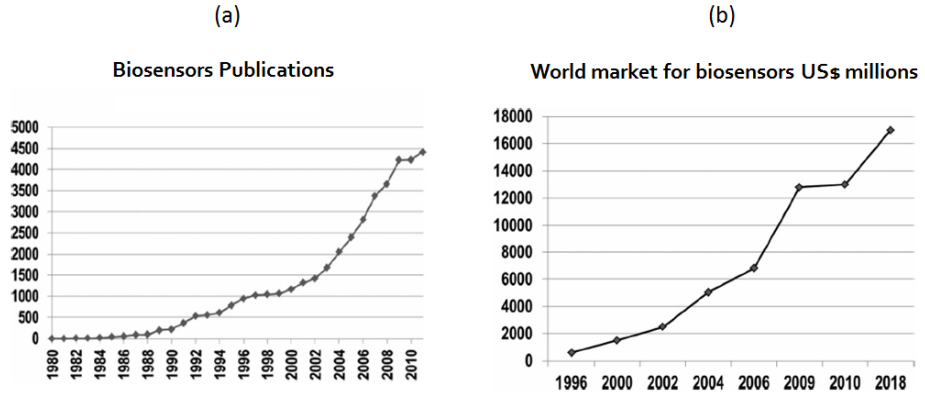

Figure 1.1: (a) Graph of the publications in biosensors during the period from 1980 to 2011; (b) Graph of the world market for biosensors estimated from various commercial sources and predicted for the future in US$ millions. [2]

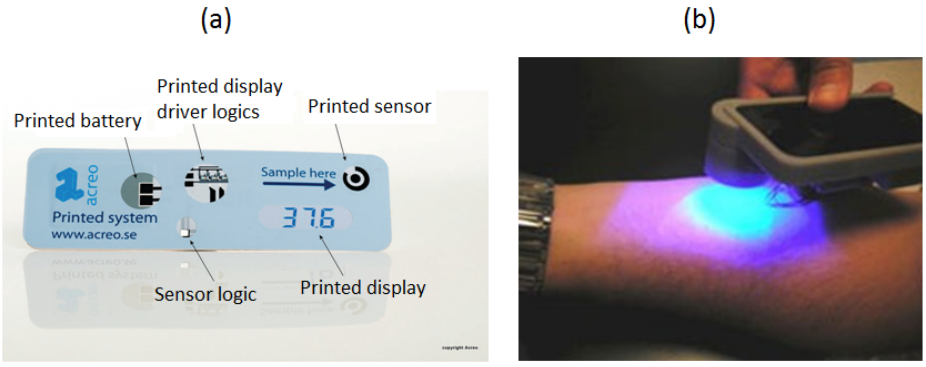

Figure 1.2: (a) All-printed biosensing system: glucose concentration can be measured in few seconds and observed via the printed display; (b) Implantable biosensors for continuous glucose monitoring [1].

Biosensors are promising alternatives to conventional analytical tools since they offer advantages in size, cost, specificity, rapid response, precision and sensitivity. Healthcare is and will continue to be the most important area for the application of biosensors. For example glucose biosensors for diabetes have had profound effects on the disease management. Moreover cardiac disease or cancer markers and single cell cancer detection have attracted considerable recent literature.

Last but by no means least, nucleic acid-based biosensors have played an increasingly significant role in medicine. This kind of biosensors exploits systems of biomolecular recognition which provide a biological-sensing system (bioreceptor), a transducer and an output system. The bioreceptor is a biological probe typically immobilized on the biochip surface. For example, DNA microarrays with thousands of probes can be used for the study of different genes expressions. The biomolecular recognition of the probes, with an unknown target sample, generates a physical or chemical change, that can be converted to an electrical signal by the transducer. Finally, the electrical signals are further treated (amplified, filtered...) in order to retrieve an understandable analysis of the experiments.

Other important fields of application are the agricultural and food sectors, where biosensors can be exploited in order to control production processes and ensure food quality and safety by means of reliable, fast and cost effective procedures. Indeed over the past few years a great number of biosen-

sors have been developed for the evaluation of food composition, in order to analyze external substances in food products such as pesticides, fertilizers, genetically modified organisms or pathogenic microorganisms including *Salmonella*, *Listeria monocytogenes*, and *Escherichia coli*. A traditional method for the detection of pathogens in food is through enzyme-linked immunosorbent assays (ELISA) [9]. The ELISA test is based on qualitative or quantitative color changes, using an enzyme as a reaction biomarker between an antigen and an antibody. A strong color change will indicate a greater concentration of the analyte. However, the reuse of antibody receptors linked to enzymes increases the cost of detection, as well as the limited sensitivity of antibodies increases the possibility of unreliable results in a rapid test. In this regard, biosensors can offer rapid and effective detection options to control biological hazards. For example for the rapid detection of *Salmonella*, piezoelectric antigen-antibody and resonance magnetoelastic biosensors have been used [46], while fiber-optic biosensors [37] or surface plasmon resonance biosensors (SPR) [71] have been developed for the detection of *Listeria monocytogenes*.
Although conventional methods for the detection and identification of microbial contaminants can be very sensitive, inexpensive and present both qualitative and quantitative information, they can require several days to yield results. Lab-on-chip biosensors offer an exciting alternative to the more traditional methods, allowing rapid “real-time” and multiple analyses that are essential for the detection of bacteria in food products [67] [99] [113].

1.2 Lab on a chip

Over the past decade, many important technological advances have been made in the use of nanotechnology for biomolecular detection. Coupled with the development of optical, electrochemical, and various other techniques for monitoring biorecognition events, a lot of effort has been put into realizing accurate, sensitive, selective, small and practical biosensing devices, for both laboratory and point-of-care applications. These biochips are being fully integrated in compact handheld microsystems that provide all the electronic circuitry required, and also perform the sensor signal acquisition.
This tendency to scale of single or multiple lab processes down to chip-format is known as "Lab on a chip". A lab on a chip is a device that integrates one or

several laboratory functions on a single chip of few centimeters in size. The driving force for miniaturization is the aim of increasing processing power while reducing the economic cost and environmental impact. The advantages brought to biology and diagnostics by the miniaturization are different. For example an important benefit is the low fluid volumes consumption that implies less waste, lower reagents costs and less required sample volumes for diagnostics. Moreover the reduced sizes brings to faster analysis and response times due to short diffusion distances, fast heating/cooling and high surface to volume ratios. The faster response of the system allows also better process control. The integration of much functionality in small volumes allows to use compact systems bringing to a massive parallelization, which permits high-throughput analysis. To these important advantages are also added lower fabrication costs, allowing mass production, and safer platform for chemical, radioactive or biological studies thanks to the integration of functionality, the smaller fluid volumes required and stored energies.
A common problem in all biosensors is the slow diffusion of the target DNA to the sensors surface. For this reason lab on a chip is closely related to, and overlaps with microfluidics, which describes primarily the physics, the manipulation and study of minute amounts of fluids. Microfluidics integrated sensors allow to improve the sensitivity: microfluidics can confine the DNA solution within the vicinity of the sensor surface, therefore the target DNAs do not need to travel a long distance before binding the probe oligonucleotides. This can potentially improve the sensitivity and decrease the assay time and the quantity of biological material.

1.3 Biomolecular recognition experiments

The most widely spread method for biomolecular recognition experiments relies on the principle of detection by hybridization, i.e. the interaction between two complementary strands of nucleic acids into a single complex. Hybridization allows a highly parallel analysis of many different biomolecules. Indeed, functionalizing specific small areas of a detector with a common sequence of single stranded DNA (so-called probe DNA), this area can become sensitive to complementary DNA sequences in its vicinity (so-called analyte or target DNA).
A typical biomolecular recognition detection experiment needs four different

steps:

1. Probe immobilization on the chip surface
2. Target recognition
3. Washing
4. Signal detection

First, the probe DNA strands are coupled to the sensor surface in a so-called immobilization step. Then, the solution is spread across the entire sensor surface, and matching probe and analyte strands hybridize to each other. After hybridization a washing step is necessary in order remove all the non-hybridized DNA strands. The stringency control of this step is crucial in order to avoid false negative and positive results.

1.3.1 Detection methods

The detection of the hybridization events can be direct (label free, fig. 1.3 (a)) or can employ additional markers specifically bound to the hybridized biomolecules (not label free fig. 1.3 (b)). Marker-free methods are based on the detection of the immobilized species by comparing the measure of selected properties before and after immobilization. In this way undesiderable effects such as marker binding instability, steric hindrance or spurious biases induced by labelling are neglected. However, since the signal originating from the sample can only change incrementally upon immobilization, it is rather difficult to distinguish the signal from the background. Furthermore, other ingredients of the surrounding solution, like trapped ions, can falsify the outcome of the measurements, so that great care has to be taken in interpreting the results. For this reason usually, in order to have sensitive measurements, expensive instrumentation is needed, making in this regard marker-enabled methods favourable. The latter have the advantage of large signal to noise ratio, since markers generally possess properties which can be easily distinguished from the other materials involved (e.g. they emit light, transfer charge in an electrochemical redox process, or, as investigated within this thesis, produce a magnetic stray field). However, the use of markers requires an additional molecular recognition step, the labeling process (fig. 1.3

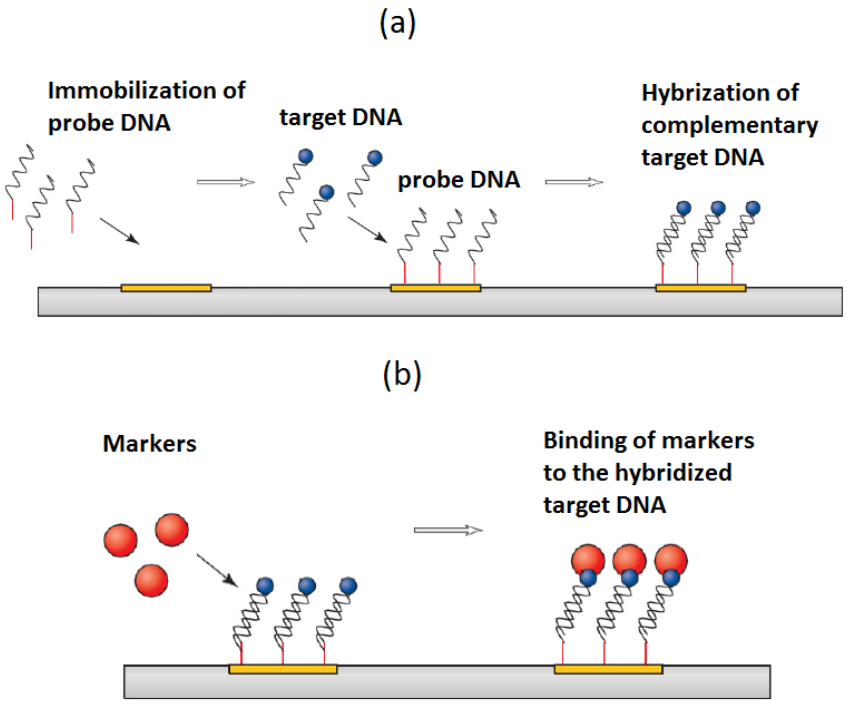

Figure 1.3: (a) A schematic of the hybridization process. (b) Binding of markers to hybridized target DNA.

(b)), and because there is always a percentage of hybridized pairs which do not contribute to the signal, because no markers are bound to them, this method can never reach 100% efficiency. Another problem of this approach is represented by the size of the markers. Indeed if the DNA target is immobilized on a big particle (close to micron size), the steric hindrance could reduce the probability of recognition. Therefore it is desired to reduce the size of the labels as much as possible.
In the next paragraphs two kind of detection methods are described, fluorescent and magnetic detection. However, many other approaches, involving different detection principles, have been investigated in the past decade (for a review see [112]). The following table shows a classification of various groups of biosensors currently in use [79].

Transduction	Detection mode
Optical	*Surface Plasmon Resonance*- measures variations in the surface optical parameters caused by the biochemical reaction; the analyte concentration is measured upon adsorption
	Optical fibers- uses an optical fiber to propagate the signal emitted by a fluorescent label after hybridization
	Ellipsometric- measures the reflection of a light beam from a reflective surface in reaction to adsorbed analytes
Thermal	*Calorimetric*- detects temperature changes in a solution containing specific analyte and converts it into concentration
Mass sensitive	*Surface acoustic wave*- generates and detects acoustic waves using inter-digital transducers. This will detect changes on the surface, such as mass loading, viscosity and conductivity changes, thus enabling quantification of the deposited mass
	Quartz crystal microbalance- consists of a system measuring the change in frequency of a quartz crystal resonator, related to the mass increase caused by hybridization
	Cantilever- nanomechanical biosensors microfabricated with the standard silicon technology. The surface is coated with detectors which will cause the cantilever to bend once binding occurs
Electrochemical	*Conductance*- measures the change in the conductive properties of medium between two electrodes caused by the hybridization reaction.
	Amperometric/Voltammetry- measures the current generated during redox reaction
	Potentiometric- detects charge accumulation or potential caused by hybridization
	Impedance- measures both resistance and reactance (change from weak or non-charge substances to highly charged)

Fluorescent detection

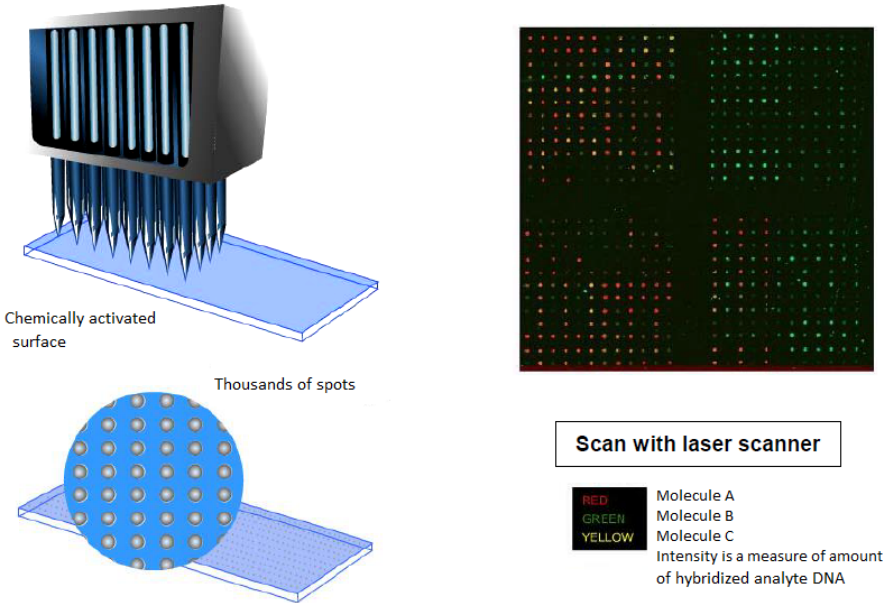

Figure 1.4: DNA microarray spotters producing thousand of spots on the surface. The amplified DNA strands are labeled with fluorophores and fuorescence scanner detects the light emitted by the labels; the different colours indicate that different biomolecules have been detected.

In this kind of detection method, fluorescent markers are bound to the hybridized target DNA. Subsequently they are excited by a monochromatic (e.g. laser or LED) or white (e.g. tungsten lamp) light source, and their emission is collected by a suitable detector.
Currently, this kind of detection is closely connected to DNA amplification by polymerase chain reaction (PCR), of which a brief description is given in paragraph 1.3.2. For DNA microarrays, specific sequences that probe the presence of complementary DNA strands, are spotted onto the sample surface. A DNA chip can consist of thousands of micron-sized DNA spots, and they are typically produced by microarray spotters that put small drops (0.1–1 nl) of probe DNA onto the sensor surface. Since the sequence and position of every probe DNA spot is known, the composition of the sample can be mapped if the amount of hybridized analyte DNA is detected for each spot (fig. 1.4). After the spotting procedure, the probe DNA strands are immobilized onto the sample surface. Then the target DNA is amplified

using the PCR technique, and the amplified strands are labeled with fluorophores. After the hybridization the chip is introduced into a fluorescence scanner which detects the light emitted by the labels.
These fluorescence based systems suffer from some weaknesses. The first one is directly related to the label, since its fluorescence emission is gradually reduced along the time. This phenomenon is called photo-bleaching. Moreover, since these systems are still bulky and expensive and have limited dynamic range and sensitivity due to nature of the detection principles, other devices and detection techniques have been developed. In order to improve portability and rapidity, the integration of fluorescence-based systems have been pursued. One example is the incorporation of photodetectors (Si, amorphous Si or III-V based) in chips to detect the light emission of fluorophores [33]. Since fluorescent labels need to be optically excited, semiconductor lasers are also being integrated in the chip.
However several major drawbacks of this technique still remain. Broad absorption and emission bands, and nonuniform rates of fluorophore photobleaching may reduce accuracy. Sophisticated algorithms and expensive instrumentation are needed for fluorescence readout, restricting application to laboratories. Furthermore, this kind of detection does not permit to reach very high biological sensitivity without the use of amplification processes like PCR, which can introduce biases and spurious effects in the assay.

Detection method employing magnetic markers

The use of nanoparticles as labels in biomolecular detection, in place of conventional molecular fluorophores, has led to improvements in sensitivity, selectivity, and multiplexing capacity. For example nanoparticle based detection can be based on the detection of specifically bound metal nanoparticles through their optical properties (mostly, gold particles are used). In this context magnetic nanoparticles and microparticles can offer important advantages: having embedded magnetic entities, they can be magnetically manipulated using permanent magnets or electromagnets during a biological process. Of particular interest are small mono-domain nanoparticles (called *beads*) because, having a dimension that is typically of the order or smaller than the typical thickness of a magnetic domain wall, they are single domain particles. Mono-domain magnetic particles become superparamagnetic, i.e. their time-averaged magnetization is zero without a magnetic field, but, when

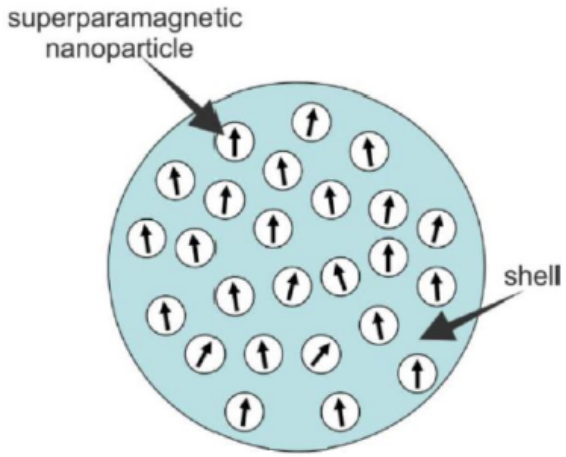

Figure 1.5: Sketch of magnetic bead formed by magnetic nanoparticles in a non-magnetic matrix/shell.

a magnetic field is applied, their magnetic response is practically immediate. A typical magnetic nanoparticle consists of a magnetic core surrounded by a non magnetic coating for selectively binding the biomaterial of interest (e.g. a specific cell, protein, or DNA sequence). In fact their surface can be easily functionalized with specific receptors, which allow specific binding to the desired biomelecules. The most wide-spread labeling techniques exploit the strong interaction between biotin and streptavidin in order to attach biotin-modified target DNA to streptavidin-coated magnetic particles.

Iron oxides, such as magnetite (Fe_3O_4), are preferentially used as core material instead of iron because are more stable against oxidation. Typically superparamagnetic particles of Fe_3O_4 with diameters in the range 5-50nm are used. In order to maintain the properties of superparamagnetic particles, but achieving a greater volume and magnetic moment, larger magnetic beads (0.1 to 5 μm in diameter) have been introduced. They are obtained by embedding several superparamagnetic nanoparticles, not magnetically interacting, in a non-magnetic matrix. A sketch of a magnetic bead made by superparamagnetic particles core in a polymeric shell is illustrated in figure 1.5. In this thesis work Micromod Nanomag-D streptavidin-coated magnetic beads, with a diameter of 250 nm, a core of 75-80% magnetite in a shell of dextran, have been used.

The magnetization curve of an ensemble of superparamagnetic particles is

hysteresis free and this has important consequences for bio-analysis. Indeed suspended superparamagnetic particles tagged to the biomaterial of interest can be removed from a matrix using a magnetic field, but they do not agglomerate (i.e. they stay suspended) after removal of the field. Hence, it is very easy to switch on and off the magnetic interaction. Another important advantage of using magnetic particles is the fact that all other components in the solution are essentially non-magnetic, thus eliminating interferences and minimizing the background signal.
Therefore the use of a magnetic approach, compared with optical/fluorescence methods, has the main advantages of low magnetic background noise in biological samples and the ability to actuate or manipulate magnetically labelled molecules using controlled magnetic gradients.

1.3.2 Limit of Detection and the Polymerase Chain Reaction

The *limit of detection* – LOD – is the smallest amount of a quantity of interest which produces a measurable output signal. In biological terms, the LOD can be considered as the lowest target biomolecule concentration that is required to produce a detectable signal. As evident, this parameter is a direct measure of the sensitivity of the device.
Usually, only a small number of copies of target nucleic acids are present in test samples. For example a microbial cell usually contains from 1 to 100 target-DNA sequences, so that the total target-DNA available per sample ranges from approximately 10^{-24} to 10^{-16} moles. Considering average sample volumes, of the order of tenth to hundreds of microliters, the target molecule concentrations may range from zepto- (10^{-21} M) to femtomolar (10^{-15} M). This is far below the current limit of detection for most of the hybridization-based systems. For example the optical detection systems using conventional fluorescence scanning do not go beyond the picomolar range [41]. Electromechanical devices integrating microcantilevers [110] or quartz crystal microbalances [80] present LOD of 10^{-11} and 10^{-14} M, respectively. Other systems based on electrochemical detection methods are closer to the required sensitivity [116] [84]. On the other hand magnetoresistive biosensors have demonstrated limit of detection in the zM range (see the next section 1.4)
In order to make biological samples measurable by standard detection systems, the sample amplification method of polymerase chain reaction (PCR)

is typically used. The polymerase chain reaction (PCR) is a biochemical technology in molecular biology to amplify a single or few copies of a piece of DNA across several orders of magnitude, generating thousands to millions of copies of a particular DNA sequence. PCR is now a common and often indispensable technique used in medical and biological research labs for a variety of applications. These include DNA cloning for sequencing, the diagnosis of hereditary diseases, the identification of genetic fingerprints (used in forensic sciences and paternity testing) and the detection and diagnosis of infectious diseases.

The method relies on thermal cycling, consisting of cycles of repeated heating and cooling. The more the cycles performed, the larger the amplification. Each cycle is generally repeated for about 30-40 times, and in principle, each cycle should double the amount of DNA.

Almost all the PCR applications employ an enzyme called DNA polymerase (after which the method is named) which assembles a new DNA strand from DNA building-blocks, by using single-stranded DNA as a template and DNA oligonucleotides (DNA primers), which are required for initiation of DNA synthesis. The primers contain sequences complementary to the target DNA and are key components to enable selective and repeated amplification. As PCR progresses, the DNA generated is itself used as a template for replication, setting in motion a chain reaction in which the DNA template is exponentially amplified.

In the first step, the two strands of the DNA double helix are physically separated at a high temperature (of about 90 °C) in a process called DNA melting or denaturation. In the second step, the hybridation, the temperature is lowered down to $\sim 50\,^{\circ}\mathrm{C}$ and the two DNA strands become templates for DNA polymerase to selectively amplify the target DNA. In the third step the temperature is raised, to the optimum value depending on the DNA polymerase used, and replication starts producing copies of the DNA.

The utility of PCR comes from the very small amount of starting material required. Manipulation of the specificity can be achieved by simply varying length and nucleotide sequence of primers and annealing temperature.

1.4 Magnetoresistive biosensors

This thesis is concerned with an approach involving the use of magnetoresistive sensors to detect biomolecular recognition. In the last years magnetoelectronics has emerged as a promising new technology for biosensors and biochip development. Magnetoresistive-based sensors, conventionally used as read heads in hard disk drives, have been used in combination with biologically functionalized magnetic labels to demonstrate the detection of molecular recognition.
Two different procedures for magnetic labeling of hybridization events can be possible. In the post-hybridization method (fig. 1.6 (a)) the target molecules

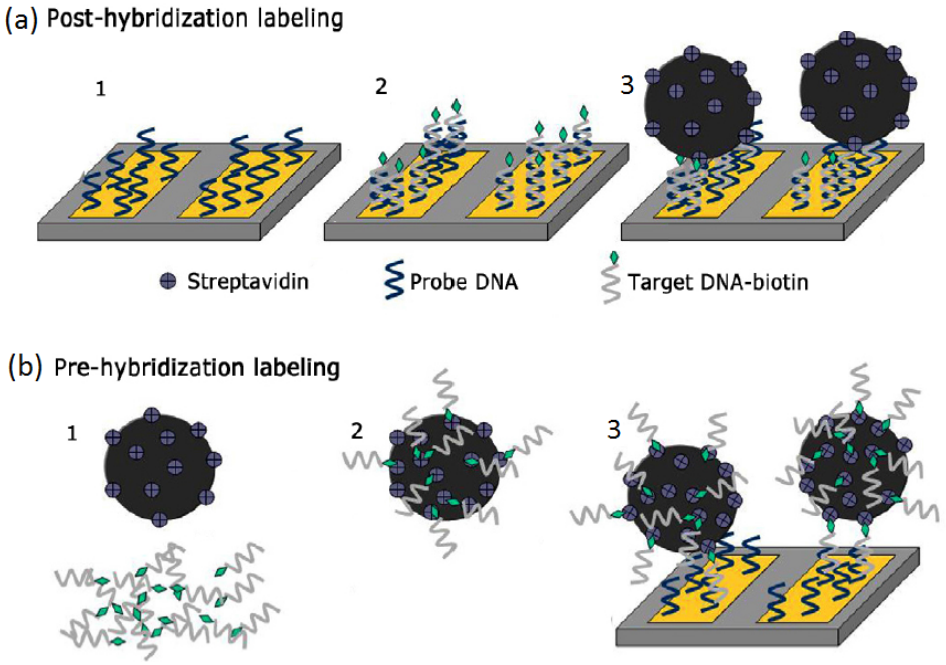

Figure 1.6: Schematic representation of the two different procedures for magnetic labeling of hybridization events: post-hybridization and pre-hybridization magnetic labeling. In the former, first probe DNA is immobilized (1), then target DNA hybridizes (2) and finally labeling of pre-hybridized target DNA occurs. In the latter, first target DNA and magnetic particles are concentrated (1) in order to enable streptavidin-biotin bonds (2), then the labels coated by target DNA are placed onto the sensor so that hybridization occurs (3).

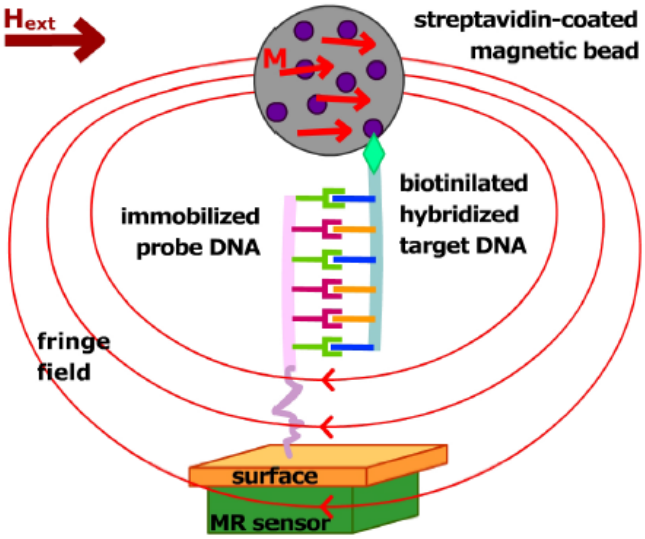

Figure 1.7: Schematic representation of the detection process of a magnetic bead: when an external field is applied the bead is magnetized and the MR sensor detects the fringe field generated from it.

are labeled with a small biochemical label, such as biotin. Biotinylated target molecules, bound to complementary surface-bound probe molecules, are then detected by introducing magnetic labels functionalized with streptavidin, the complementary molecule to biotin. In the case of pre-hybridization (fig. 1.6 (b)), the target biomolecule is magnetically labeled and passes over the probe molecules, which are immobilized over the sensors. In this case, the hybridization process can be favoured by the magnetic interactions between the sample and the beads, even if the main drawback is related to the steric hindrance of the magnetic beads which prevents chemical interations between probe and target DNA. However, in either cases, when a magnetic field is applied, because of the stray field generated by the magnetic beads, the sensors can detect the beads via a change in their resistance, at a fixed sense current (fig. 1.7). The unbound target biomolecules are then washed away and residual sensor signals are obtained at sensor sites, where complementary magnetically labeled target-probe have successfully interacted.

An important aspect to be taken into account when magnetoresistive biosensors are used, is the position and extension of the biological active area, i.e.

the region where the biological probes are immobilized. It has been demonstrated [24] that the average magnetic field generated by the beads over the sensor area depends dramatically on their position, changing even its sign if generated by a particle inside or outside the sensor. In the borderline case of an ideal infinite monolayer of beads equally spaced, the resulting total magnetic field could be zero. For these reasons a significant increase in the sensor sensitivity and performances can be achieved through a careful control over the extension and position of the bio-functionalized area on the chip sensors. It has been demonstrated that a very high gain on the sensor sensitivity can be achieved when the bio-functionalized area coincides with the sensor active surface. This is compatible with an optolithographic patterning of the sensors' surface [4], which allows to immobilize the probe biomolecules only in corrispondence of the patterned regions. This procedure is described in detail in chapter 4 and will be the first step of the experiments of biomolecular recognition in the new platform to be developed.
The hybridization detection system based on magnetoresistive (MR) sensors, associated to the use of superparamagnetic nano-particles, arose with promising characteristics: high sensitivity, fast performance and electronic platform compatibility leading to integrability, miniaturization, scalability and portability. However, only few groups have demonstrated the applicability of such devices to the real detection of biological events. For example magnetic labels, in combination with highly sensitive spintronic biosensors, have offered the opportunity to reach sensitivities in the zM range, as reported by the group of Wang S. X. [117] [118]. In this work a wash-free protein detection assay has been demonstrated employing giant magnetoresistive (GMR) nanosensors. GMR biosensors have been found to be more suitable than other kinds of magnetoresistive sensors for this type of applications. Indeed their compactness, robustness, broad linear dynamic range and real-time readout capabilities make them ideal for analysis measurements.

Compared to advances in enzyme sensors, immunosensors, and microbial biosensors [122] [123] [25] [73], relatively little work exists on DNA based biosensors [70], and among them especially with tunneling magnetoreistance (TMR) based sensors. Despite the higher sensitivities achievable with TMR respect with GMR [20], the more difficult fabrication process and thus reproducibility of the devices performances has prevent so far the TMR sensors to be fully exploited in extensive bioassay studies and point of care appli-

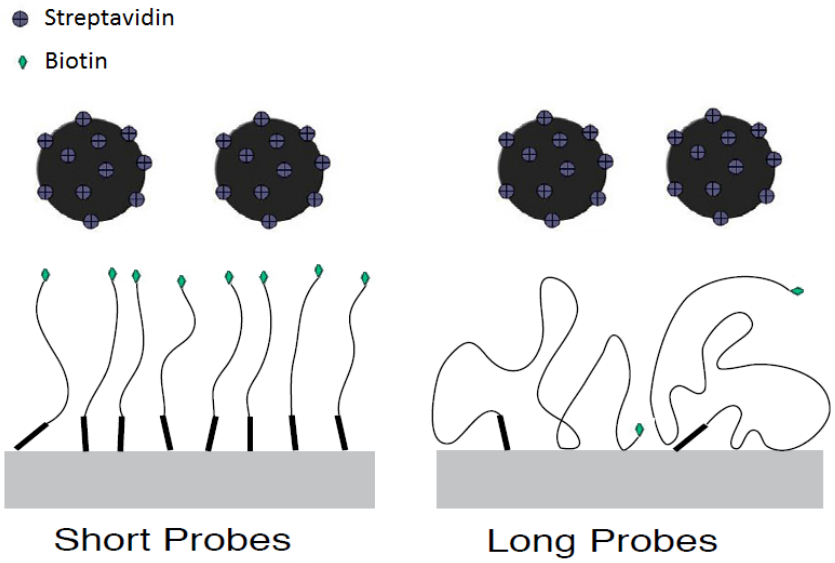

Figure 1.8: Probe length and packing configuration influencing biotin-streptavidin binding.

cations. Most reports to date have only shown the detection, by means of TMR based sensors, of magnetic particles without analytes, or the detection of synthetic oligonucleotides (COCU) [3] [89] [4]. The main difficulty concerning the recognition of natural DNA, as will be discussed in chapter 6, is related to the length of the oligonucleotides, which is associated with a reduced hybridization efficiency due to steric effects. Indeed while short probes, such as synthetic ones, pack in extended configurations, long probes can exist in more flexible, polymeric-like configurations, becoming a drawback for the hybridization process between biotin and streptavidin (see figure 1.8).

In this context, the project of this thesis, which will be described in detail in the next section and in chapter 4, overcoming some typical problems of TMR based sensors, like the low fabrication yield and the higher electrical noise respect with GMR, which can be considered important steps towards the detection of natural DNA employing TMR based biosensors. In fact, during this work an experiment of molecular recognition of pathogen DNA (HEV virus, 100bases) has been successfully completed by means of a microarray of 8 TMR sensors (see chapter 6).

1.5 Thesis project

This thesis work is part of a project, in collaboration with several lombard companies and research groups, with the aim of developing a platform for the detection of chemical and biological dangerous substances in food and in food processing environments. In particular the project aims at the detection of two classes of pathogens of great agribusiness interest:

- Hepatitis E virus
- Pathogenic bacteria (*Salmonella* and *Listeria monocytogenes*).

Hepatitis E is a viral disease. Nowadays it is an important problem in developing countries, in which it is frequently epidemic and it is mainly transmitted through contaminated water or food. *Salmonella* and *Listeria monocytogenes* are pathogens widespread in nature and are among the main causes of food poisoning. Monitoring these pathogens is of strategic importance for food production sector, both for the complexity of the methods currently used for their detection and for the growing importance that these pathogens play in the agri-food production.
The classical diagnostic methods, such as bacterial DNA detection by PCR and electrophoresis, have the drawback possibility to identify just one or a few bacteria in a single experiment. In contrast, combining microarrays technology and spintronic sensors in a lab on chip system, the request of detection of more pathogens in parallel could be fulfilled.
In particular this project combines the following technologies:

- **Spintronic biosensors** for measuring the specific nucleic acids concentration extracted from pathogenic organisms. In particular the project involves the construction of a microchip with a microarray of magnetic tunnel effect sensors for the detection of the two kinds of pathogens.
- **Integration of microarrays in systems "lab on chip"**. Traditional methods require highly qualified personnel and laboratory analysis to ensure high quality, which, however, cannot be performed 'on-site'. The devices lab-on-a-chip-based provide an alternative suitable for use in-situ and are characterized by speed of analysis, sensitivity,

specificity and automation. The realization of this type of devices derives from the idea of integrating all analytical processes in a small space for analyzing complex samples outside of a laboratory.

The development of such on-chip magnetic-based platform would therefore provide these advantages, compared to the current methods:

1. Quick diagnosis
2. Easy use
3. Versatility
4. Multi-target analysis
5. Greater sensitivity (up to fM)
6. Greater specificity
7. Reduced cost
8. Small size and portability.

1.6 Thesis outlook

The thesis work can be divided into three main phases:

1. In the first part of the work the design of the microchip for the platform, containing the sensors' microarray, has been carried out.
2. In the second part of the thesis numerous different sensors have been fabricated and characterized in order to optimize the manufacturing process and the performances of the magnetic device. MTJ junctions having resistance between $30k\Omega$ and 100Ω have been produced, with good results regarding the TMR ratios, up to 90%, and the linearity of the transfer curves.
3. Finally preliminary experiments of molecular recognition of HEV (Hepatitis E virus, 275 nM) have been carried out. Despite there is still much work to be done to move towards multi-target analysis, these experiments can be considered a good result.

Here an overview of each chapter of the thesis is presented:

- **Chapter 1: Introduction**: This chapter gives a brief description of the scientific background about biosensors and lab-on-chip platforms. Moreover the project of my thesis and a short summary of the work are presented.
- **Chapter 2: Magnetic Biosensors**: In this chapter, after a brief overview of the various magnetoresistive sensors, the theoretical aspects such as the physics, working principles, structure and main applications of TMR sensors are illustrated.
- **Chapter 3: Experimental methods**: In this chapter the experimental techniques used in this work, including the machinery, the explanation of the optolithography, the characterization techniques, the different setups and methods used for the experiments, will be shown.
- **Chapter 4: Platform layout**: Here the design of the platform and its components will be explained, with particular attention to the design of the mask for optical lithography, realized by myself.
- **Chapter 5: Sensors optimization and characterization**: In this chapter I focus on the fabrication, characterization and optimization of the magnetic device, showing the experimental results and the conclusions.
- **Chapter 6: Biological experiments**: Here the preliminary biological experiments are presented, including the experiments of beads detection and molecular recognition, and the study of surfaces functionalized with biomolecules labeled with magnetic nanospheres. The results and the conclusions are also showed.
- **Conclusions**: Here the conclusions of this thesis work and the future perspectives are summarized.

Chapter 2

Magnetic Biosensors

In the past decade, significant effort has been put towards the detection of magnetic micro- and nano-particles using spintronic sensors. This work has led to the development of new spintronic technologies based on magnetic sensors for the detection of the presence/absence of magnetic labels in target biomolecules [66] [93] [42]. All these magnetic sensors exploit the principle of magnetoresistance. Magnetoresistance is the property of a material to change the value of its electrical resistance when an external magnetic field is applied to it. There are different kind of magnetoresistive sensors: anisotropic magnetoresistive (AMR) and giant magnetoresistive (GMR) sensors, spin valves (SV), magnetic tunnel junctions (MTJ), or planar Hall-effect sensors (PHE). The anisotropic magnetoresistive effect (AMR) originates from the change in material resistance, which occurs when the magnetization changes from parallel, with respect to the direction of current flow, to transverse. This effect is present in ferromagnetic alloys (i.e. NiFe, NiFeCo) and it forms the basis of single thin-film sensors, such as the planar Hall sensors [13] and the AMR sensors [75]. GMR sensors have been extensively studied as biosensors for biomolecular detection and recognition [11] [74] [43]. The GMR effect is based on the spin-dependent interfacial and bulk scattering asymmetry that is found for spin-up and spin-down conduction electrons crossing ferromagnetic/nonmagnetic/ferromagnetic multilayer structures, where the parallel or antiparallel alignment of the ferromagnetic layers can be engineered exploiting the bilinear coupling phenomena (it will be described in paragraph 2.2.2). An applied magnetic field is used to change the relative orientation of the magnetizations of the two magnetic layers. When they

are parallel, the electrical resistance of the structure is low, when they are antiparallel, the resistance is high. This is the basis of GMR sensors [49] and also spin valves [36] [36], which are used in most computers as read heads measuring the fringe magnetic field created by magnetized regions on the track (bits).
Among the various types of magnetic sensors just described, magnetic tunnel junctions (MTJs) assume great importance because of their greater flexibility in design and because they benefit from recent research and technological advances, which aim at the development of future ultra high density magnetic memory chips and high magnetic sensitivity. In the next sections the theoretical aspects such as the physics, working principles, structure and main applications of TMR sensors are illustrated.

2.1 MTJ sensors

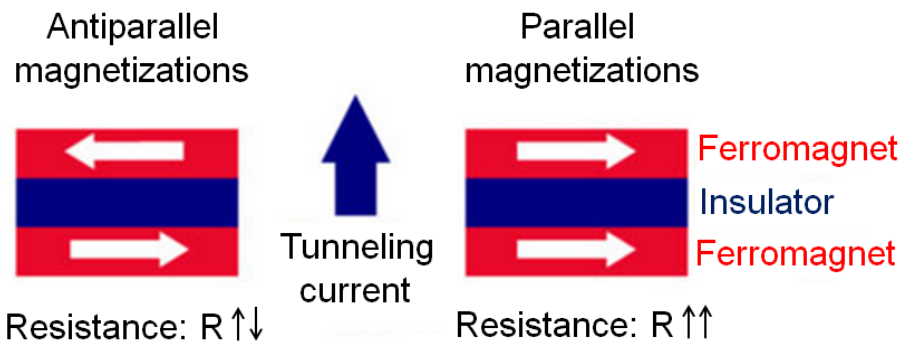

Figure 2.1: Tunneling current flowing perpendicular to the layers of a MTJ.

The basic stack of a Magnetic Tunnel Junction (MTJ) is constituted by two ferromagnetic (FM) layers separated by an insulator (I), FM/I/FM (figure 2.1). When a bias voltage V is applied across the multilayer stack, a quantum - mechanical tunneling current flows across the insulating barrier, that is thinner enough, typically less than 2 nm. One of the FM layers has its magnetization pinned, acting as a reference layer, while the other is free to move under the influence of an applied external magnetic field, similar to the Spin Valve sensor. A bias voltage applied across the MTJ results in a spin polarized tunneling current that flows perpendicular to the layers.

The magnitude of tunneling current depends on the relative orientation of the magnetizations of both magnetic electrodes separated by the insulating layer. The largest value is obtained when the magnetizations of each layer are oriented parallel to each other, and it is lowest when antiparallel, corresponding to the lowest and highest tunneling resistances states, respectively.

During this thesis MTJs based on $Co_{40}Fe_{40}B_{20}/MgO/Co_{40}Fe_{40}B_{20}$ interfaces have been fabricated, varying the MgO barrier thickness from 2nm to 0.9nm. Magnetic tunnel junctions (MTJs) with crystalline MgO barriers are being intensively studied. In addition to being ideally suited as non volatile magnetic random access memory, MgO based magnetic tunnel junctions MTJs are excellent magnetic field sensors. As such, they are used in read write heads in the magnetic storage industry and played a big role in the increase in storage density in the last few years. Applications include magnetic microscopy, spin torque oscillators and biological assays.
Proper growth and annealing conditions lead to a tunneling magnetoresistance (TMR) in excess of 200% [85] [27]. Indeed for large TMR, typically above 200%, MgO/CoFeB based MTJs need a thermal anneal step up to 360 °C to achieve highly crystalline MgO/CoFeB interfaces [52]. And this value can exceeds 600% using molecularbeam- epitaxy (MBE) grown [59]. The reason for the higher TMR is due to the coherency in the crystallized CoFeB/MgO/CoFeB structure leading to coherent tunnelling [22]. Indeed, during the tunneling process, the Bloch states couple with evanescent states within the barrier and, since the evanescent states decay with different rates depending on their symmetry, also the tunneling probability of the coupled Bloch states will be different. In case of coherent tunneling, only states with the same symmetry can couple, and those which decay most slowly will dominate the tunneling probability, that will result very high.

2.1.1 Jullier's model

The tunneling effect in the system FM/I/FM can be roughly explained by the Jullière model [63]. The magnitude of the tunneling current is related to the overlap of the exponentially decaying wave functions inside the barrier. Therefore, the current exponentially decreases with the barrier thickness. The tunneling resistance depends on the relative orientation of the magnetizations on both sides of the barrier. The probability of tunneling is pro-

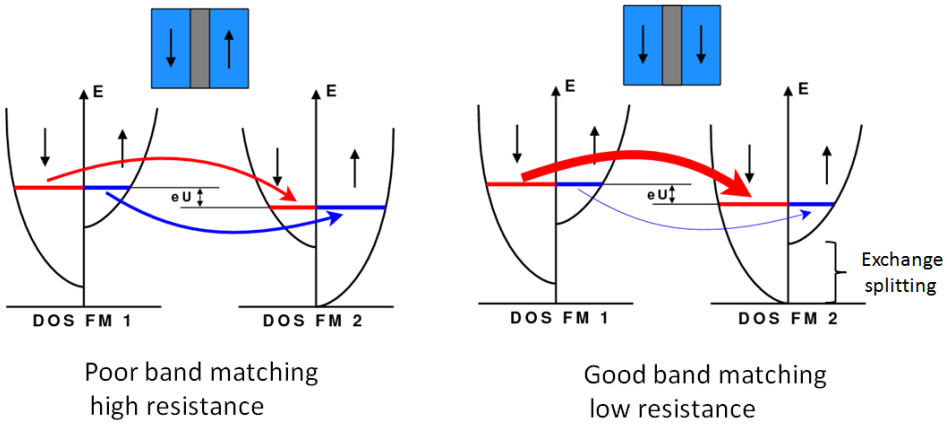

Figure 2.2: Valence bands illustration of spin-dependent tunneling across an insulating barrier, in case of antiparallel and parallel alignment. The arrows in the boxes show the majority spin in the two electrodes.

portional to the product of the density of states in both FM layers adjacent to the barrier, that depends on the spin polarization (P) of electrons. The result is a change in the tunneling conductance (G) between the parallel and antiparallel alignment of the magnetizations of the two FM electrodes. The total conductance in the parallel configuration ($G\uparrow\uparrow$) and in the antiparallel configuration ($G\uparrow\downarrow$), assuming conservative spin tunneling [72] and the parallel of the two spin channels, is given by:

$$\begin{aligned} G\uparrow\uparrow &\propto D_1^{\uparrow}(E_F)D_2^{\uparrow}(E_F) + D_1^{\downarrow}(E_F)D_2^{\downarrow}(E_F) \\ G\uparrow\downarrow &\propto D_1^{\uparrow}(E_F)D_2^{\downarrow}(E_F) + D_1^{\downarrow}(E_F)D_2^{\uparrow}(E_F) \end{aligned} \tag{2.1}$$

where $D_1^{\uparrow}$, $D_2^{\uparrow}$, and $D_1^{\downarrow}$, $D_2^{\downarrow}$ are the density of states (D) of the majority and minority electrons of the two electrodes (FM 1, FM 2), respectively. The TMR is therefore defined as:

$$TMR = \frac{R\uparrow\downarrow - R\uparrow\uparrow}{R\uparrow\uparrow} = \frac{G\uparrow\uparrow - G\uparrow\downarrow}{G\uparrow\downarrow}, \tag{2.2}$$

being R=1/G.

Ferromagnetic metals such as Ni, Co and Fe and their alloys have a strong spin imbalance which is modeled by splitting in energy the bands for spin up and spin down electrons. The spin polarization (P) is a measure of the

spin imbalance of a FM at the Fermi level. Defining the spin polarization of electrons (P) in function of the density of states of both electrodes at Fermi level:

$$P = \frac{D^{\uparrow}(E_F) - D^{\downarrow}(E_F)}{D^{\uparrow}(E_F) + D^{\downarrow}(E_F)}, \tag{2.3}$$

the theoretical TMR value can be determined in function of the electrodes polarization:

$$TMR = \frac{2P_1P_2}{1 + P_1P_2}. \tag{2.4}$$

In all these calculations, the electrodes are considered independent. In fabricated devices with usual barrier materials, the TMR will not be exactly given by the expression above since there are interactions between the two ferromagnetic electrodes. Therefore, a more generalized model was developed by Slonczewski [104] and Kubo/Laudauer [76]. However the theoretical model suggests that FM materials with large spin polarizations are required to achieve higher TMR. The highest polarization values are obtained with transition metal ferromagnets.
In figure 2.2 a schematic representation of the TMR process is shown. In case of antiparallel configuration the resistance is the highest because the electrons, flowing towards the top electrode, see fewer available states respect to the parallel configuration.

2.1.2 I-V characteristic

A current flows through the MTJ if a bias voltage is applied. For very low bias voltages $V \sim 0$ and assuming only tunnelling conductance, the current can be calculated using the following expression (Simmons [102]):

$$I = k_0 k_1 \frac{AV\sqrt{\phi}}{2t} exp[-k_1 t\sqrt{\phi}] \tag{2.5}$$

with

$$k_0 = \frac{q^2}{2\pi h} \quad and \quad k_1 = \frac{4\pi\sqrt{2m}}{h}\sqrt{e} \quad , \tag{2.6}$$

where A is the MTJ area, t the barrier thickness, ϕ is the effective barrier height (i.e. the difference between the electrode Fermi level and the conduction band of the insulator), q the electron charge, m the electron mass, and h Planck's constant. This expression shows that for low voltages the MTJ has the same IV characteristic of a resistor.

However in several applications (including biochips) higher voltages are applied to the MTJ. In that case, the MTJ I-V characteristic can also be calculated in the framework of Simmons' model:

$$I = k_0 \frac{A}{t^2} \cdot \Big[(\phi - V/2)exp[-k_1 t\sqrt{\phi - V/2}] - (\phi + V/2)exp[-k_1 t\sqrt{\phi + V/2}]\Big]. \tag{2.7}$$

The expression 2.7 is linear for $V \ll \phi$, and becomes cubic ($I \propto \alpha V + \beta V^3$) for sightly higher potential (see fig. 2.3).
In conclusion the current depends exponentially on the barrier thickness and on the square root of the barrier height.

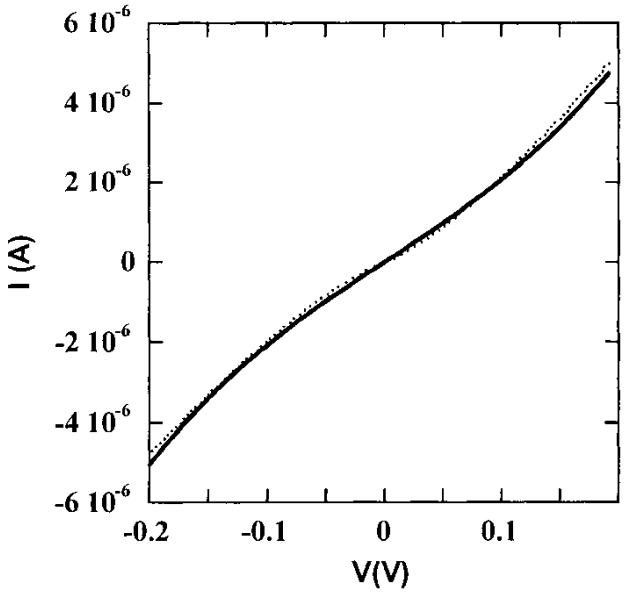

Figure 2.3: I-V characteristics at T = 13 K for a tunnel junction of the type CrO_2/barrier layer/Co fitted to the Simmons model (solid black line) [10].

2.1.3 Parameters influencing the TMR

RxA product

A common figure of merit for MTJs is the resistance area product (RA). The RA product is a characteristic that only depends on the barrier thickness,

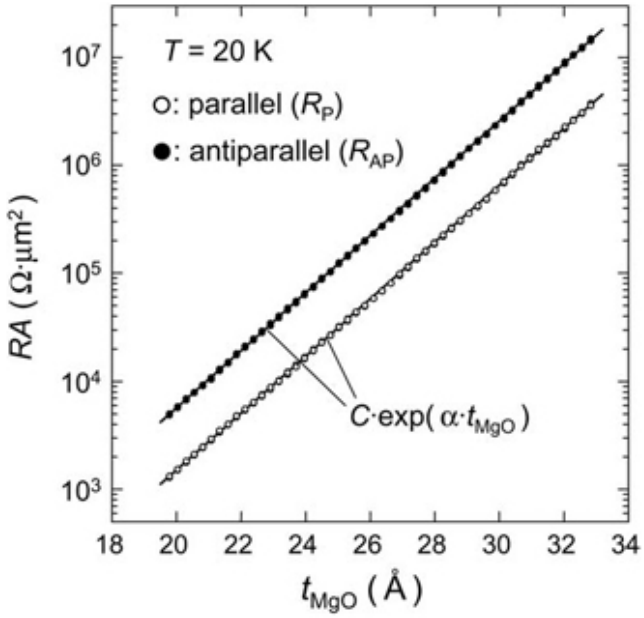

Figure 2.4: MgO-thickness dependence of resistance-area (RA) product for parallel (R_P) and antiparallel (R_{AP}) configuration at T = 20 K for an epitaxial Fe/MgO/Fe junction. Adapted from[125].

increasing exponentially with it (from a simple calculation in equation 2.7), as depicted in figure 2.4. Indeed, for a fixed barrier thickness, the MTJ minimum resistance is inversely proportional to the junction area. This results from the fact that the number of tunnelling electrons are directly proportional to the total electrode area. The higher the area is, the higher the tunnelling current will be, therefore the lower the resistance will be.
The RA product of MTJs with the same barrier thickness is constant, thus allowing the comparison of different devices. This fact permits to choose the area and the resistance of the sensor independently: an adequate sensor area can be chosen for a certain application while a sensor resistance can be chosen for optimizing the sensor signal-to-noise ratio. However there are some limitiations: for example a high junction's active area could enhance the risk of defects that would lead to a loss in the TMR.
The RA product is commonly expressed in $\Omega\mu m^2$ and can be tuned from $M\Omega\mu m^2$ down to few $\Omega\mu m^2$, by decreasing the insulator thickness from 2nm down to 0.8 nm. In this thesis, junctions with RA product varying from 3000 $k\Omega\mu m^2$ to 25 $k\Omega\mu m^2$ have been obtained, decreasing the MgO thickness from

2nm down to 0.9 nm.

Bias voltage

The TMR of a magnetic tunnel junction depends on the applied voltage. The TMR is almost constant until 25-30 mV, then it starts to decrease with increasing bias voltage. In the range where the signal drops until half of the initial TMR (between 300-500mV), the decrease is almost linear.
The decrease of the TMR is due to the presence of defects in the barrier which starts to conduct as the voltage increases, or in the opening of new conductive channels, which reduce the tunneling. Different models were proposed to explain the dependence [127], [16], [129], [128], [15]. One of the models which correctly predicts the TMR behaviour for many junctions was proposed by Zhang *et al*, [128]. When the bias voltage increases, the "hot electrons", having an excess of energy eV, can disexcite transferring this energy excess to collective excitation of local spins, the magnons. This causes spin flip events and spin mixing and therefore the decrease in the polarization and thereby in the TMR.
The barrier of the MTJ is a dielectric which can be electrically disrupted if the bias voltage increases beyond a certain value. In this regime pinholes are formed providing direct low resistance metallic conduction, resulting in the lost of TMR. The voltage at which this phenomenon occurs is called the *breakdown voltage* and is related to the dielectric strength of the insulator.

Temperature

The temperature dependence of TMR greatly exceeds the temperature dependence of non magnetic tunnel junctions. It tends to decrease for all kinds of MTJs, of about 25% from 4.2 K to 300 K because of the corresponding decrease of the spin polarization induced by the spin-wave excitations [29]. The model which reproduces better the TMR behaviour, is the classical $T^{3/2}$ Bloch law. Furthermore, for a more accurate model, one has to take into account the non-polarized excited conduction channels created increasing the temperature, which cause an increase of the conductivity and a reduction of the TMR ratio.

2.2 Sensor engineering

The operation of a TMR junction is based on the use of many different layers, whose thickness and material are specially chosen. Indeed the typical stack of a TMR junction consists, not only of the real magnetic tunnel junction, but also of many other layers (in total 11, see figure 2.5 and figure 3.11 in chapter 3 for the thicknesses), each with its functionality. In particular there are: the buffer and capping layers (Ta/Ru/Ta and Ru/Ta), the exchange biased synthetic antiferromagnet layers (IrMn/CoFe/RuSAF/CoFeB) and the real magnetic tunnel junction.

The buffer layers are crucial for having high TMR values, because affect the

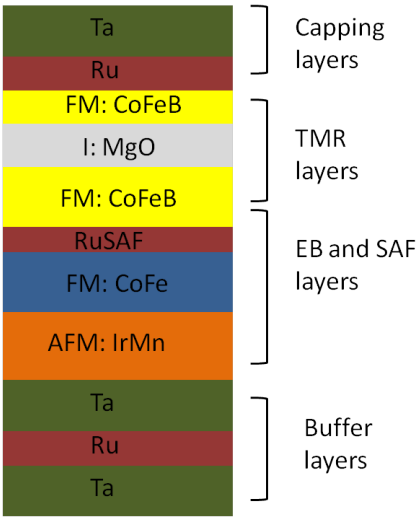

Figure 2.5: Typical stack of a TMR junction.

crystallization of the bottom CoFeB junction layer [121]. The capping layers instead, not only promote the crystallization of the top CoFeB junction layer [58], but also have the important function of protecting the magnetic tunnel junction.

The exchange biased synthetic antiferromagnet layers consist in a (FM2/ NM/ FM1/AFM) structure that exploits two important interface phenomena: the exchange bias and bilinear coupling. Instead of the conventional FM/AFM, the ferromagnet FM1 is directly pinned by the antiferromagnet (AFM) by exchange bias, and the FM2 is antiferromagnetically pinned to FM1 by bilinear coupling, becoming the pinned layer of the MTJ. This

structure has some important advantages respect to a conventional exchange biased junction. It is used to improve the exchange field [53] and to enhance the thermal stability, since the presence of the spacer in the SAF prevents interdiffusion. The magnetic stability is also improved by increasing the exchange bias field. Moreover, the SAF is used to reduce the effective moment of the pinned layer [115] and thereby the external magnetostatic field that shifts the free layer response. Therefore it is important to engineer all the thicknesses of the SAF structure in order to obtain the best performances. In this regard in chapter 5 a comparison between junctions with unbalanced and balanced SAF structure will be presented.

The exchange bias and bilinear coupling are presented in detail below. Moreover the description of another interface phenomenon, the Néel coupling, is presented, as it will be useful in the characterization and analysis of the transfer curve of the sensors grown during the thesis work.

2.2.1 Exchange Bias

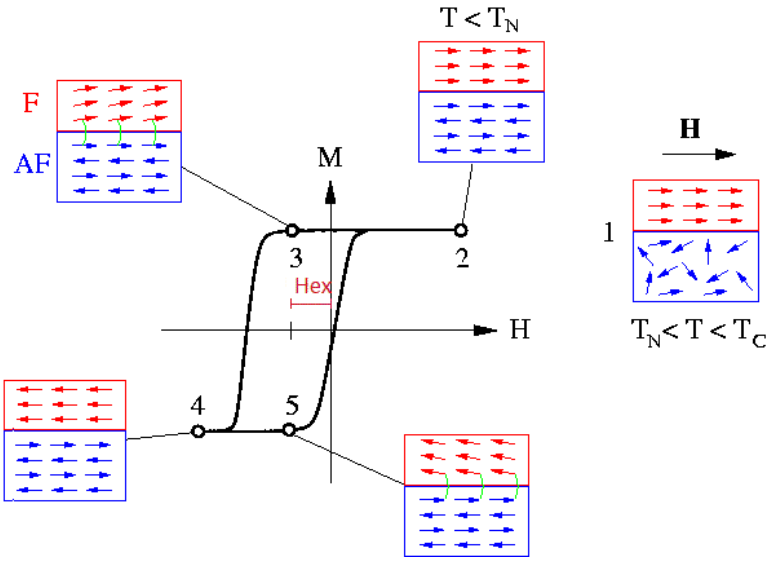

Figure 2.6: Schematic diagram of the spin configuration of a FM/AFM bilayer at the different stages (1-5) of an exchange biased hysteresis loop.

The exchange bias is an exchange interaction that is observed at the interface between a ferromagnetic and an antiferromagnetic material. To observe

this phenomenon a ferromagnetic layer has to be grown on an antiferromagnet at an intermediate temperature between the Néel temperature and the Curie temperature ($T_N < T_C$), with an applied magnetic field (stage 1 in figure 2.6). Therefore the ferromagnet will be forced its magnetization to orientate along the field direction. The system is then field cooled below the Néel temperature, fig. 2.6, stage 2, so that the AFM interfacial spins align ferromagnetically to the FM, to minimize the exchange energy. All the other spins, away from the interface, follow the standard AFM order. Applying a variable magnetic field (parallel to the direction of the field cooling) the resulting hysteresis loop will be not be centered, but shifted from the origin by an amount Hex, the *exchange bias field*, in the opposite direction of the cooling field. Therefore, the AFM spins at the interface determine a microscopic torque on the FM spins, to keep them in their original position fig. 2.6, stage 3. The hysteresis loop of fig. 2.6 is obviously due to the magnetization of the ferromagnet (the antiferromagnet on the other hand, has no net magnetization) and it is shifted as a result of the unidirectional anisotropy, that acts as an extra biasing field.
This phenomenon is used with an AFM/FM system in the TMR sensors to force the magnetization of the reference layer. The AFM layer is usually called the pinning layer and the FM the pinned layer. In this thesis the AFM/FM system used consists of IrMn/Co_{40} Fe_{40}. The antiferromagnet used is IrMn, 20nm thick, because it provides both high exchange bias magnitudes and good thermal stability [38].

2.2.2 Bilinear Coupling

The antiferromagnetic coupling between two ferromagnetic layers separated by a thin nonmagnetic spacer was first observed by Grünberg in 1986 [44]. The greatest interest has been in the simplest form of the coupling, called bilinear because the energy per area is linear in the directions of both magnetizations $\hat{m}_i$:

$$\frac{E}{A} = -J\hat{m}_1 \cdot \hat{m}_2, \tag{2.8}$$

where the interlayer coupling constant J is given by the difference in energy between the antiparallel and the parallel alignment of the magnetizations:

$$J = \frac{1}{2A}(E_{anti} - E_{par}). \tag{2.9}$$

With this form of the interaction expression, positive values of the coupling constant J favour parallel alignment of the magnetizations and negative values favour antiparallel alignment.
The discovery that the sign of J, and hence the preferred alignment of the magnetizations, oscillates as the thickness of the spacer layer is attributed to Parkin [87]. By 1993, there were a number of theoretical models for interlayer exchange coupling, and all gave the result that the Fermi surface of the spacer layer material determined the coupling periods. The models showed that the critical spanning vectors of the Fermi surface of the spacer-layer material determine the oscillation periods [114] [18]. A spanning vector of the Fermi surface is a vector parallel to the interface normal that connects two points on the Fermi surface, one point having a positive component of velocity in the interface direction and the other a negative component. A critical spanning vector is a spanning vector that connects two sheets of the Fermi surface at a point where they are parallel to each other, see fig. 2.7.
In 1993, a model for interlayer exchange coupling [108] [17], based on spin-

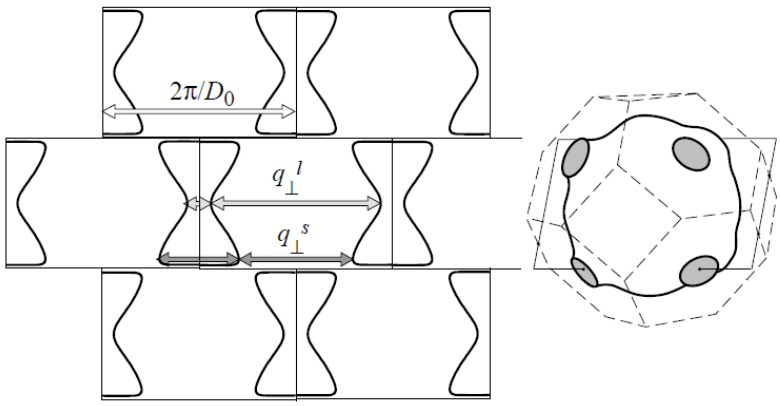

Figure 2.7: Critical spanning vectors for Cu in the 100 direction. The right panel shows a representation of the Cu Fermi surface and a rectangular slice (solid line) through it. The necks in the (111) directions are indicated in gray. The dashed lines indicate the bulk Brillouin zone. In the left panel, the rectangular slice from the right panel is repeated periodically. There, the heavy curves show the Fermi surface of Cu in that slice. The white arrow gives a 1-dimensional reciprocal lattice vector in the interface direction. The gray arrows give the critical spanning vectors (for both the long (l) and short (s) period).

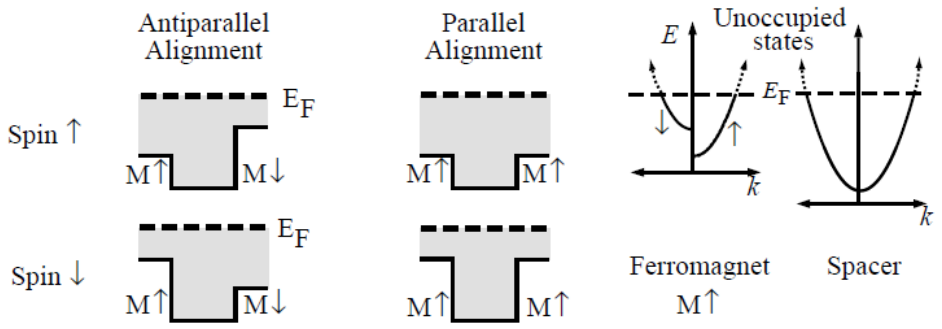

Figure 2.8: Quantum wells used to compute interlayer exchange coupling. On the right, the two panels give typical band structures for free electron models of interlayer exchange coupling. On the left, the four panels give the quantum wells for spin up and spin down electrons for parallel and antiparallel alignment of the magnetizations.

dependent reflection at interfaces between the spacer and the ferromagnetic layers, was provided, unifying all the previous models. In a simple picture, for free electron model, our system can be described as a one-dimensional quantum well where the heights of the two potential steps, created by the ferromagnet/spacer interfaces, are spin dependent (figure 2.8). Electrons reflect from interfaces, and the multiply reflected waves interfere with each other. The total amplitude for n round trips in the spacer layer is:

$$\sum_{n=1}^{\infty}[e^{i2kD}R_R R_L]^n = \frac{e^{i2kD}R_R R_L}{1 - e^{i2kD}R_R R_L}, \tag{2.10}$$

where D is the spacer layer thickness, k is the electron wavevector, $R_{R(L)}$ is the reflection coefficient for the right (left) interface and e^{i2kD} is the phase accumulated in a roundtrip.
The denominator becomes zero and there is constructive interference whenever $2kD + \phi_R + \phi_L = 2m\pi$, where m is an integer and $\phi_{R(L)}$ is the change in the phase of the reflected electron. This constructive interference inside the spacer layer gives rise to resonances, frequently referred to as quantum well states. Whenever the reflection probability is one, these quantum well states are true bound states, otherwise they are like bound states that are broadened by transmission into the ferromagnetic layers (fig. 2.9). As the thickness D of the spacer layer is varied, the resonances and bound states shift

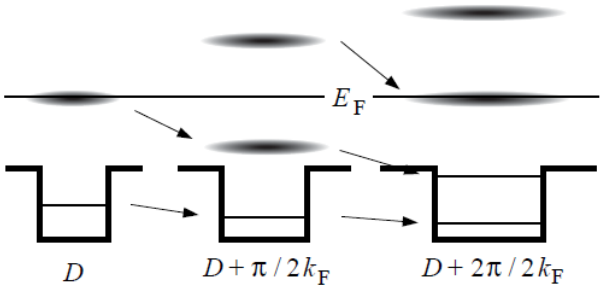

Figure 2.9: Evolution of quantum well resonances with spacer layer thickness. The lines are the bound states, and the fuzzy ellipses are the resonances for quantum wells of increasing thickness.

in energy. If there is a resonance at the Fermi energy at a thickness D, then resonances cross the Fermi energy whenever the thickness is $D + 2n\pi/2k_F$, where k_F is the Fermi wave vector of the spacer layer and n is an integer. This periodic crossing of the Fermi energy by quantum well resonances is the origin of the oscillations in the interlayer exchange coupling. Indeed these quantum well states affect the density of states in the trilayer, and hence the system's energy, on which J depends. In this 1-d model, the Fermi surface consists of two points, $k = \pm k_F$, and the period of the oscillations is determined by the spanning vector of the Fermi surface, $2k_F$. The change in the density of states of the quantum well for each spin can be derived [17]:

$$\Delta E = \frac{1}{\pi} Im \int_{-\infty}^{E_F} ln(1 - e^{i2kD} R_R R_L)\, dE. \tag{2.11}$$

For a fixed thickness D, the integrand oscillates rapidly through the energy dependence of k. All these oscillations cancel out in the integration, except those close to the Fermi energy, where there is a sharp cut-off. The only contribution is from a range of states near E_F of width proportional to $\hbar v_F/D$, where v_F is the Fermi velocity. Assuming a large spacer thickness D (larger than one oscillation period) and low reflection coefficients $R_{R(L)}$, the expression of the total change in energy becomes:

$$\Delta E \approx \frac{\hbar v_F}{2\pi D} |R_R R_L| cos(2k_F D + \phi_R + \phi_L), \tag{2.12}$$

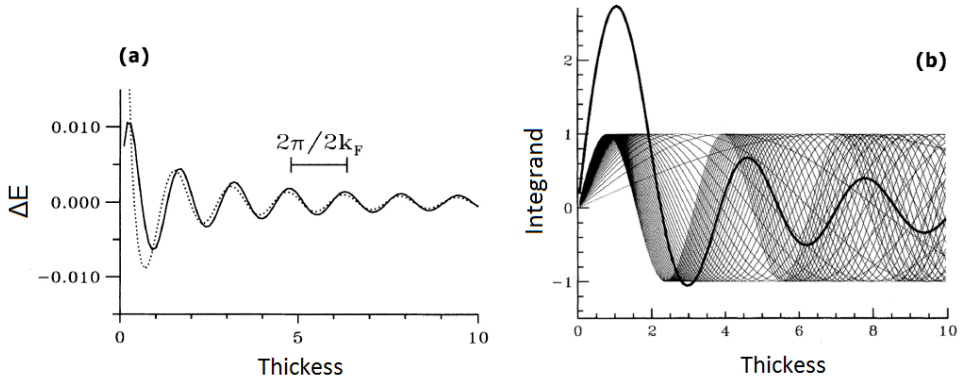

Figure 2.10: In (a), total energy change due to a quantum well filled to the Fermi level. The solid line shows the energy, the dotted line shows the approximated form for large D in eq. 2.12. In (b), illustration of an integration of sinusoids with different periods. The peaks in the heavy curve come from constructive interference among some of the light curves [108].

which is a damped oscillation of period $2\pi/2k_F$ (fig. 2.10). As the thickness increases, fewer and fewer of the integrated functions interfere constructively, resulting in lower peaks.

The interlayer exchange coupling is then the sum of the energies for the four different quantum wells seen in fig. 2.8. All four quantum wells have cohesive energies that oscillate with the same period, determined by the Fermi surface spanning vector of the spacer layer material, that is spin-independent. For this one-dimensional case, in the large D, small R limit, the result for J is:

$$\begin{aligned} J &\approx \frac{\hbar v_F}{4\pi D} Re[(R_\uparrow R_\downarrow + R_\downarrow R_\uparrow - R_\uparrow^2 - R_\downarrow^2) e^{i2k_F D}] = \\ &= -\frac{\hbar v_F}{4\pi D} Re[(R_\uparrow - R_\downarrow)^2 e^{i2k_F D}], \end{aligned} \tag{2.13}$$

where $R_{\uparrow(\downarrow)}$ is the reflection amplitude for majority (minority) spins and is supposed equal for the left and for the right interface.

Thus, the oscillatory coupling in magnetic bilayers, spaced by a non magnetic layer, arises as a consequence of the oscillatory nature of the quantum well energy, due to the response of the metal electrons at the Fermi surface, and the oscillation period of the interlayer exchange coupling is determined by the critical spanning vectors of the Fermi surface.

Real multilayers are three dimensional, not one dimensional. However, if the interface is coherent and there are no defects, the multilayer is periodic in the two directions parallel to the interface. Then, the crystal momentum parallel to the interface is conserved. In this case, the problem simplifies to a two-dimensional set of independent one-dimensional quantum wells. The cohesive energy is just the integral over the interface Brillouin zone (IBZ) of a series of one-dimensional quantum well energies. Even in this case the oscillation period of the interlayer exchange coupling is found to be determined by the critical spanning vectors of the Fermi surface [108].

2.2.3 Néel Coupling

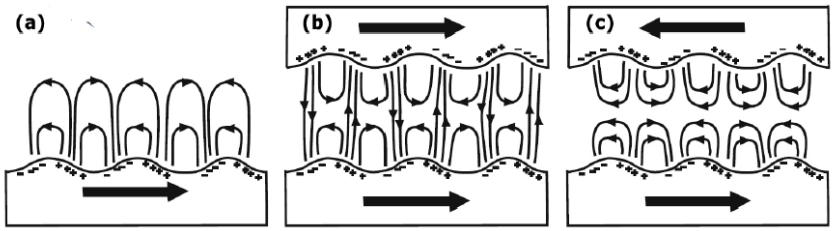

Figure 2.11: Orange peel coupling from correlated roughness. Fringe field and magnetic "charges" in case of a rough surface (a), of two separated magnetic layers with parallel magnetizations (low energy configuration) (b) and of two separated magnetic layers with antiparallel magnetizations (high energy configuration) (c) [14].

The Néel coupling, or Orange Peel coupling, is a ferromagnetic coupling between two magnetic layers separated by a non-magnetic spacer and it is induced by the magnetostatic interaction between the magnetic poles at rough interfaces. It was first studied by Néel in 1962 [78] and then the model was further refined by Zhang [126] and Kools [64].
When the surface of a ferromangetic material is rough, magnetic poles arise and it is possible to describe the magnetic configuration at the interfaces with distributions of magnetic "charges":

$$\sigma(\mathbf{R}) = \mathbf{M} \cdot \mathbf{n}(\mathbf{R}), \tag{2.14}$$

where ($\mathbf{M}$) is the magnetization of the layer (which is uniform in the plane)

and $\mathbf{n}(\mathbf{R})$ is the normal to the surface (which changes due to the corrugation with the position on the surface $\mathbf{R}$). Ferromagnetic coupling arises from the fact that, if the two magnetizations are aligned ferromagnetically, also the magnetic charges will be locally opposite, thus minimizing the magnetostatic energy of the system (2.11 (b)).
The total strenght of the coupling is determined by the interlayer coupling energy: $J = \mu_0 M_F t_F H_p$, where H_p is the effective offset field which pins the magnetization of the free layer to the one of the bottom layer:

$$\begin{aligned} H_p = &\frac{\pi^2 h^2 M_p}{\sqrt{2}\lambda t_F} \cdot \left[1 - exp\left(-\frac{2\pi\sqrt{2}t_F}{\lambda}\right)\right] \cdot \\ &\cdot \left[1 - exp\left(-\frac{2\pi\sqrt{2}t_p}{\lambda}\right)\right] \cdot exp\left(-\frac{2\pi\sqrt{2}t_s}{\lambda}\right). \end{aligned} \tag{2.15}$$

In this expression $M_{F(p)}$ is the saturation magnetization of the free (pinned) layer, λ is the period of the roughness oscillation, t_F is the thickness of the free layer, t_s the thickness of the spacer and t_p is the thickness of the pinned layer. The exponential dependence of the coupling on the layers' thickness is due to the limited range of the dipolar interactions. Increasing the spacer thickness weakens the ferromagnetic coupling, because it weakens the interaction beween poles with opposite sign.
In TMR sensors with reduced thickness of the spacer layer (e.g. MgO), the Orange Péel coupling favours an undesirable ferromagnetic alignment between the pinned and the free layer altering the field response of the sensor, as it will be seen in section 5.2.

2.3 Linearization of a MTJ sensor

The resistance field curve (called transfer curve) of a MTJ is obtained by applying a voltage drop across the system FM/I/FM while varying the magnetic field. For an angle θ between the magnetization direction of the two electrodes, the total resistance of the MTJ is given by:

$$R(\theta) = \frac{R\uparrow\uparrow + R\uparrow\downarrow}{2} + \frac{R\uparrow\uparrow - R\uparrow\downarrow}{2}\cos(\theta). \tag{2.16}$$

If the magnetization of the free layer varies linearly with the applied magnetic field, that is, if $\cos(\theta)$ linearly varies, then a linear curve R(H) is obtained.

For sensing small fields the critical parameter is the sensor field sensitivity S_{sensor}, which corresponds to the slope of the transfer curve. Considering the sensor resistance change $\Delta R_{\Delta H}$ for the sensor linear field range ΔH, S_{sensor} is defined by:

$$S_{sensor} = \frac{\Delta R_{\Delta H}}{R_0} \frac{1}{\Delta H}, \tag{2.17}$$

where R_0 is the resistance at zero external field.
Maintaining high field sensitivity with reduced hysteresis is a challenge for sensor devices with linear response. This can be achieved by controlling of the shape anisotropy [69], or changing the free layer thickness, with certain compromise on the junction TMR. In particular linear and hysteresis-free behaviour is observed in junctions using CoFeB/MgO/CoFeB with a thickness of the top CoFeB lower than 1.5nm [61], [120]. In this case, in fact, the material exhibits a superparagnetic behavior, i.e. a paramagnetic behaviour with a very high magnetic susceptibility.
In the next two paragraphs, the conditions for a linear transfer curve of a MTJ sensor are described, in the ideal case of the free layer being mono-domain [20].

2.3.1 Parallel and crossed anisotropies

Thanks to simple energy considerations it is possible to identify the conditions for the linearity of the sensor. In the assumption that the free layer is a single magnetic domain (i.e. in the case of an annealed film of CoFeB and device dimensions less then $1{\times}1$ μm^2 [20]), the energy of the free layer normalized by its volume can be calculated considering the sum of the following energy terms:

- Zeeman term: this is the energy possessed by the sample in an external applied field. This can be expressed as: $-\mu_0 H \cdot M^f$ where H is the external applied field, and M^f is the magnetization of the free layer.
- Magnetocrystalline anisotropy term: this is the work needed to align the magnetization along one direction starting from the esay axis, that is the cristallographic direction along with the sample's magnetization aligns easier because of anistropy. This can be expressed as: $K \sin^2\theta$ or $K \cos^2\theta$ (the first, in case of parallel anisotropies, and the latter in case of crossed anisotropies, figure 2.12), where $K = \frac{1}{2}\mu_0 H_k M_s^f$ and

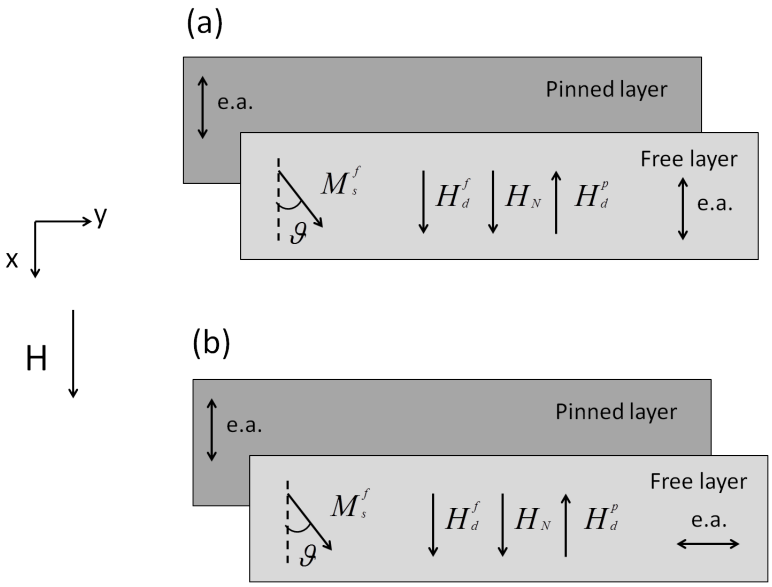

Figure 2.12: Scheme of the sensor composed by a pinned layer and a free layer with (a) parallel anisotropies and (b) crossed anisotropies.

M_s^f is the saturation magnetization of the free layer.

- Demagnetizing field of the free layer: this is the field that is produced inside the material, having finite dimensions, to counteract the stray field generated by magnetic poles at the sample's surfaces. It can be expressed as: $-\frac{1}{2}\mu_0 H_d^f \cdot M^f$, where H_d^f is the demagnetizing field of the free layer.

- Demagnetizing field of the pinned layer: $-\mu_0 H_d^p \cdot M^f$, where H_d^p is the demagnetizing field of the pinned layer.

- Néel term: this term is due to the Néel Coupling and can be expressed as: $-\mu_0 H_N \cdot M^f$, where H_N is the Néel field.

For some geometries the demagnetizing field can be calculated [23] [54]. In this case of thin film, the demagnetizing field can be assumed to be: $H_d^f = -N_{xx} M_s^f \cos\theta$, where N_{xx} is the xx component of the demagnetizing matrix N. Therefore the energy can be calculated and also the related minima, by means of the first and second derivative of the energy.

Parallel anisotropies

$$\frac{E_f}{V} = \mu_0 M_s^f \left[\frac{1}{2} \sin^2\theta (H_k - N_{xx} M_s^f) + \right. \\ \left. + \frac{1}{2} N_{xx} M_s^f - \cos\theta (H - H_d^p + H_N) \right] \tag{2.18}$$

Solutions:

1. $\sin\theta = 0 \Leftrightarrow \theta = 0 \; or \; \pi$
2. $H_k - N_{xx} M_s^f = 0$ and $H - H_d^p + H_N = 0$
3. $\cos\theta = (H - H_d^p + H_N)/(N_{xx} M_s^f - H_k)$

If $H_k > N_{xx} M_s^f$, the magnetic response of the sensor is that described as in figure 2.13 (a). As observed, the component $N_{xx} M_s^f - H_k$ defines the field at which the state change occurs, while$H_d^p - H_N$ shifts the whole curve.
If $H_k < N_{xx} M_s^f$, a linear magnetic response curve is obtained (fig. 2.13 (b)). This arises because in the first case the magnetic field is applied parallel to the easy axis of the free layer, while in the second case is applied perpendicular to it.

Crossed anisotropies

$$\frac{E_f}{V} = \mu_0 M_s^f \left[\frac{1}{2} \cos^2\theta (H_k + N_{xx} M_s^f) - \cos\theta (H - H_d^p + H_N) \right] \tag{2.19}$$

Solutions:

1. $\sin\theta = 0 \Leftrightarrow \theta = 0 \; or \; \pi$
2. $\cos\theta = (H - H_d^p + H_N)/(N_{xx} M_s^f + H_k)$

Contrary to the parallel anisotropies, in this case a linear magnetic response curve is the only possible solution because the magnetocrystalline easy axis of the free layer is parallel to the long edge, so both shape and magnetocristalline anisotropies favour the alignment along the same direction (fig. 2.13 (c)). As observed, the component $N_{xx} M_s^f + H_k$ defines the field at which the response starts to be linear, while $H_d^p - H_N$ shifts the whole curve.

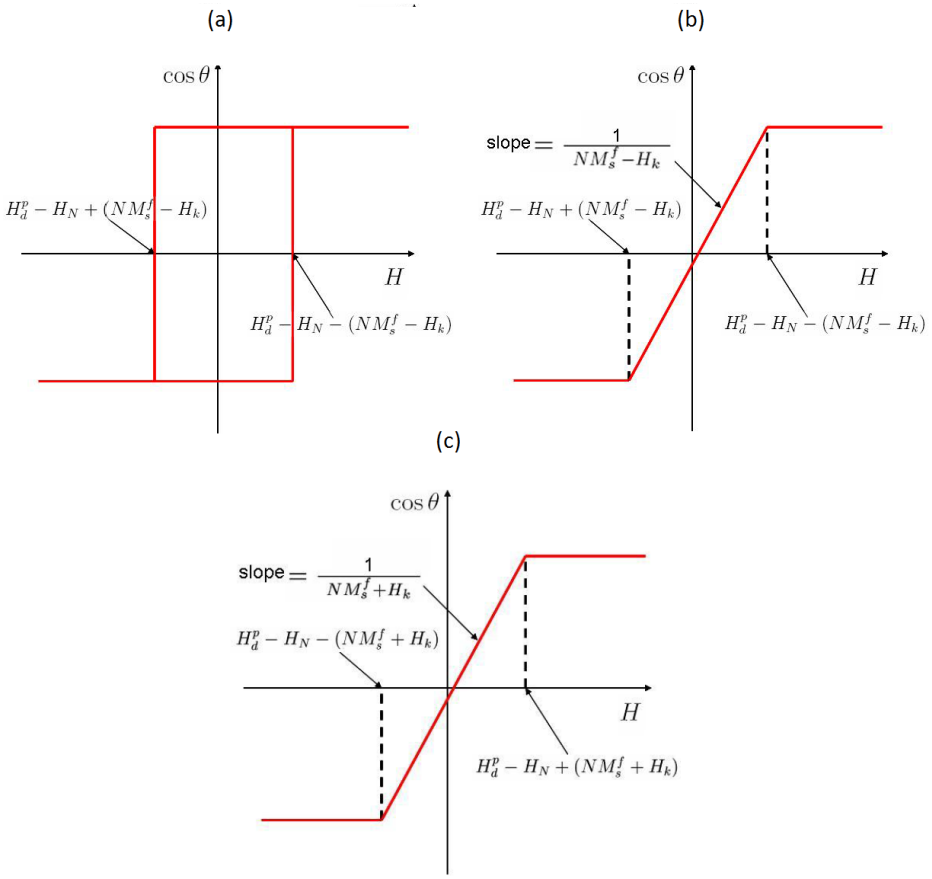

Figure 2.13: Transfer curves of the sensor in case of (a) parallel anisotropies and $H_k > N_{xx}M_s^f$, (b) parallel anisotropies and $H_k < N_{xx}M_s^f$, (c) crossed anisotropies.

The sensitivity of the sensor is proportional to the slope $(1/(NM_s^f + H_k))$. An increase of the demagnetizing field will reduce the slope and therefore the sensor sensitivity. In principle in this configuration the sensor should be designed to have no demagnetizing field. However, the demagnetizing field is important to stabilize the free layer and achieve a linear sensor.

2.3.2 Superparamagnetism

Consider a magnetic particle of volume V, so small that it is a signle-domain, with magnetocrystalline or shape anisotropy described by an energy density term: $E_a = K \sin^2 \theta$. If the activation energy KV for flipping its magnetiza-

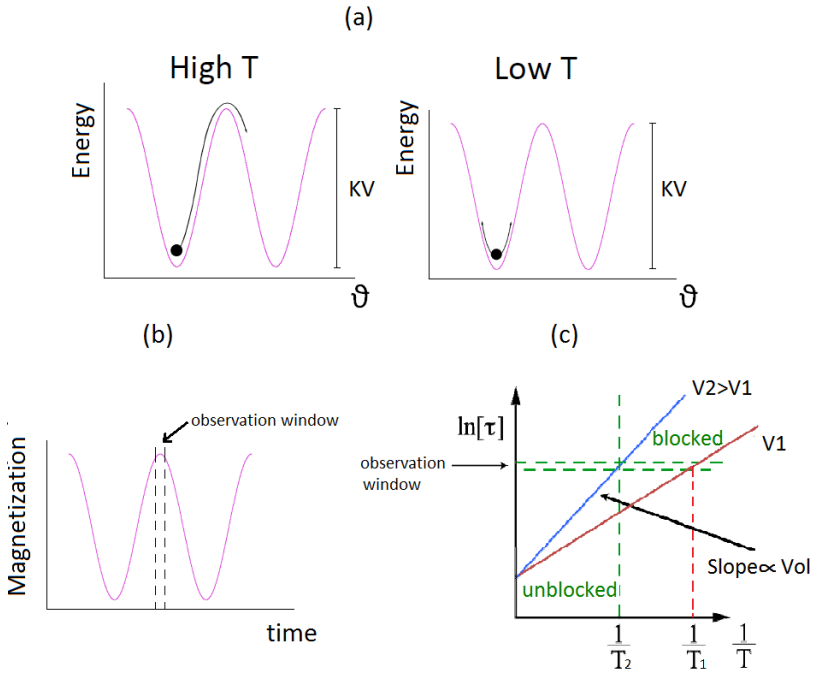

Figure 2.14: (a) Magnetization flipping by thermal fluctuations; (b) observation window for having the particle blocking in one of its magnetic states; (c) $\log(\tau)$ versus $\frac{1}{T}$ for two values of particle volume V.

tion from $\theta = 0$ to $\theta = \pi$ is small compared to K_BT, the magnetization is continuously flipped by thermal fluctuations, while if it is big the magnetization is blocked in one of its minima (fig. 2.14 (a)).
After application of a magnetic field the particle magnetization undergoes a relaxation with a characteristic time:
$\tau = \tau_0 exp\left(\frac{KV}{k_B T}\right)$, where $\tau_0 \sim 10^{-9}$ s.
The particle will appear blocked if the measuring time t is much smaller than τ (fig. 2.14 (b)). A commonly used criterion for blocking is $\Delta/k_B T_b$, where T_b is the blocking temperature below which the fluctuations vanish. This situation corresponds to τ ∼100s, i.e. above the time requirement for a magnetic moment measurement.
In figure 2.14 (c) the trend of the logarithm of τ with respect the inverse of temperature is shown. It explains the superparamagnetic behaviour of an ensemble of non-interactive magnetic particles. Indeed from the previous equation a linear dependence of $log\tau$ with respect 1/T is clear: $log\tau =$

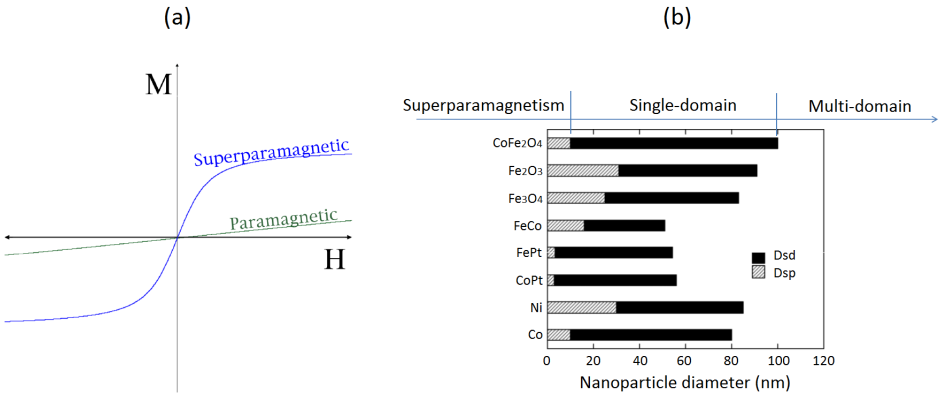

Figure 2.15: (a) Comparison between the curves M(H) of a paramagnet and a superparamagnet and (b) size effect on the magnetic behaviour for different materials [65].

$log\tau_0 + KV/k_BT$; as the angular coefficient increases, that is the volume V, 1/T decreases and consequently T increases with the risk of going out to the observation window. For this reason, reducing the particle's volume is necessary. A particle with a very small volume can be considered as a single domain having zero average magnetization. When a cluster of these particles is created and a magnetic field is applied, it will behave as a paramagnet with giant magnetic moment m of each particle (fig. 2.15 (a)). In figure 2.15 (b) the size effect on the magnetic behaviour for different materials is shown. In FeCoB films the superparamagnetic condition is achieved with layer thickness below 1.5 nm, condition in which, due to the low wettability of the underlayer MgO, the CoFeB has granular nature.

The sensitivity of the samples grown during this thesis work results from the combined effect of the shape anisotropy and the superparamagnetic behaviour of the top $Co_{40}Fe_{40}B_{20}$ layer, leading to an easy axis of the top free layer perpendicularly aligned to that of the reference layer. However, experimentally, a mixture of linear response and hysteresis has been observed: loops with a maximum coercive field of about 10 Oe and a minimum of 4 Oe have been measured. This can be probably ascribed to the fact that the free layer of the MTJ not behaves exactly as a mono-domain.

2.4 MTJ Sensor Noise

Noise in TMR structures is mainly composed of white noise (flat in frequency) and 1/f noise. The noise is related with the tunneling through the barrier of the MTJ and with magnetic fluctuations on the sensing magnetic layer, which vary as the inverse of the area of the MTJ. Therefore, the quality of the barrier and the magnetic materials used are crucial for reducing noise in a MTJ sensor.
In a MTJ the white noise is composed by shot and thermal noise. The shot and thermal noise are related and can not be treated as separated processes. The Johnson noise [62], [82], also called thermal noise, corresponds to the random voltage caused by thermal fluctuations of the electric charge. Shot noise, first described by Schottky [97] [96], is associated with the tunneling across the barrier and is caused by the quantization of charge carriers. The shot noise increases with the sensing current, and therefore with the bias voltage, [100] [101], and is also dependent on the quality of the barrier [39]. The noise spectral density that takes into account both the noise contributions (thermal and shot) can be expressed as follows [21]:

$$S_v^W(V^2/Hz) = 2eIR^2 \coth(eV/2k_BT). \tag{2.20}$$

In zero bias voltage limit $V \to 0$, the equation above tends to $4Rk_BT$, corresponding to the Johnson expression.

Almost all electronic devices exhibit voltage fluctuations with a power spectral density, inversely proportional to frequency. These voltage fluctuations are commonly called the 1/f noise, that limits the low frequency magnetic field detectivity. This noise is predominant at low frequencies and from a certain frequency called the 1/f knee, the white noise background starts to be the dominant noise. The 1/f noise voltage spectral density can be described phenomenologically by the Hooge formula [57] [56], which was determined empirically:

$$S_v^{1/f}(V^2/Hz) = \frac{\alpha_H I_{bias}^2 R_0^2}{fA}, \tag{2.21}$$

where α_H stands for the modified Hooge constant for tunnel junctions, I_{bias} is the sensor bias current, R_0 the dynamic resistance at the operating point, A the area of the junction and f the frequency.

The origin of the 1/f noise in MTJ is associated with reconfiguration of the domain structures due to thermal activation [83] [119], and it is observed to scale inversely proportional to the volume of the magnetic sample [105].
The Hooge constant α_H depends on the state of the magnetization of the sensing layer which in turn depends on the applied magnetic field and the MTJ barrier thickness (related to the resistance area product (RA)). Since the MTJ noise depends on the bias conditions and area, α_H can be used to compare the intrinsic 1/f noise level of different sensors. Thinner MTJ barriers have lower α_H values which was observed in MTJ with MgO barriers deposited by Sputtering [81] [7], even if lower values, typically of one order of magnitude, were found in MgO MTJs obtained by molecular beam epitaxy (MBE) [6] [26].

The sensor noise level can be expressed in units of magnetic field that corresponds to the sensor field detection limit:

$$S_v(T/Hz^{0.5}) = \frac{\sqrt{S_v(V^2/Hz)}}{S_{sensor} I_{bias} R_0} \tag{2.22}$$

Where S_{sensor} (%/T) is the sensor field sensitivity, I_{bias} stands for the sensor bias current and R_0 the sensor dynamic resistance in the operating point.
Using equation 2.21 the expression above can be semplificated:

$$S_v(T/Hz^{0.5}) = \frac{1}{S_{sensor}} \sqrt{\frac{\alpha_H}{fA}}. \tag{2.23}$$

Consequently, to increase field detectivity:

1. The Hooge constant α_H must be minimized by improving the quality of MTJ barrier and in particular thin barriers (low resistance) must be chosen.

2. The sensor field sensitivity $S_{sensor} = \Delta TMR/\Delta H$ must be higher as possible, which means that the TMR must be maximized (acting on materials/barriers), and for the application in mind the field range ΔH must be minimized.

3. Whenever is possible the field source must be modulated in frequency since the sensor presents lower noise at higher frequencies.

4. Finally, the area must be maximized until the maximum spatial resolution allowed by the application.

Chapter 3

Experimental methods

In this chapter an overview of all the experimental methods used in this thesis work is presented. In the first section all the instruments and methods for the fabrication of the MTJ sensors are described, showing all the phases of the process flow and a detailed description of all the steps of optical lithography. In the second section the device characterization techniques, but also the experimental setups exploited for magnetoresistive and noise measurements are presented. Finally, the last section shows the instrumental apparatus and the method of double modulation that will be used for the biological assays of molecular recognition of chapter 6.

3.1 Instruments and methods for sample preparation

3.1.1 AJA Magnetron Sputtering

Magnetron sputtering is a physical vapour deposition technique that allows good film adhesion to the substrate and high control on the thickness, uniformity and composition of the deposited material. Figure 3.1 shows a schematic of the sputtering process.
During the process the sputtering material is ejected due to bombardment of ions to the target surface. Indeed the vacuum chamber is filled with an inert gas, frequently argon, and, by applying a high negative voltage to the target, a glow discharge is created, resulting in the acceleration of ions towards the target surface. All these charged particles are immediately accelerated by the target voltage and ionize, by collisions, the Ar atoms, leaving Ar^+

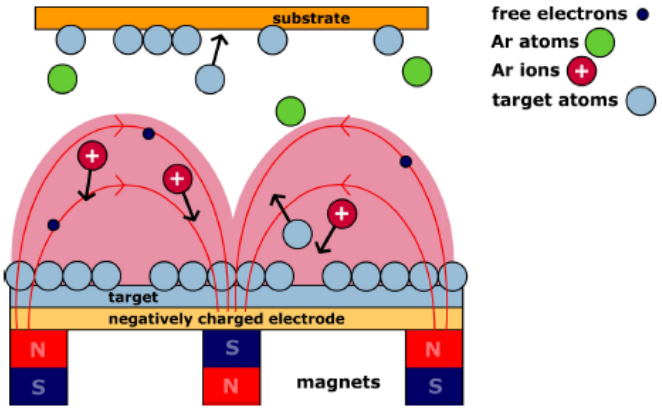

Figure 3.1: Schematic of the magnetron sputtering process.

ions and e^- free electrons, which in turn ionize other Ar atoms triggering a cascade process. At this point positively charged Ar^+ ions are accelerated towards the negatively charged electrode ejecting sputtering materials from the target surface. This results in a coating layer on the substrate, such as a Si wafer, that is placed in the path of these ejected particles, in front of the target. In magnetron sputtering, permanent magnets are put behind the target in order to trap the free electrons in a magnetic field directly above the target surface. The circular path of the free electrons along the lines of the magnetic field enhances the probability of ionizing neutral Ar atoms by several orders of magnitude. This fact significantly increases the erosion of the target material and subsequently the rate of deposition onto the substrate, allowing to operate at lower voltages [111].

When insulating and/or ferromagnetic targets are used, as in the cases of MgO, SiO_2, and CoFe, it is necessary to power the sources by a RF generator. Indeed, the formation of a charged layer on the top of insulating target would reduce the erosion and hence the effectiveness of the sputtering process. The use of an RF power, where the sign of the target bias is varied at a high rate, can avoid this problem. In the latter case of CoFe, an RF bias is used, not because of charging problem (being a metal), but because its strong magnetization gives rise to a high stray field which makes the plasma ignition very diffcult [77]. When RF power is used, usually the minimum Ar pressure needed for igniting the plasma is higher than the deposition pressure, for this reason a *plasma-strike* with high Ar pressures is performed

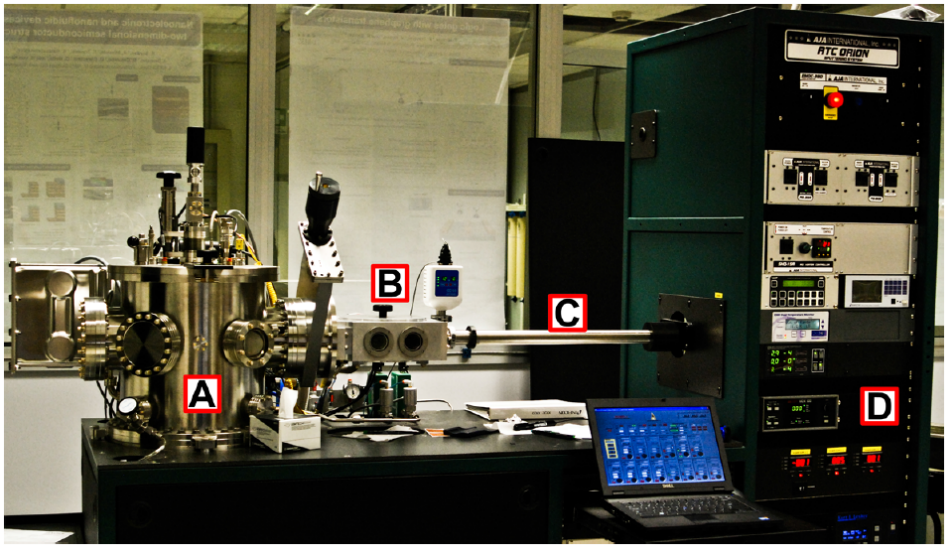

Figure 3.2: Our AJA ATC Orion sputtering system. A is the deposition chamber, B the load-lock, C the transfer arm, D the generators which power the sources located under the deposition chamber [60].

before the deposition.

During this thesis work, the *AJA ATC Orion Sputtering System* shown in figure 3.2 has been used. This system is provided with 10 magnetron sputtering facing-up sources positioned in the bottom of the chamber and pointing to a common focal point, where the substrate is located, thus permitting also co-evaporation. Pneumatic shutters positioned over the sputtering targets ensure a control of the deposited film with a precision up to about 0.1 nm. The facing down substrate is fixed on a sample-holder which is kept in rotation during the deposition to ensure the uniformity of the deposited film. Moreover the sample-holder can be moved in the vertical direction for optimizing the substrate-target distance. A permanent magnet ($H \sim 300Oe$) can be added to the sample-holder. Indeed, as it will be explained in chapter 5, most of the samples used for this work requires an uniaxial anisotropy direction, provided by the growth in this magnetic field.
The base pressure of the deposition chamber (A in figure 3.2) is around 10^{-9} Torr and is provided by a cryopump. Moreover an adiacent load-lock chamber (B in fig. 3.2), which is turbo-pumped down to 10^{-6} Torr, is used to quickly insert the sample without venting and contaminating the main

chamber.
The entire deposition process is controlled by a Labview software, which can control the Argon flux, the pressure, through the cryopump throttle valve, the pneumatic shutter, the gun voltage and the duration of the deposition. The deposition rates can be measured thanks to a quartz balance mounted in the vacuum chamber.

The availability of many parameters that control the sputter deposition makes it a complex process, but also allows large degree of control over the growth and microstructure of the film. The main parameters that influence the deposited films are briefly described below. These have been previously optimized by the NaBiS group.

1. Argon pressure: argon pressure should be preferentially kept low to avoid film contaminations. Moreover increasing the Argon pressure two competing phenomena take place: on one side the ionization probability and thus the deposition rate are enhanced, because of the larger number of Ar atoms, but, on the other, the eroded target material travelling towards the substrate experiences more scattering, preventing the material transfer.

2. Target power: depending on the voltage applied to the target, the collision energy of Ar ions impinging the target surface can vary. As a result, the target erosion rate and the energy of the eroded particles can be different, giving rise to different deposition rate.

3. Substrate Bias: applying a RF bias to the substrate causes a portion of the Ar^+ ions to bombard the substrate, thus enhancing the ad-atoms mobility and allowing a better rearrangement of the atoms on the surface. This mechanism is exploited prior to the deposition to perform a soft-etch cleaning of the substrate. However this can also cause a decrease of the deposition rate, because, due to the collisions with the Ar^+, part of the ad-atoms could desorb from the substrate.

4. Target to sample distance: it affects strongly the uniformity of the deposited materials, the energy and rate of deposition.

3.1.2 Optical Litography

Optical lithography is used for the microfabrication of electronic and spintronic devices exploiting the properties of a polymer, the photoresist, when it is exposed to UV light. Once the geometries of the devices have been designed, the patterns are transferred on the top of the substrate from a template, the *mask*.
After cleaning the sample from contaminations, the photoresist is spread over the sample and then the mask is placed upon it and irradiated with UV light, making only some areas of the photoresist soluble. At this point the development occurs in which an appropriate solvent removes the part of resist with higher solubility and leaves the rest unchanged.
High-speed centrifugal whirling of the samples is the standard method for applying photoresist coatings on the substrates. This technique, known as *"Spin Coating"*, produces a thin uniform layer of photoresist on the wafer surface. After the spin coating a *soft-baking* is performed. This consists in heating the wafer at about 100 °C for 1-2 minutes. In this step almost all of the solvents are removed from the photoresist coating. Soft-baking plays a very critical role in photo-imaging, because the photoresist becomes photosensitive, or imageable, only after this step. Oversoft-baking will degrade the photosensitivity of resist by either reducing the developer solubility or actually destroying a portion of the sensitizer, that is a basic component of resist which controls its photochemical reactions. Undersoft-baking, on the other hand, will prevent light from reaching the sensitizer.
There are two types of photoresist: positive and negative. In positive resist, exposure to the UV light changes its chemical structure so that it becomes more soluble in the developer. The exposed resist is then washed away by the developer solution. The mask, therefore, contains an exact copy of the pattern which is to remain on the wafer. Negative resists behave in an opposite way. Exposure to the UV light causes the negative resist to become polymerized, and more difficult to dissolve. Therefore, the negative resist remains on the surface wherever it is exposed, and the developer solution removes only the unexposed portions. Masks used for negative photoresists, therefore, contain the inverse of the pattern to be transferred. Figure 3.3 (a) shows the pattern differences generated from the use of positive and negative resist. During my thesis work the resists employed has been AZ5214E which is positive.

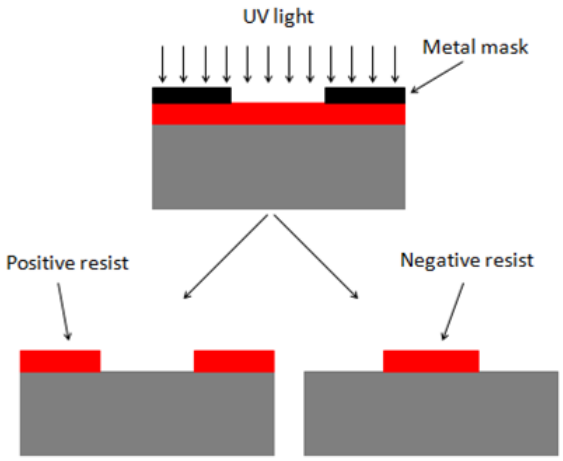

(a)

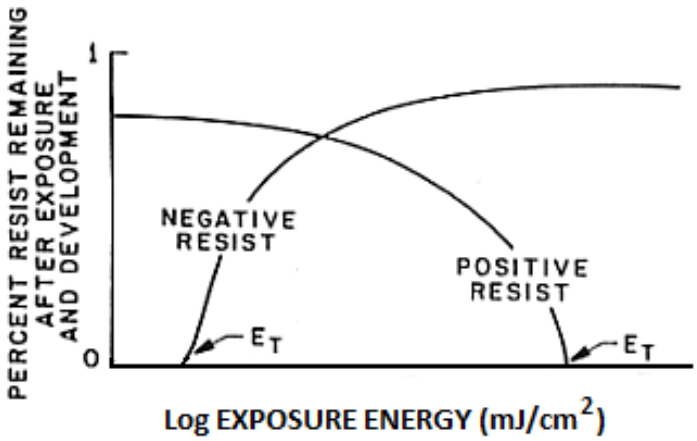

(b)

Figure 3.3: (a) Positive and negative resist after development. (b) Positive and negative resist exposure characteristics.

One of the most important steps in the photolithography process is mask alignment. A mask or *"photomask"* is a square quartz plate with a pattern of chriomium on one side, so that the metallized zones absorb the radiation, protecting the underlying resist from the exposure. The mask is aligned with the sample, so that the pattern can be transferred onto its surface. The mask-aligner used in this work is the Karl Suss MA56 (fig. 3.4), which allows to realize both the contact and proximity printing, using mask up to 5" and

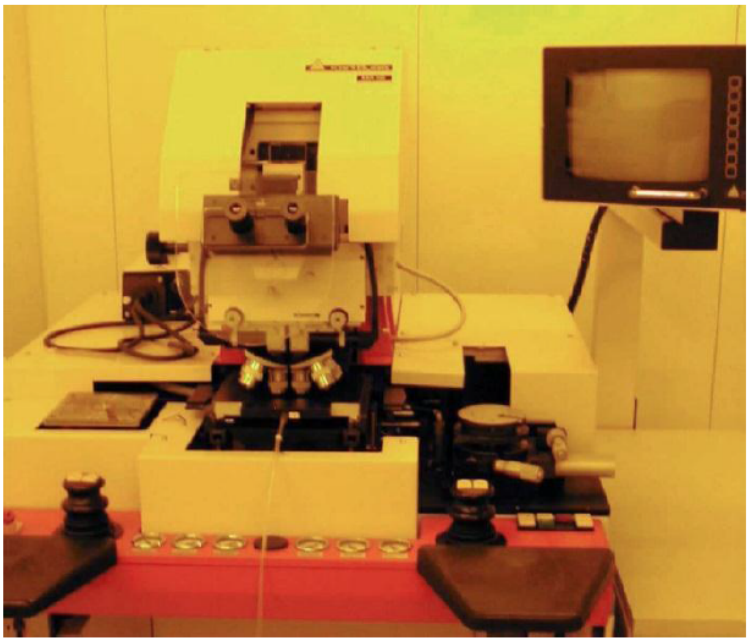

Figure 3.4: Mask aligner Karl Suss MA56.

wafer up to 4" in diameter. The UV radiation is obtained from the Hg I line (365 nm) of a mercury lamp with an intensity of about 13 mW/cm^2. In contact exposure, the resist-coated sample is brought into physical contact with the glass photomask. The wafer is held on a vacuum chuck, and the whole assembly rises until the wafer and mask contact each other. Because of the contact between the resist and mask, very high resolution is possible in contact printing (e.g. 1-micron features in 0.5 microns of positive resist with Karl Suss MA56). However, on the other hand, impurities trapped between the resist and the mask, can damage the mask and the photoresist causing defects in the pattern. The proximity exposure method is similar to contact printing except that a small gap, some tens of microns wide, is maintained between the wafer and the mask during exposure, minimizing the damages. Approximately 2 micron resolution is possible with proximity printing. During this thesis work the hard contact exposure mode is used: once the sample is in contact with the mask, the vacuum is removed and nitrogen is introduced under the sample, pressing it against the mask.

One of the last steps in the photolithographic process is development. Figure 3.3 (b) shows response curves for negative and positive resist after

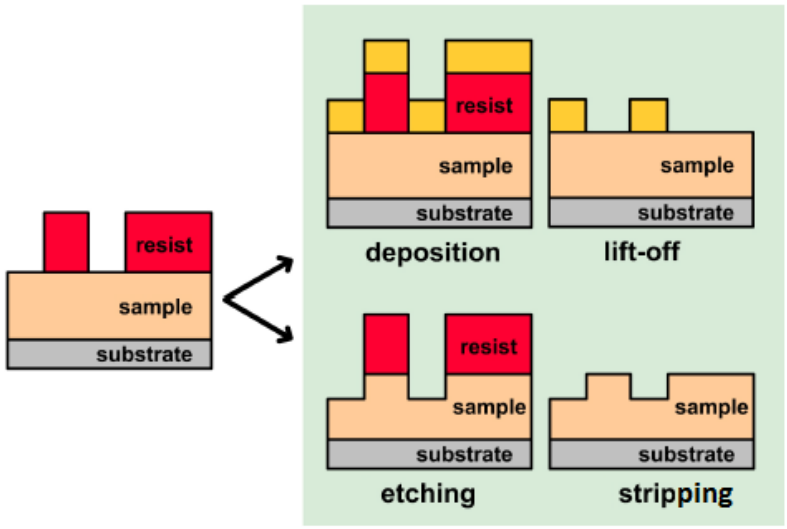

Figure 3.5: The two final phases of the photolithographic process.

exposure and development. At low-exposure energies, the negative resist remains completely soluble in the developer solution. As the exposure is increased above a threshold energy E_t, more of the resist film remains after development. At exposures two or three times the threshold energy, very little of the resist film is dissolved. For positive resists, the solubility in the developer is finite even at zero-exposure energy. The solubility gradually increases until, at some threshold, it becomes completely soluble.
After development, two other possible and opposite steps can follow and are depicted in figure 3.5. In the first case a deposition of addictional material can be performed, and the resist is then removed (using acetone or other suitable solutions) leaving the material deposited only in areas not covered by the resist (*lift-off*). In the second case an etching process can be performed, removing material from the sample thanks to ion bombardment or chemical etchants (dry etching (RIE, IBE) or wet etching (chemical)). At the end of the etching process, the residual resist, that protects the underlying material, is removed (*stripping*).

At variance with the process described so far, the inverse lithography (figure 3.6) uses an *inverted positive* resist, that, respect to the simple positive one, allows to facilitate the lift-off procedure. After the exposure (a), the

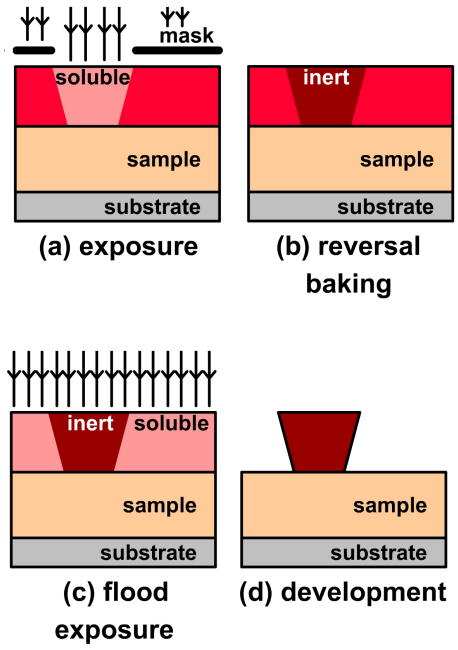

Figure 3.6: Inverse lithography process steps.

sample is baked so that a cross-linking of the polymeric chains in the exposed zones takes place. This makes the exposed area unsoluble and insensitive to further light exposure (b); after this, the sample is exposed without mask in the so-called *flood exposure* step (c). As a result, all the resist which was not exposed in the first step becomes soluble, whereas the rest, which experienced crosslinking, remains unsoluble (d). This procedure allows to obtain the inversion of the mask image and an undercut profile (walls inclined more than 90°). In this way the lift off procedure is facilitated because the solvent can filter up to the resist layer causing its detachment from the sample. This procedure will be used in the last step of lithography of magnetic tunneling junctions, as it will be described in paragraph 3.1.6.

3.1.3 Ion Beam Etching

IBE is a physical dry etching technique that faithfully reproduces the mask pattern on a substrate: the wafer is placed in a vacuum chamber ($\approx 10^{-7}$ Torr by a cryopump) and exposed to the ion beam, so that the impact of the ions erodes the sample abrading away the areas not covered by the photore-

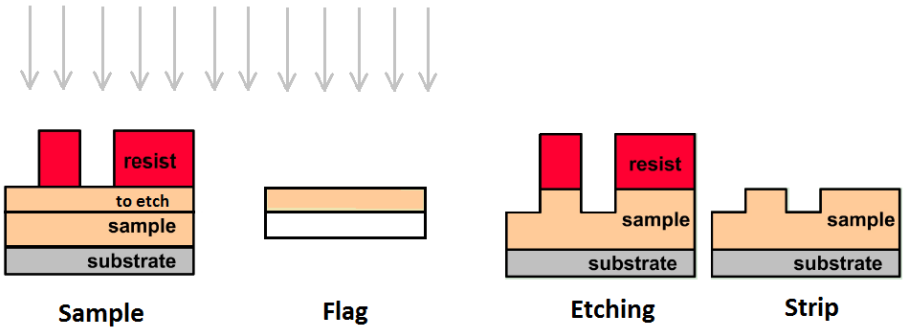

Figure 3.7: Visual method based on the use of flags for determining when to stop the etching.

sist (fig. 3.7). Due to the low precision and repeatability of the etching rates, above all with the high precision required by the MTJ fabrication process, a visual method using calibration samples is employed for determining when to stop the etching. Calibration sampels are exact replicas of the part of the sample to be etched, grown on a transparent substrate. These are mounted near to the sample on the sample-holder: when they become transparent it means that the corresponding part of the sample has been removed. In case of the process involved in this thesis, to compensate some variabilities which can be occurs with this method (due mainly to the different operators) an "overetch" is always performed (see paragraph 3.1.6).

In essence, three main parts of an ion beam etching can be distinguished: the discharge chamber, the grids and the neutraliser (fig. 3.8). Ion production is performed in the discharge chamber from inert Ar gas through a discharge current. Here the filament current, e.g. the cathode, emits electrons by thermoionic effect. The electrons, accelerated towards the anode by the voltage drop between the electrodes (discharge voltage), hit and ionize the Ar atoms giving rise to Ar^+ ions and free electrons. These electrons, which are also accelerated by the potential difference, contribute to mantain the plasma. Some of the Ar^+ ions are then accelerated toward the sample by a grid set at a negative potential (accelerator voltage). Thanks to the decoupling between the electrodes which generate the plasma and those which accelerate the plasma to the sample, it is possible to control indipendently the flux of Ar ions (increasing or decreasing ionization through the discharge voltage) and the energy of the accelerated ions (through the accelerator voltage of the grid). Between grid and sample a second filament produces electrons by ion-

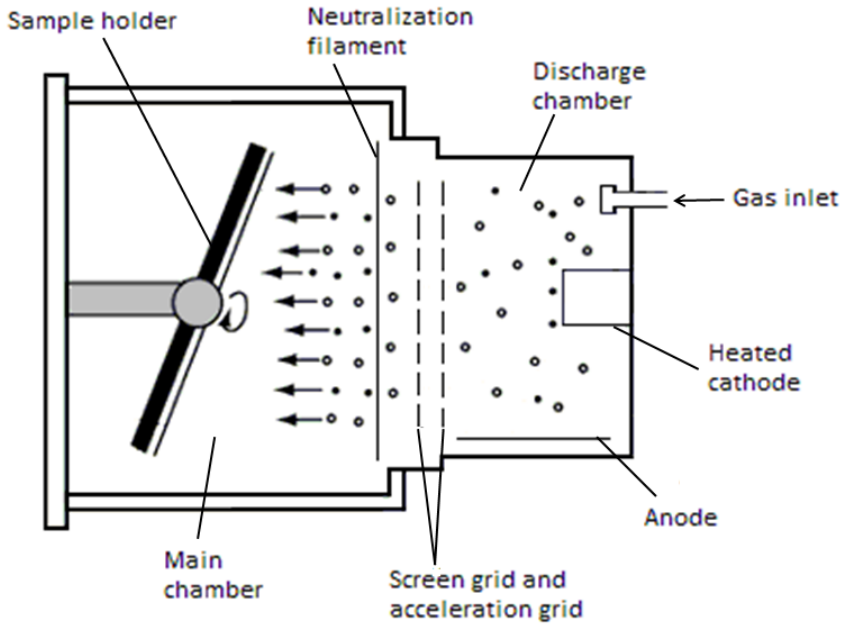

Figure 3.8: Schematic of the ion beam etching experimental apparatus.

izing Ar atoms (the Neutralizer). These electrons compensate the positive charges localized on the sample's surface, avoiding charging problems.

3.1.4 Electron beam evaporator

This process consists in electron beam heating a crucible containing the evaporation material above the melting temperature in a vacuum chamber. Evaporated atoms can move from the crucible to the substrate along an almost linear path, since atoms do not undergo collisions in vacuum. The deposition rate, once the target-substrate distance and the material are set, just depends on the electron beam power. The deposition rate, together with the film thickness, can be controlled by a rate monitor and a shutter.
An accurate replica of the mask pattern by the deposited film is contingent upon two conditions. First, the mean free path of the evaporant particles must be long compared with the target-substrate distance, to avoid random condensation caused by intermolecular collisions. Second, the sticking coefficient of the vapor must be close to unity to prevent reevaporation and lateral spreading.
During this thesis work all the samples grown and patterned with optolithog-

raphy have been provided with electrical contacts of chromium and gold, employing a Leybold "Heraeus L560" evaporator.

3.1.5 Field Annealing

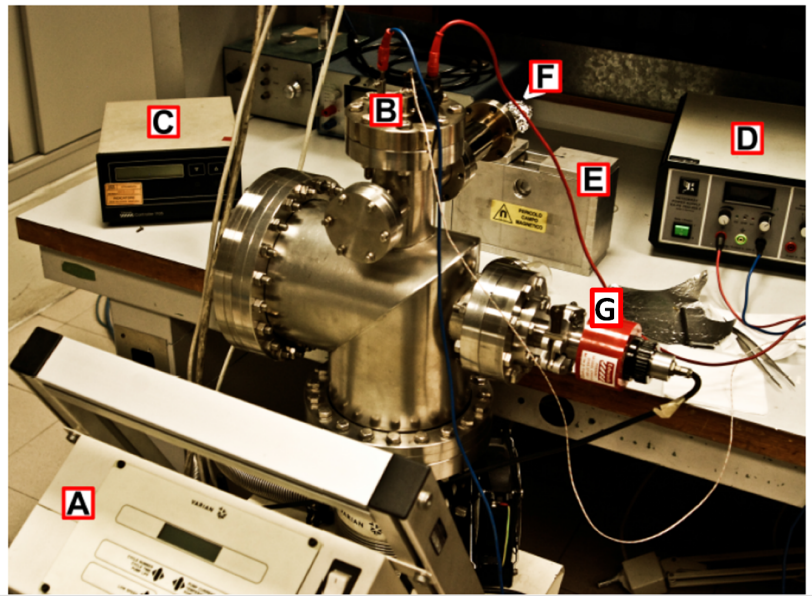

Figure 3.9: Our high vacuum magnetic field annealing system. A is the turbopump; in B, connection for the thermocouple (white wire) and the filament (blue and red wires); C is the vacuometer controller, D is the DC current generator, E is the permanent magnet; F is the sample holder; G is the vacuometer.

Magnetic field annealing is a well-established method for inducing a uniaxial anisotropy in amorphous ferromagnetic films. The high temperature allows atomic diffusion on a local scale, so that a preferred orientation minimises the energy of the system of atomic pairs and aligns them parallel with the applied magnetic field. This directional order is frozen in place as the sample is allowed to cool in the presence of the magnetic field, giving rise to an easy axis direction which is parallel to the applied field. As explained in section 2.1, the annealing procedure is necessary in MTJs for having high TMR ratios. Indeed it improves the crystallization of CoFeB (due to the presence of Boron, the deposited CoFeB layers are amorphous) and the quality of the MgO barrier, that are key factors for the TMR ratios. Moreover, the magnetic field cooling crossing the Néel temperature of the

antiferromagnet IrMn gives rise to the exchange bias.
The annealing parameters have to be carefully optimized. The annealing time should not be excessively prolonged and the temperature must be high enough to promote induced-anisotropy, but at the same time sufficiently low to avoid interdiffusion between the layers.
Figure 3.9 shows the high vacuum field annealing system. It consists of a chamber (pumped by a turbopump), terminating with a transparent bulb. In the bulb, the sample is located upon a thermically conductive support heated by a resistive filament through Joule effect. The filament current, provided by a DC generator, is modulated by a PID controller connected to a termocouple in thermical contact with the sample. The PID controller can be set for ramping from room temperature to a desired temperature (the top limit is about 500 °C) setting the final temperature, the temperature rising rate (°C/min), and the waiting time at the final temperature. At the end of the process the cooling down is not controlled and is mainly achieved by irradiation through the transparent bulb, because there is no convection (due to high vacuum) and the conduction through the sample-holder support is not significant. During the annealing process, the pressure is $p < 10^{-4}$ Torr in order to avoid sample contamination and to preserve the heating filament. The magnetic field is provided by a permanent magnet which generates an approximatively uniform field of magnitude $H \simeq 4$ kOe.

3.1.6 Process flow

In the previous paragraphs an overview of the fabrication techniques exploited in this work was performed. In the following the process flow to fabricate the MTJ sensors will be described.
The fabrication process consists of different steps:

- Substrate preparation
- Stack deposition by magnetron sputtering
- Patterning of rectangular junctions by optical lithography and contact deposition by electron beam evaporation
- Deposition of capping layer by magnetron sputtering

At the end of the manufacturing process each sample contains 6 chips with a total of 48 sensors of rectangular shape (see figure 3.10). The individual chip

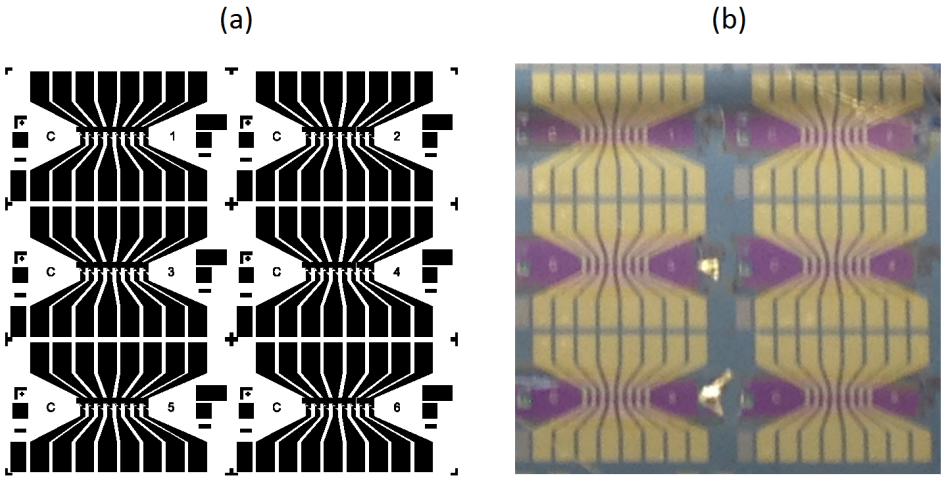

Figure 3.10: (a) Mask pattern and (b) picture of the final device after the fabrication process.

containing 8 sensors are then cut to be inserted in the microfluidic system for the experiment of molecular recognition that will be presented in chapter 6.

Substrate preparation

First of all the substrate is cleaned in acetone and isopropyl, and then cleaved with photoresist into 15x15mm^2 squares. The photoresist is removed with piranha solution, a solution of sulfuric acid (H_2SO_4) and hydrogen peroxide (H_2O_2), used in a 7:1 mixture, which further cleans organic residues off the substrate.

Sensor layout and sputtering parameters

The structure of the sensors developed is shown in figure 3.11. It consists of a multilayer stack grown on a Si/SiO_2 substrate by magnetron sputtering in the AJA ATC ORION sputtering system. During the stack deposition a magnetic field of $\sim 300Oe$ is applied to induce an exchange bias anisotropy. In table 3.1 all the sputtering parameters are listed for each layer.

Four kinds of stack have been tested, with different thicknesses of MgO (2nm, 1.23nm and 0.9nm) and of Co_{40} Fe_{40} and Co_{40} Fe_{40} B_{20} in the SAF structure (CoFe=2nm, CoFeB=3nm and CoFe=2.5nm, CoFeB=2.5nm). Before the deposition a soft etch of the substrate is performed in the vacuum

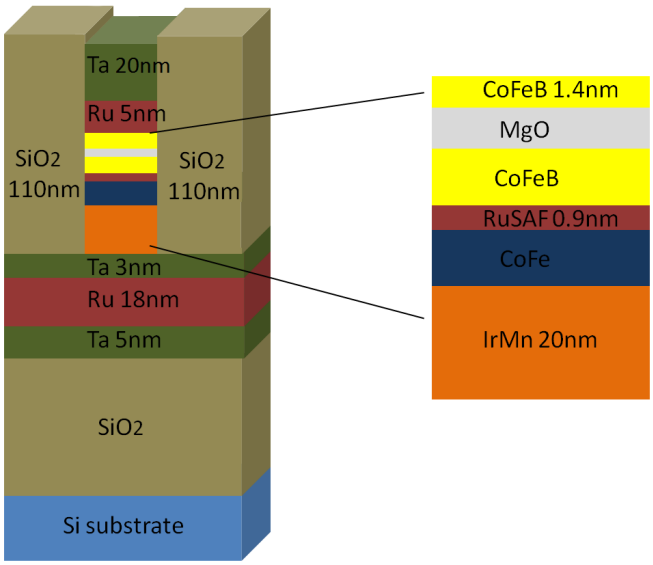

Figure 3.11: 3D view of the sputtered sensor stack after the lithographic patterning process.

Layer	Argon Pressure (mTorr)	Power target (W)	Dep. rate (Å/min)
Ta	3	100 DC	38.5
Ru	3	50 DC	21.5
IrMn	3	50 DC	16.08
CoFe	12	200 RF	19.5
CoFeB	3	58 DC	11.83
MgO	2	220 RF	1.58
SiO_2	2	200 RF	12.46
Al_2O_3	3	50 RF	4.84

Table 3.1: Magnetron sputtering parameters for each layer and the relative deposition rates.

chamber (10 minutes at 30W (RF mode), Argon pressure of 2mTorr) to etch the surface removing the residues arising from the cleavage and from the exposure to air.

Optical lithography process

After the growth, the stacks are patterned by optical lithography in order to define the sensors' shape and dimensions and to electrically insulate each sensor on the sample. In this paragraph the lithographic process employed for realizing the sensors is illustrated.
In order to test different cases, different patterns have been used. All these are compatible with the microfluidic system of figure 3.24 (c), used for the experiments of molecular recognition. All patterns give rectangular shaped sensors but with different junction areas of $2.5 \times 30\mu m^2$ and $2.5 \times 50\mu m^2$, and different bottom contact areas of $40 \times 150\mu m^2$ and $20 \times 150\mu m^2$. The shorter side of the rectangles is chosen parallel to the magnetic easy axis of the pinned bottom layer.
Sensors definition involves 3 lithographic steps which are the same for all patterns. All the parameters have been optimized in order to be able to define features with the right precision. The three steps of lithography are summarized in the following.

The first step consists in the electrical isolation of the single device through the definition of MESA (figure 3.12). First, the sample is cleaned with Acetone and Isopropanol. Then the photoresist is spin-coated on the sample and baked on a hot plate. Subsequently, the sample is exposed with the mask of figure 3.12 and developed. Then ion beam etching (IBE) defines the MESA in the sample, that during the process is tilted by 30° with respect to incident beam. The calibration sample, mounted in proximity to the sample, is an exact replica of the sample, so that, when it becomes transparent the sample will be etched until SiO_2. Finally the resist is stripped, and ultrasounds are used to remove residual resist. In table 3.2 the optimized parameters of this step are listed.

The second step is the most delicate step because the actual shape and dimensions of the sensors active area have to be defined with great precision. In this step the sensors' area is defined carving a pillar in the MESA (case a or b in figure 3.13). The sample is spin-coated with photoresist, baked, exposed with the mask of figure 3.13 and than developed. At this point the etching procedure takes place at different angles to sharply define the pillars: for 13' 30" at 30° and than for other 5'30" at 60° until IrMn, always waiting the calibration sample to become transparent. An "overetch" of 30" is than performed to compensate some variabilities.

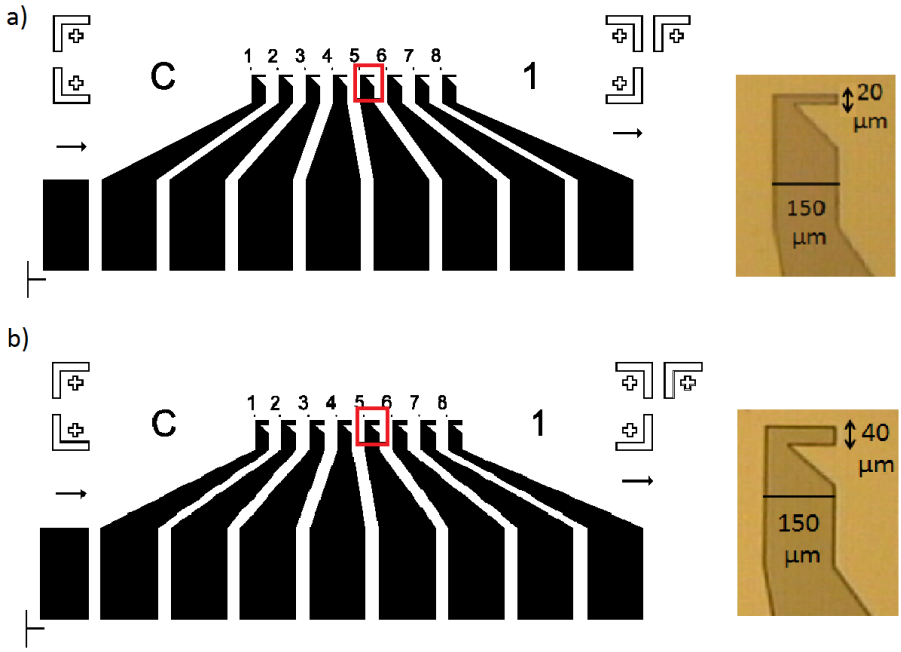

Figure 3.12: MESA definition. Bottom contact areas of a) $20 \times 150 \mu m^2$, b) $40 \times 150 \mu m^2$. On the right, zoom of the optical microscope images for the two pattern.

First Step	Parameters
Spin coating & baking	AZ5214E resist 1.4 μm thick, baked at T=110 °C, for 1'30"
Exposure	Exposure dose=128 mJ/cm^2
Development	35" in pure AZ726MIF
Etching	V_{dis}=200 V, V_{acc}=600 V
Stripping	AZ100 remover at T=100 °C

Table 3.2: Optimized parameters of the first step of lithography. V_{dis} and V_{acc} stand for respectively discharge voltage and acceleration voltage.

This part of the process, as already said, is very crucial because etching more or less can influence the sensor's functionality, altering its resistance and magnetic properties. Indeed, if the etching time is too short the risk is not to reach the MgO barrier and thus to have a shortcut between the top and bottom electrodes; on the other hand, if the ion milling is too prolongated, the risk is to carve the bottom layer too much thus resulting in high

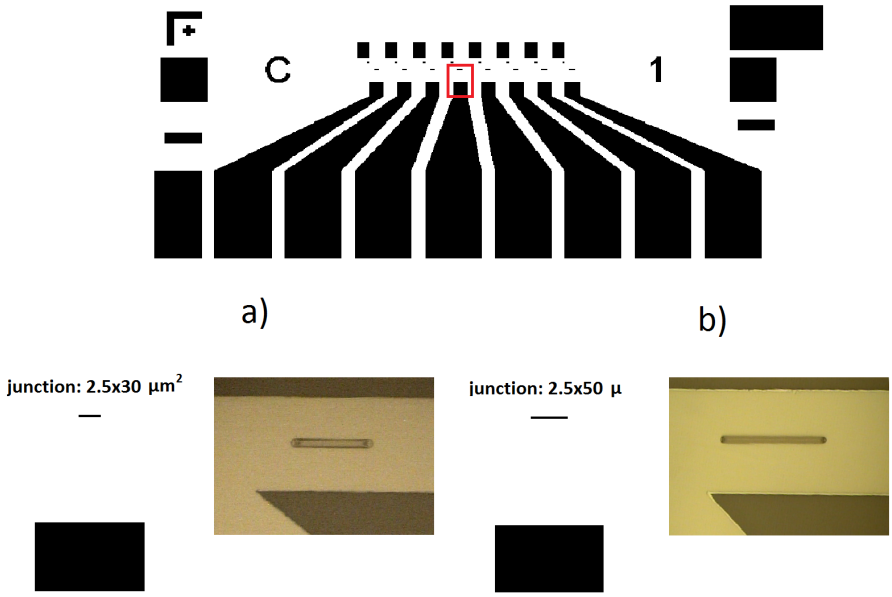

Figure 3.13: Second step of lithography: junction definition. The SiO_2 is deposited everywhere except for the junctions and the bottom contacts (black features in the pattern). In the lower panel, zoomed images of optical microscope of the junction area a) $2.5 \times 30 \mu m^2$, b) $2.5 \times 50 \mu m^2$.

Second Step	**Parameters**
Spin coating & baking	AZ5214E resist 1.4 μm thick, baked at T=110 °C, for 50"
Exposure	Exposure dose=128 mJ/cm^2
Development	40" in pure AZ726MIF
Etching	V_{dis}=200 V, V_{acc}=600 V
Lift off	AZ100 remover at T=100 °C

Table 3.3: Optimized parameters of the second step of lithography.

bottom resistance in series to the tunneling one.

A layer of 110 nm of SiO_2 is then deposited on the etched surface of the sample. The purpose is to insulate the bottom and top contacts and to cover the pillars edges to prevent further oxidation and edge effects. Finally, during the lift off the oxide layer deposited over the resist is removed leaving the junctions uncovered, in order to ensure ohmic contacts on the top and bottom electrodes. Even the lift off is a very delicate procedure, indeed

ultrasounds are not used for more than one minute a time, since the SiO_2 could be removed from the sample surface. In table 3.3 the optimized parameters of this step are listed.

In the third step the electrical contacts are defined (figure 3.14). The top pads are in ohmic contact with the top CoFeB electrode of the MTJ, while the bottom pads, deposited on the MESA, provide the contact with the bottom CoFeb electrode. This last contact is not ohmic, since it is made through the MgO barrier. However, since the contact area is bigger respect to the junction area, the MESA structure is likely to have a larger number of defects with respect to the MTJ, thus the current finds conductive channels which make the bottom contact resistance negligible with respect to the

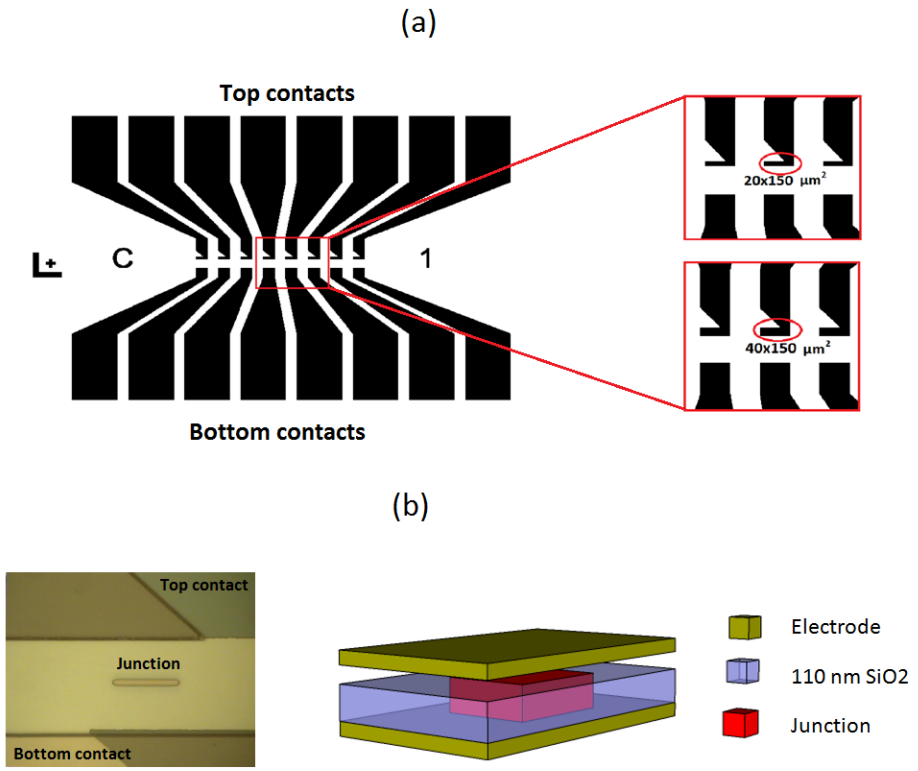

Figure 3.14: (a) Pattern of the third step of lithography. In the left panel the two kinds of contact areas are showed. (b) In the left panel a zoomed optical microscope image of the patterned structure before contacts deposition, and on the right a 3D view of the sensor.

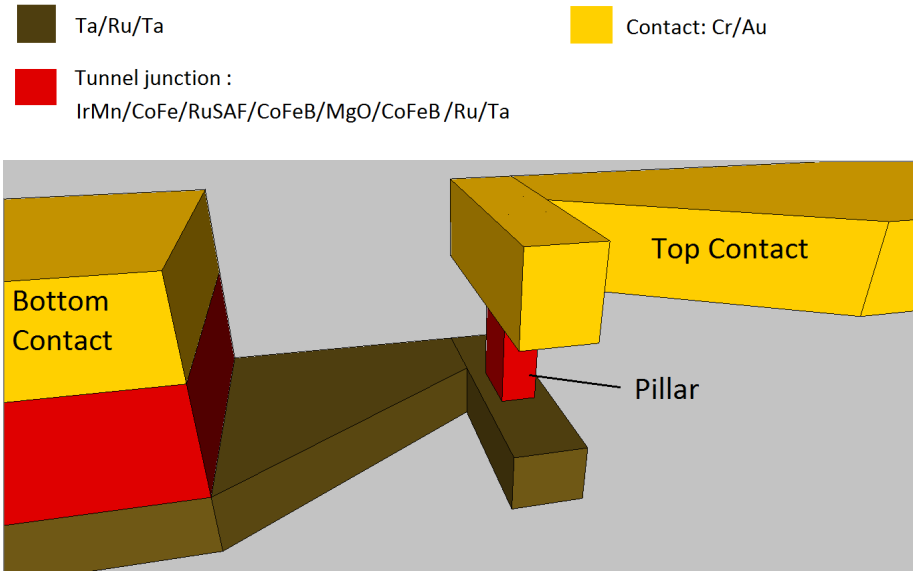

Figure 3.15: 3D view of one sensor after the lithographic process.

junction one (see figure 3.15).

Differently from the steps just described, in which the direct litography is used, this one is performed using inverse litography with the mask opaque upon the contacts and transparent elsewhere. Therefore the procedure in this case is different (it is summarized in table 3.4). First of all a thin layer of primer is cast on the sample for promoting the resist adhesion. Then the resist is spin coated on the sample, baked and then exposed with the mask of figure 3.14. At this point the reversal baking takes place to allow the cross-linking of the polymeric chains in the exposed zones. After this, the sample is exposed withouth mask for 30" and finally developed. In table 3.4 the optimized parameters of this step are listed.

Finally a bilayer of Cr(7nm)/Au(300nm) is deposited on the patterned sample by evaporation in a Leybold system. The chromium layer is used to promote adhesion of gold on the surface. In table 3.5 the parameters used in the evaporation process are listed for the two layers. At the end the resist is removed leaving only the patterned gold contacts. Even in this case ultrasounds are used with caution, since it can cause contacts detachment.

Third Step	Parameters
Prime spin & baking	2' at T=120 °C
Spin coating & baking	AZ5214E resist 1.4 μm thick, baked at T=110 °C for 1'30"
Exposure	Exposure dose=24 mJ/cm^2
Reversal baking	1'40" at T=117 °C
Flood exposure	30"
Development	20" in pure AZ726MIF
Lift-off	AZ100 remover at T=100 °C

Table 3.4: Optimized parameters of the third step of lithography.

Material	Base pressure (mTorr)	Rate (nm/s)	E-beam power
Chromium	2*10^{-6}	0.1	3%
Gold	2*10^{-6}	0.1-0.2	6%

Table 3.5: Parameters used in the evaporation process and relative deposition rate. The E-beam power is normalized to the full scale.

Capping

All the samples have been capped to prevent them from damages due to the fluids dispensed during the biological experiments (that will be secribed in chapter 6). The capping consists of the following multilayer: SiO_2(50nm)/ Al_2O_3(60nm)/SiO_2 (180nm), deposited by Magnetron Sputtering in RF mode from SiO_2 and Al_2O_3 targets (the growth parameters are summarized in table 3.1).

3.2 Sample characterization

3.2.1 Atomic Force Microscopy

Atomic force microscopy (AFM) is a very high-resolution scanning probe microscopy, with demonstrated resolution on the order of fractions of a nanometer. The AFM consists of a cantilever with a sharp tip (probe) at its end that is used to scan the specimen surface. The cantilever is typically made of silicon or silicon nitride, with a tip radius of curvature on the order of

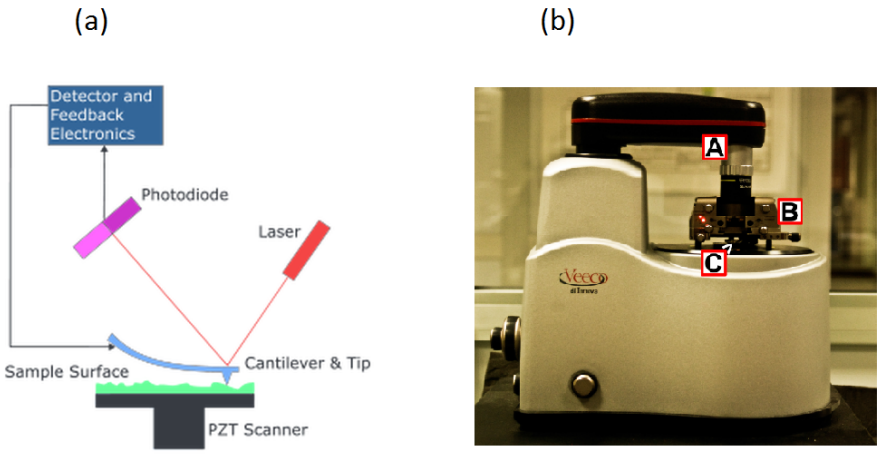

Figure 3.16: (a) Sketch of an AFM measuring process; (b) Our Veeco AFM system, where A is the optical camera for centering the desired sample zone and B is the core of the AFM, which includes the AFM tip, the laser and the partioned photodiode; C is the sample holder.

nanometers. When the tip is brought into proximity of a sample surface (few nanometers), forces between the tip and the sample lead to a deflection of the cantilever according to Hooke's law [19]. The deflection is measured using a laser spot reflected from the top surface of the cantilever into an array of photodiodes (fig. 3.16).

In most cases a feedback mechanism is employed to adjust the tip-to-sample distance to maintain a constant force between the tip and the sample. Traditionally, the sample is mounted on a piezoelectric system responsible for scanning in the x,y and z directions. The AFM can be operated in two different modes: static (also called contact) mode and dynamic (non-contact or "tapping") mode. In static mode, the cantilever is "dragged" across the surface of the sample in close contact with it and the contours of the surface are measured directly using the deflection of the cantilever. In the dynamic mode, the cantilever is externally oscillated at or close to its fundamental resonance frequency. The variation of the oscillation amplitude and phase with respect to the external reference oscillation provides information about the sample's characteristics.

At ambient conditions, most samples develop a liquid meniscus layer. Because of this, keeping the probe tip close enough to the sample, while pre-

venting the tip from sticking to the surface, presents a major problem for measurements. Dynamic contact mode, also called tapping mode overcomes this problem. All the AFM measurements have been performed during the thesis work in tapping mode, where the cantilever is driven to oscillate up and down near its resonance frequency and the amplitude of this oscillation typically ranges from 100 to 200 nm. A piezoelectric actuator is used to control the height of the cantilever above the sample. A tapping AFM image is therefore produced by imaging the force of the intermittent contacts of the tip with the sample surface. This method of "tapping", compared to the contact mode, reduces significantly the damage to the surface and the tip.

3.2.2 Vibrating Sample Magnetometer

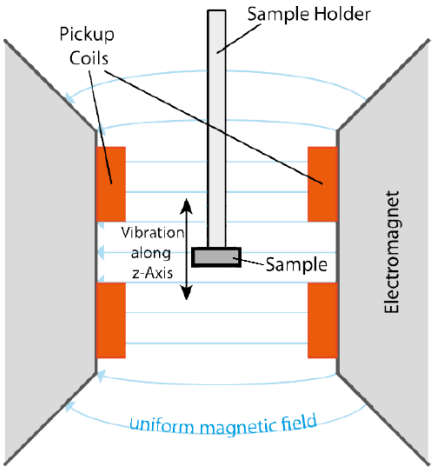

Figure 3.17: Tipical VSM measurement configuration. The facing down sample is put within a uniform magnetic field, generated by an elecromagnet, and a pair of pick-up coils. The sample is attached to a sample holder, that is connected to a mechanical system that makes the sample vibrate transversely.

Vibrating Sample Magnetometer (VSM) is a standard method of measuring hysteresis of thin magnetic films. The sample is placed as shown in figure 3.17, between two magnetic poles and a pair of pick-up coils. The sample holder is attached to a mechanical system, that makes the sample vibrate transversely, causing a change in the magnetic flux detected by the coils.

VSM operates on Faraday's Law of Induction, which tells us that a varying magnetic field will produce an electric field:

$$\nabla \times \mathbf{E} = -\frac{\partial \mathbf{B}}{\partial t} \tag{3.1}$$

The electromotive force generated in the pick-up coils is proportional to the magnetization of the sample, and depends on the orientation of the magnetic moment relative to the coils:

$$U = \oint \mathbf{E}\, dl = -\iint \frac{\partial \mathbf{B}}{\partial t}\, dS \tag{3.2}$$

To minimize the noise due to external sources of magnetic field, a pair of coils ares used: the variations of the external field add to the signal in one coil and subtract from the signal of the other coil. The induction current is amplified by a transimpedance amplifier and a lock-in amplifier. The various components are hooked up to a computer interface. Once properly calibrated, using controlling and monitoring software, the system can measure the absolute value of magnetic moment of the sample.
A typical measurement of a sample is taken in the following manner:

1. The sample begins to vibrate
2. The strength of the constant magnetic field is set through the controlling software
3. The signal received from the probe is averaged out of a fixed number of measurements and translated into a value for the magnetic moment of the sample
4. The strength of the constant magnetic field changes to a new value
5. The measurements are repeated and a plot of magnetization M versus magnetic field H is generated.

The VSM used in this thesis work is the *MicroSense Easy (EZ9) VSM*, shown in figure 3.18. This system allows to reach high magnetic field (up to 22 kOe) with still low field noise (5 mOe), and to measure the magnetic moment with very low noise (below 0.1 μemu at a usable sample space of 5 mm). The system is also equipped with a slide mounted cryostat/oven that allows quick cooling and heating of the sample from 77 K to 1000 K.

Figure 3.18: Vibrating sample magnetometer (MicroSense Easy (EZ9)). A is the system sketched in figure 3.17, B the mechanical system that makes the sample vibrate, including an anti-vibration component to minimize the vibration noise, and C the generators, amplifiers, and computer interface.

3.2.3 Magneto-Optic Kerr Effect

Magneto-Optic Kerr Effect (MOKE) technique consists in the analysis of the reflected light from a ferromagnetic sample, providing a powerful way for studying the magnetic behaviour of thin films. As depicted in figure 3.19, there are various kinds of MOKE configurations, depending on the relative direction of the magnetization to the plane of incidence of light. Depending on the direction of the magnetization whether it is perpendicular to the surface, parallel to the surface and in the plane of incidence, or parallel to the surface and perpendicular to the plane of incidence, it is called the polar Kerr effect, the longitudinal Kerr effect, and the transverse Kerr effect, respectively. During my thesis work only the longitudinal Kerr effect has been exploited.

MOKE measurement does not provide quantitative information about the magnetization vector, but gives an accurate picture of the hysteresis loops. Although MOKE is a surface-sensitive method, the probing depth is on the order of 10-20 nm thus, if the films are thin enough, one can obtain infor-

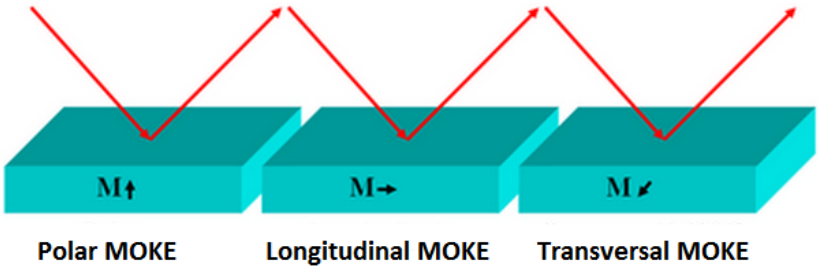

Figure 3.19: Schematic configurations of the sample magnetization for the polar, longitudinal, and transverse magneto-optical Kerr effects.

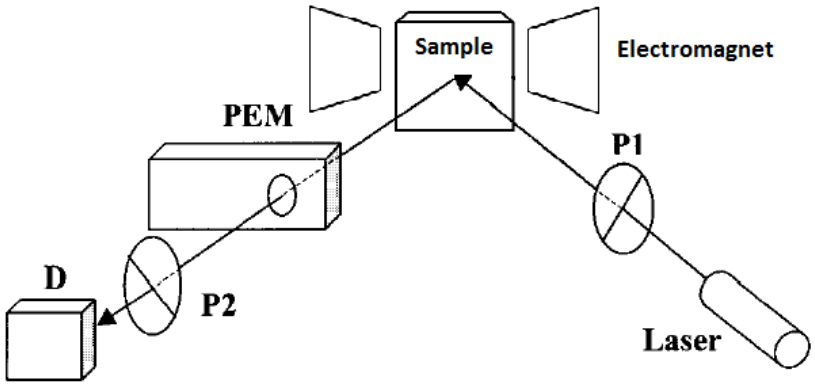

Figure 3.20: Sketch of our longitudinal MOKE experimental setup.

mation about the magnetization of the underlying layers.
In this paragraph I have mainly focused my attention on the instrumental apparatus used, while a detailed description of the Magneto-Optic Kerr Effect and of its possible configurations can be found elsewhere [124].

The measurement scheme of the standard MOKE configuration is reported in figure 3.20. The sample is located between the poles of an electromagnet which generates the external magnetizing field H. The electromagnet is powered by a KEPCO generator which can be controlled remotely by the PC. A laser diode generates a collimated light beam that is linearly polarized by a polarizer (P1 at 0° or 90° with respect to the optical plane, for p and s polarizations respectively) before it's reflected from the sample. After the reflection, it crosses a PhotoElastic Modulator (PEM) that introduces a con-

trolled oscillation of the phase between p and s components at a frequency f = 50 kHz. The MOKE measurements performed are tipically affected by an intense background, and by a weak signal due to the reduced thickness of the ferromagnetic material. For this reason a modulation-demodulation technique, allowed by the phase modulation introduced by PEM, results to be necessary.
After the PEM, a second polarizer (P2 at 45°) is placed as an analyzer before the beam reaches the photodiode (D), where the light is converted into a voltage signal which is subsequently demodulated by a lock-in amplifier. The demodulated voltage signal is proportional to the longitudinal component of the film magnetization (see You and Shin equations [124]). The signal is then digitalized by a DAQ and sent to the PC where the data are collected and analyzed in a Labview software.

3.2.4 TMR Measurements

The measurement of the TMR ratios of the sensors is directly connected to the study of the related curves R-H (resistance field curve or transfer curve). As shown in fact in paragraph 2.1.1 the magnetoresistance can be directly calculated from the transfer curve according to the relation:
TMR=(R_{ap}-R_p)/R_p,
where R_{ap} and R_p are respectively the electrical resistance in the anti-parallel and parallel states between free and pinned layers.
The transfer curve of a MTJ is obtained by applying a voltage drop across the system FM/I/FM while varying the magnetic field. To extract the magnetoresistive behavior of the sensors grown at LNESS, the instrumental apparatus in figure 3.21 has been used. The sample is located in the middle of an electromagnet whose current comes from a KEPCO bipolar generator controlled remotely by the PC. The electrical measurement is performed with a two-points probe. A microscope is placed just above the sample for the correct positioning of the tips on the gold contacts of the junctions (fig. 3.21 (c)).
A contact between the bottom and top electrode of the device is created imposing a fixed current to flow between them, and then the voltage drop is sensed for the different values of the applied field (switch from -400 Oe to 400 Oe). The current generation and the voltage sensing can be performed by the same instruments, Keythley 2601 source meter, or by two different

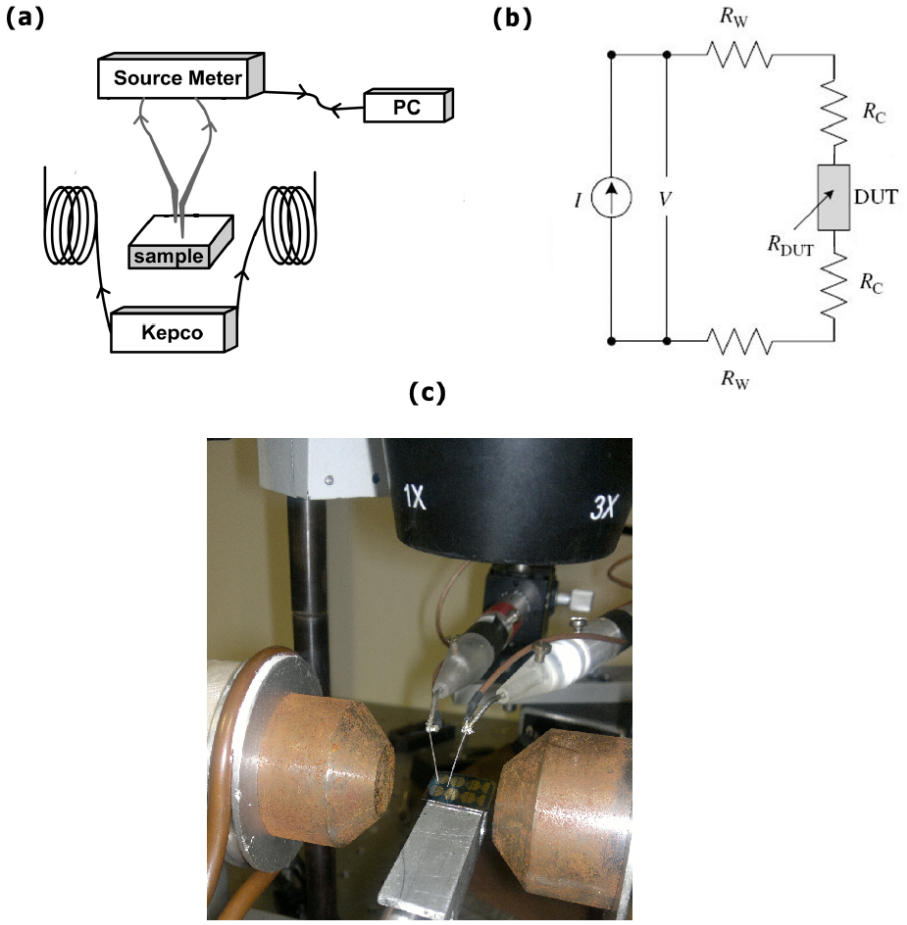

Figure 3.21: (a) Sketch of a two point-system for TMR mesurements; (b) Two-points probe; (c) Photo of the sample placed between the poles of the electromagnet during the two-points measurement.

Keythleys. The data are then analyzed by a Labview software which automatically plots the R(H) curve calculating the TMR ratio.
In figure 3.21 (b) the resistance scheme involved in the measurement is reported. From this sketch it is clear that measuring the device resistance R_{DUT} with the right precision, implies that R_{DUT} is bigger than R_W, that is the resistance of the wire of the connections, and than R_C, that is the contact resistance. Indeed the total resistance of the system is $R_{tot} = 2R_W + 2R_C + R_{DUT}$, and the presence of these parasitic terms, since they do not

vary with the magnetic field, causes an underestimation of the TMR ratio:

$$TMR = \frac{R_{ap} - R_p}{R_p + R_{par}}, \tag{3.3}$$

where R_{par}=2R$_W$ + 2R$_C$.
From previous measurements in different configuration it is known that the top contact is less than 10 Ω, the bottom is about 50-70 Ω, and the probes and wires are about 5 Ω, resulting in a parasitic resistance R$_{par}$ ≈ 85 Ω. Considering a junction resistance of about 1 kΩ, the underestimation will be small, of the order of 8%.
It is worth to notice that this probe configuration is dictated by the number of lithographed contacts in our devices (see paragraph 3.1.6), which does not allow to perform a more accurate four-point probe measure, but has the advantage to greatly simplify the biological experiments during which all the bottom contacts are connected together to ground.

3.2.5 Noise Measurements

During this thesis work different sensors have been tested to extract their noise spectrum (see section 5.3). The noise measurements have been performed using a spectrum analyzer based on the cross-correlation technique between two different acquisition channels. This technique reduces the effect of the instrumental noise, thus obtaining a higher sensitivity than a traditional single channel spectrum analyzer. The cross-correlation technique consists of two different measures of the same signal by two identical and independent acquisition channels; in both of them, both the useful signal and the unwanted noise inevitably introduced by the channel itself, will be present. Because the noise in one channel is uncorrelated with the noise in the other one, mathematical cross-correlation operation on two channels returns only the useful signal and reduces (ideally eliminates with an infinite measurement time) the uncorrelated noise [31], [95].
In this scheme each channel consists of a low-noise preamplifier and a band-pass filter that selects the frequency of interest for the spectrum measure.
In the case of noise measurements, a digital spectrum analyzer has been used, in which the frequency selector is replaced by an ADC converter followed by a Discrete Fourier Transform (DFT) operation which works as a bank of narrowband filters and allows to measure over N frequencies in parallel (where

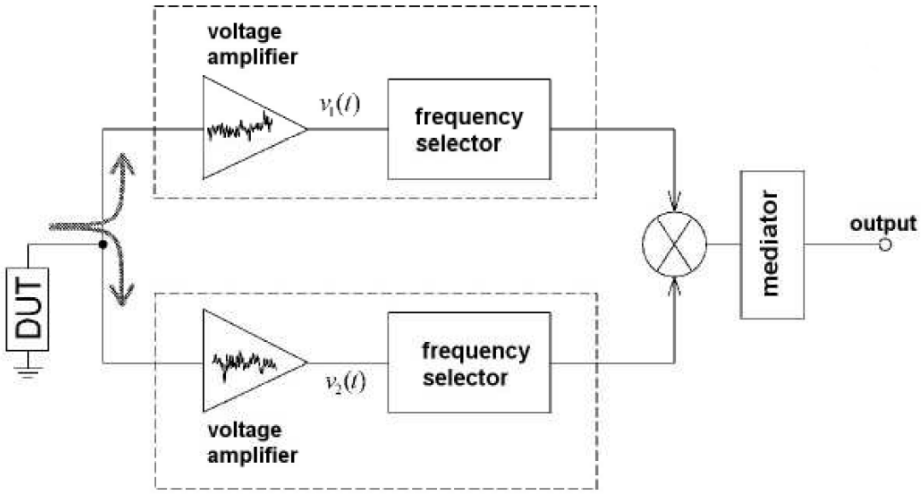

Figure 3.22: Working principle of a cross-correlation spectrum analyzer.

N is the number of acquired samples).
To performe the noise measurements, the sensor has been biased with a DC current, and the noise spectrum is measured sampling at 25 Mhz (the measurement lasts few minutes). To obtain a more resolved spectrum at low frequencies, a low pass filter (pole frequency=1 kHz) and a lower sampling frequency of 250 kHz can be used.

3.3 Biological experiments

3.3.1 Instrumental apparatus

During the experiments of beads detection and molecular recognition described in chapter 6, the beads signal has been acquired through a double modulation technique in order to improve the sensor sensitivity and minimize the 1/f noise [47]. In this section the instrumental apparatus used and the method of double modulation will be described, while all the phases of the experiments will be reported in detail in chapter 6. In figure 3.23 (a) a sketch of the instrumental apparatus used for the experiments is shown. The samples used for these experiments consist in a rectangular chip containing 8 sensors of rectangular shape, as described in paragraph 3.1.6 (figure 3.24 (a)). The chip is inserted in the microfluidic cell sketched in figure 3.24 (c). This consists in a click-on cell comprising a Polycarbonate (PC) chip

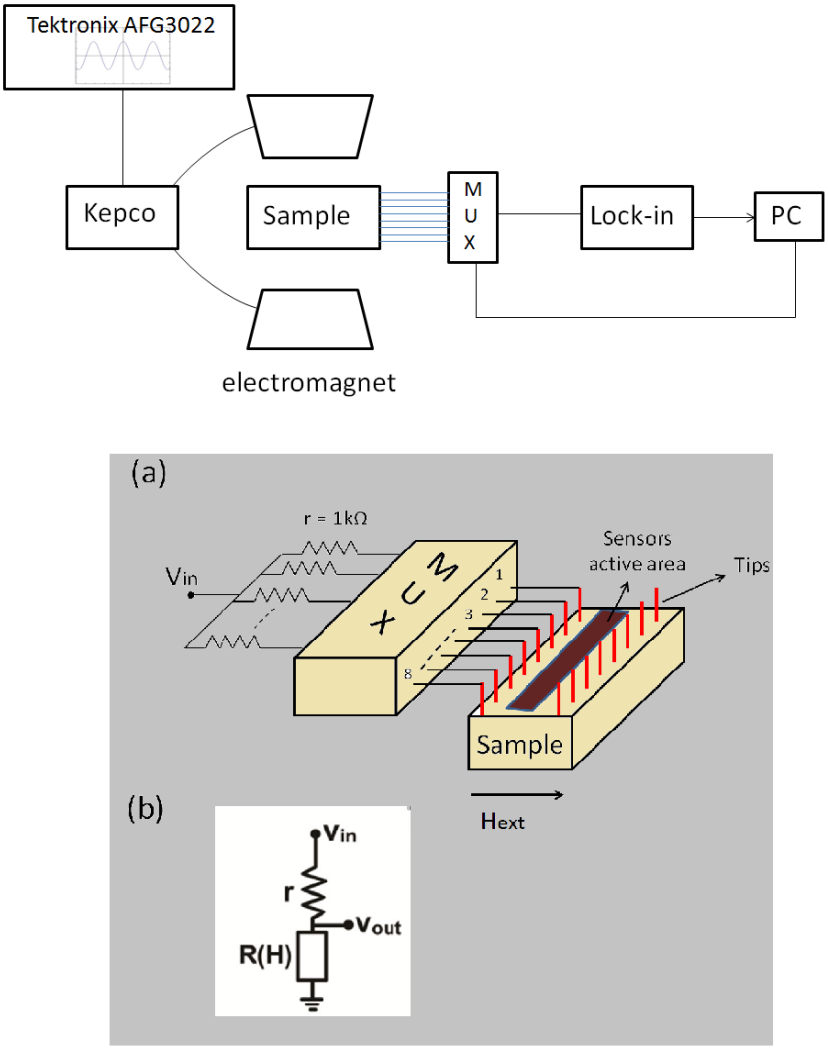

Figure 3.23: Circuit diagram of the instrumental apparatus used for the experiments of detection beads with a double modulation technique. In the inset (a) the multiplexer and series resistances of 1kΩ and (b) Vin and Vout with only one enable sensor.

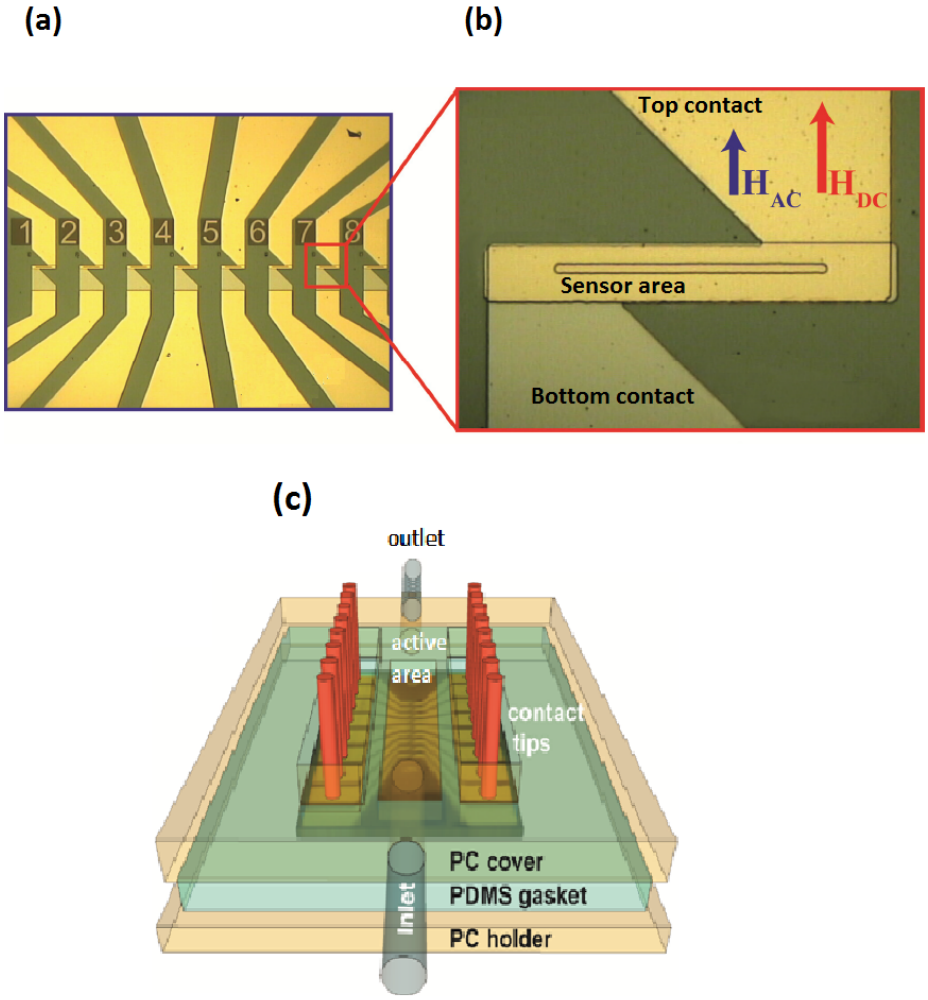

Figure 3.24: (a) Optical microscope image of the chip containing 8 sensors and (b) zoom image of one sensor with the directions of the two components of the magnetic field; (c) sketch of the microfluidic system with also the electrical contact to the array of eight sensors.

holder, on top of which a 12 mm^3 microfluidic chamber is defined by a Polydimethylsiloxane (PDMS) gasket, and a PC cover. The active area of the sensors is located in the central region, in which the liquid containing the beads will pass, with a controlled speed, through the thin tubes of inlet and outlet. Metallic tips will contact the bottom and top electrodes of each sensor from the top, outside the microfluidic cell. A multiplexing system is used to address the eight different sensors in such a way that, for stability purpose, the current permanently flows throughout all the junctions and the readout occurred sequentially. The multiplexer is enabled from the PC via a Labview software which also performs the ouput signal visualization and the data saving. The output voltage is monitored during all the phases of the experiments, from the beads injection and sedimentation until the beads wash out and the consequent signals change (see chapter 6). The important parameter to study is the signal variation ΔS due to the stray field produced by the beads on the sensors, that should be the largest possible.
The voltage V_{in}, applied to the sensor and the series of a fixed resistance (r = 1kΩ, fig. 3.23 (b) and (c)), is modulated at a frequency $f_1 = 1.101$ kHz. The sample is located in the middle of an electromagnet whose current comes from a KEPCO bipolar generator controlled by a function generator (Tektronix AFG3022). The magnetic field H_{ext}, applied parallel to the shorter side of the junctions, is the sum of two contributions: a bias field H_{DC} to bias the sensor [3] and a small oscillating field H_{AC} at $f_2 = 39$ Hz to excite the magnetic beads (fig. 3.24 (b)) [32]. Thanks to this double modulation, the response to oscillating magnetic field, depending on the concentration of beads above the sensor, appears in the output voltage as a component at the frequency ($f_1 \pm f_2$), which can be easily extracted via a lock-in amplifier (HF2LI, ZI).

3.3.2 Methods

A commonly used figure of merit of magnetoresistive sensors, employed to detect magnetic beads labelling biomolecules in lab-on-chip applications, is the sensor sensitivity (S_{sensor}) to external magnetic fields in the linear region of the transfer curve. It has been shown [3] that, in case of lock-in detection and beads excitation by a small AC magnetic field, S_{sensor} is not the good figure of merit to optimize. Indeed, the highest sensitivity to the magnetic beads is achieved biasing the sensor in the region of its characteristics where

the product between the DC bias field and the second derivative of the resistance with respect to the magnetic field is maximum. In practice, the sensors under test are not used in the linear regime, where S_{sensor} is maximum, but with an external bias magnetic field, shifting the operation point in the non-linear zone of the R(H) curve, where S_{sensor} is sizeably smaller [32].
A general criterion for correctly choosing the bias field is given by the phenomenological model of bead detection now described [3]. If the amplitude of the oscillating field H_{AC} used for exciting the beads, that will be called h from now on, is small compared with the width of the linear regime of the R(H) characteristic, it can be considered as a perturbation superposed to the DC bias field. Without beads above the sensor R(H) can be written as:

$$R(H_{DC} + H_{AC}) \approx R(H_{DC}) + \left.\frac{dR}{dH}\right|_{H_{DC}} \cdot h \cdot \cos(2\pi f_2 t). \tag{3.4}$$

When the beads pass over the sensor's surface a DC and AC stray fields are produced, and can be written as: $H_{bDC} = \alpha_{DC} \cdot H_{DC}$ and $H_{bAC} = \alpha_{AC} \cdot H_{AC}$. The coefficient α igives the linear bead response and can be written as $\alpha = \beta\chi V_b n$ [28], [48], where β is a geometrical factor that depends on the beads side and distribution over the sensor area, χ is the magnetic susceptibility of the beads, V_b their volume and n is the number of beads per unit volume. The stray field produced by the beads adds to the external fields leading to a variation in resistance:

$$\begin{aligned} R(H_{DC} + H_{AC}) \approx R(H_{DC} \cdot (1 + \alpha_{DC})) + \\ + \left.\frac{dR}{dH}\right|_{(1+\alpha_{DC})} \cdot h \cdot (1 + \alpha_{AC}) \cdot \cos(2\pi f_2 t). \end{aligned} \tag{3.5}$$

Considering the potential divider of figure 3.23 (b), the approximation $|\alpha_{DC}| \ll 1$, and that the normalized signal $S_v = \frac{V_{out}}{V_{in}}$ is demodulated by the lock-in at a frequency $f_1 + f_2$, the net signal ΔS, can be calculated:

$$\begin{aligned} \Delta S = S_v|_{Beads} - S_v = \\ = \frac{1}{2}\frac{r}{(r + R(H_{DC}))^2} \cdot h \cdot \alpha_{AC} \cdot \left(\left.\frac{dR}{dH}\right|_{H_{DC}} + \left.\frac{d^2R}{dH^2}\right|_{H_{DC}} H_{DC} \right). \end{aligned} \tag{3.6}$$

For more detailed calculations see the article [3].

The presence of the latter term in the equation 3.6 explains why the

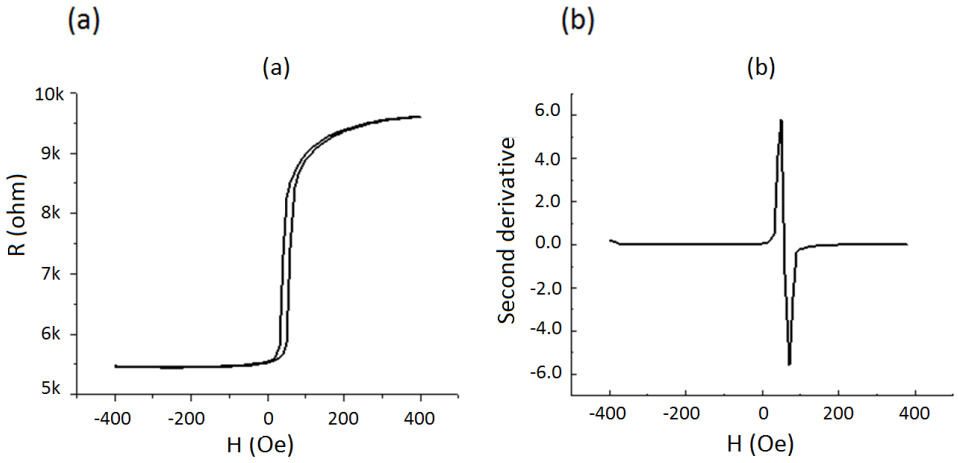

Figure 3.25: Transfer curve R(H) of a TMR sensor grown at LNESS (MgO thickness = 1.23nm) (a) and second derivative of the forward half-loop (b).

highest sensitivity to the magnetic beads is achieved biasing the sensor in the region of its characteristics where the product between the DC bias field and the second derivative of the resistance, with respect to the magnetic field, is maximum. Indeed in figure 3.25 it is possible to observe the second derivative of a typical trasfer curves of a TMR sensor (grown at LNESS) that shows how this can reverse its sign at a certain magnetic field. For a critical intermediate field, a perfect compensation of the two terms in the bracket of eq. 3.6, containing the first and second derivative, could take place, eventually leading to a net signal $\Delta S = 0$. For this reason S_{sensor} alone is not the good figure of merit to optimize and the sensor under test can not be used in the linear regime, where S_{sensor} is maximum.
Therefore, after the above considerations, the rigorous approach for choosing the best working point of the sensor is to measure its resistance R(H), by sweeping the magnetic field in DC, and selecting the optimum bias field H_{DC} in such a way that equation 3.6 results to be maximized. In practice, a less rigorous approach is used. This method consists in an empirical calibration of the sensor:

- First the bias voltage V_{in} (at frequency $f_1 = 1.101$ kHz) is applied, and the device voltage is measured
- Then the small oscillating field H_{AC} at $f_2 = 39$ Hz is turned on

- The output signal at $f_1 + f_2$ is collected sweeping the magnetic field in DC
- The optimum value of H_{DC} is chosen where the output signal, at $f_1 + f_2$, is 2/3 of the maximum.

Once identified the optimum H_{DC}, the magnetic field is set starting from saturation, in order to initialize the sensor in its state of low/high resistance and choose the proper branch of the TMR if some hysteresis is present.
As explained before, the sample consists of a chip containing 8 junctions of rectangular shape (see figure 3.24 (a)). Despite the repeatability of the manufacturing process, even if the 8 sensors presents very similar characteristic, slight differences in the switching fields or disuniformities in the applied magnetic field can result in different values of the optimum field H_{DC}. Practically, the choise of the optimal working point is performed following the above-mentioned procedure, by studying one sensor at a time, selecting it through the multiplexer. Then, for each sensor the optimum H_{DC} is found, and finally a compromise between these different values is found. This procedure also allows to verify the operation of each sensor, in such a way that only the working ones are enabled for the experiment.

A remarkable aspect to be considered is that this criterion for the choice of the best operating conditions of the sensors allows to maximize the signal to noise ratio. Indeed the highest level of noise N is found in the linear region of the sensor, while it decreases approaching the magnetic saturation of the free electrode, where magnetic fluctuations are suppressed. This implies that the signal to noise ratio, defined as the ratio $|\Delta S|/N$, results to be maximized with this choise of operating conditions.

Chapter 4

Platform layout

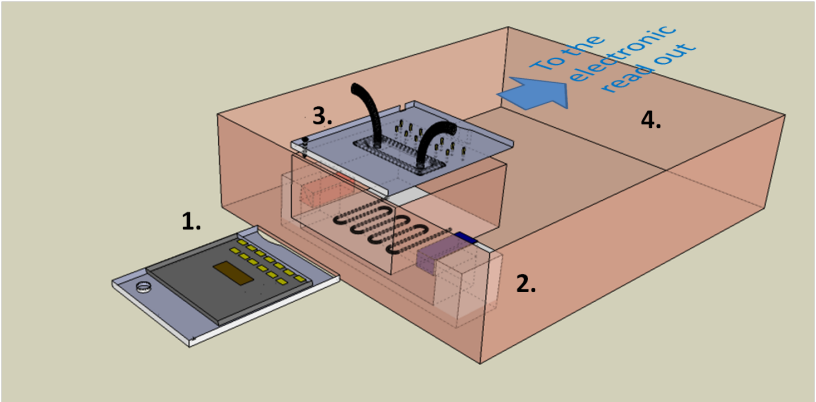

Figure 4.1: Layout of the platform for magnetic biosensing including the microchip, electromagnet, microfluidics and front-end electronics.

As explained in the introduction this thesis work is part of a project aimed at the development of an on-chip magnetic-based platform for the diagnostic of two kinds of pathogen DNA, hepatitis E and salomella/listeria virus.
The prototype of the diagnostic tool, to be developed, is shown in figure 4.1. It basically consists in a handeld device in which four main different parts can be distinguished:

1. Microchip with 12 sensors
2. Electromagnet
3. Top cover: microfluidics and electrical contacts (click on system)

4. Front end electronics for read-out

Each part of the platform has been properly designed in order to ensure small dimensions and portability, and the interface to a computer or smartphone will permit point-of-care testing. All the functionalities required for the assay will be integrated in the platform, apart from the PCR which will be performed in a dedicated modulus and the pumping system (through syringe pumps) which will be external in the first release fo the system. The experiment control will be carried out via software, except for the mounting of the chip and the fluids injection, which will be performed by the user.
The biological experiment will be divided into different phases, that are described below.

Phase 1: Bio-functionalization of the sensors

In the chemical laboratory the chip with the sensors will be functionalized only in correspondence of the active sensors area, in order to achieve higher sensitivity and quantification capabilities [4]. The procedure for the selective bio-functionalization of the sensors' surface consists in the following steps (see figure 4.2):

- A pattern is created in correspondence of the sensors' surface employing standard optical lithography.
- The chip is coated with a functional copolymer which provides reactive groups suitable for immobilization of the oligonucleotide probe molecules and, at the same time, prevents non-specific adsorption of biological fluids components [92] [106].
- The entire sensor area is then massively spotted with single strands DNA probes, employing a Sci-Flexarrayer S5 by Scienion spotter machine with an 80 μm noozle.
- After binding the probe overnight in the humid chamber (temperature $\approx 22\,^{\circ}\mathrm{C}$, humidity 50%) the photoresist is stripped in aceton.
- After the lift-off procedure, probe biomolecules are immobilized only in corrispondence of the patterned regions, which correspond to the the sensors area.

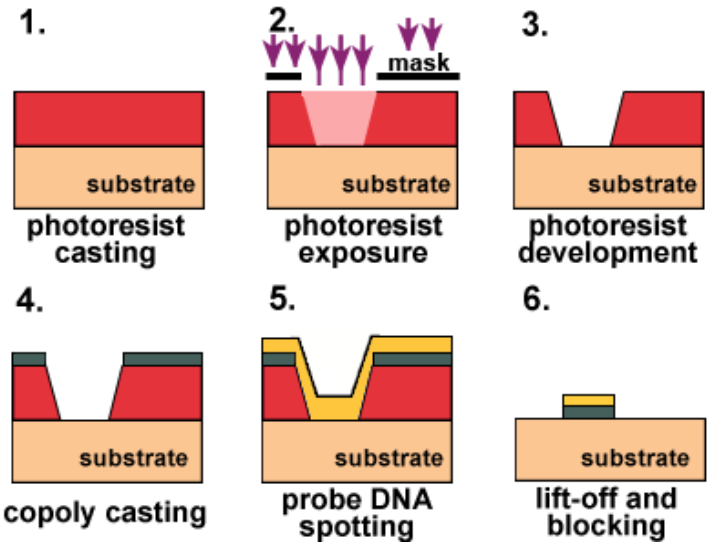

Figure 4.2: Sketch of the optolithographic process for the selective biofunctionalization.

- The surface is blocked with suitable polymers coatings which preclude unspecific binding of biomolecules during the following DNA hybridization phase.

Phase 2: Preparation of the field test (by a food and agricultural industry)

Two main steps are involved in this phase:

1. Sample preparation: the target biological material is extracted by commercial DNA extraction kits, then amplified by means of PCR, and marked by nano-magnetic beads (pre-hybridization approach).

2. Chip assembly: the microchip is inserted inside the microfluidic system, between the poles of the electromagnet, and the calibration of all the sensors is performed. This step has two goals: first of all to identify and exclude the eventually damaged sensors and secondly to identify the proper working point of the device (see section 3.3). After these tests, the parameters of the assays are set: temperature (about 50 °C), magnetic field (AC+DC) and sensors bias current (AC). Once all this parameters are stabilized and the sensors output, acquired through the

double modulation technique (see section 3.3), is constant in time, one can start with the experiment.

Phase 3: DNA hybridization

The target DNA is injected in the microfluidic cell and brought into contact with the active area of the sensors, previously functionalized with the probe DNA. Hybridation between complementary probes and target happens, and the sensors detect the presence of the magnetic labels via a change in resistance, that reflects on a variation in the output signal demodulated by a lock-in and real-time visualized by a computer/smartphone.

Phase 4: Washing

This is the most critical part of the experiment, as will be outlined in chapter 6. The unbound target biomolecules are washed away until the control sensors recover their initial baseline, and residual sensor signals are evidence of those sites in which complementary target and probe have successfully interacted.

As already mentioned, this project involves the collaboration of several research institutes and companies operating in biomedical and agrifood sectors. In particular, ICRM (Chemistry Institute of Molecular Recognition) and Dia.Pro (Diagnostic Bioprobes srl), deal with the realization and immobilization of the probes, and with the labeling of the target DNA. The department of Electronics and Information of Politecnico di Milano, instead, deals with the realization of the front-end electronics for the signal reading. In this context my work, together with my research group, has focused on the sensory part of the platform, from the definition of the architecture of the microchip, to manufacturing, characterization and optimization of different sensors to test for the first molecular recognition experiments.
In the next sections an overview of the various components of the platform is presented, with particular attention to the microchip and the design of the mask for optical lithography.

4.1 Sample holder and microchip

The microchip of figure 4.3 consists of a silicon wafer of about $15 \times 15 mm^2$ in which a matrix of 12 sensors based on magnetic tunnel junctions is defined for the simultaneous detection of the two different sequences of nucleic acids. The various sensors are organized in this way:

- Three sensors are used for molecular recognition of the first DNA sequence mode (hepatitis E)
- Three sensors are used for the second sequence (salmonella and/or listeria)
- Three sensors are made available for the controls necessary to identify false positives
- One sensor is used for the microchip's temperature control
- The remaining two sensors are duplicates for safety.

Sensors definition involves 3 lithographic processes after the sputtering deposition of the sensors' stack (see figure 3.11 in paragraph 3.1.6). Each sensor has a rectangular shape and is provided with one top contact and one common bottom contact.

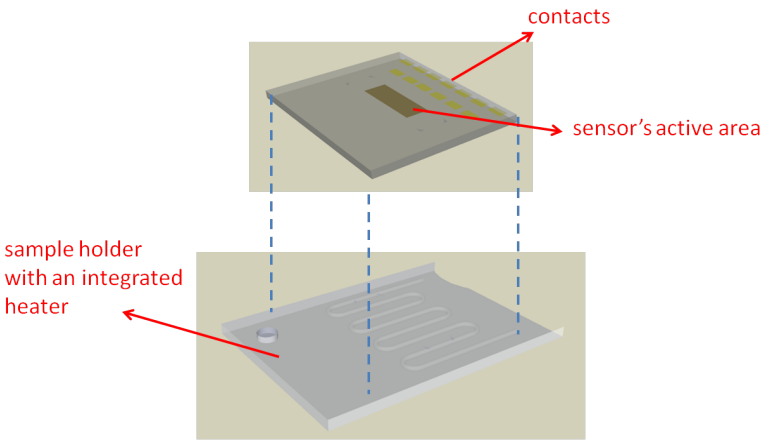

Figure 4.3: View of the microchip and of the sample holder with the integrated heater.

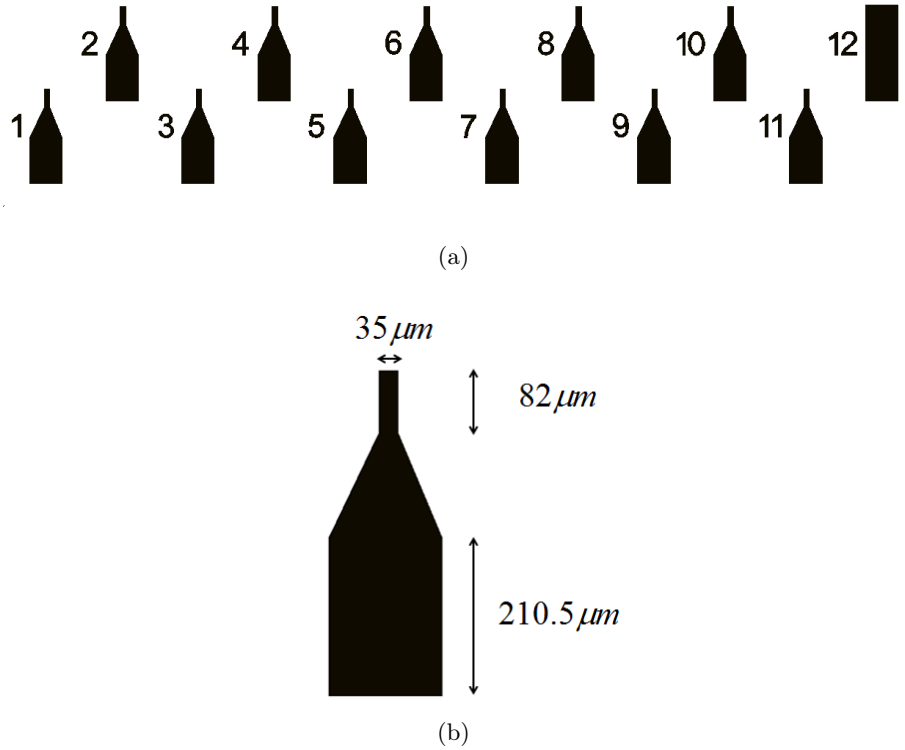

Figure 4.4: First step of lithography: (a) MESA definition for the 12 sensors and (b) zoomed image of the single structure.

The first step consists in the physical separation of the different sensors through the definition of MESA, that is a structure which includes the junctions' area and the bottom contacts (figure 4.4).

In the second step the actual shape and active area of each sensor is defined carving a pillar of $3 \times 40 \mu m^2$ in the MESA (figure 4.5). This choice results from a compromise between different requirements. On one hand, the promotion of an easy axis of magnetization induced by shape anisotropy requires a high aspect ratio, but on the other hand, in order to achieve a uniform current density throughout the junction area, one should avoid edge effects, reducing the perimeter on area ratio. Moreover, a small junction's active area is necessary to reduce the risk of defects that would lead to a loss in the TMR. However, with constant barrier thickness, small areas present higher resistance respect with larger ones, thus bringing to higher 1/f noise (see section 2.4). For this reason, during this thesis work, some efforts have been made in order to study the impact of the RA product and hence of the

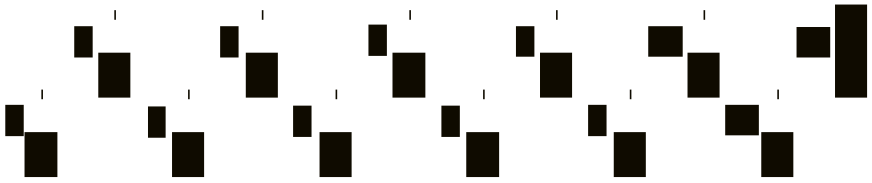

(a)

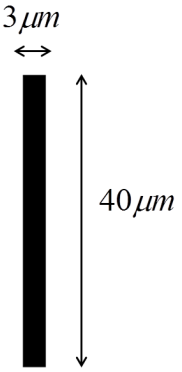

(b)

Figure 4.5: (a) Pattern of the second step of lithography. For the sensor number 12, designed for the microchip's temperature control, this step is a reply of the first one. (b) zoomed image of the single pillar: junction size of $3 \times 40\mu m^2$.

barrier thickness on the noise of the device (see section 5.3). Finally, small junction area means also smaller biological active areas, so a lower biological signal; this can be however compensate by a higher TMR ratio and therefore a higher sensitivity of the device.
Once defined the junction pillars, a SiO2 film is deposited in order to electrically insulate the top and the bottom electrode and to prevent the pillars edge from further oxidization.

In the third step the electrical contacts are defined (figure 4.6). The top pads are in ohmic contact with the top CoFeB electrode of the MTJ, while the bottom pads, deposited on the MESA, provide the contact with the bottom CoFeb electrode. This last contact is not ohmic, since it is made through the MgO barrier. However, since the contact area is bigger respect to the junction area, the bottom contact resistance is negligible with respect to the junction one. In figure 4.7 (a) and (b) a 3D view of the patterning

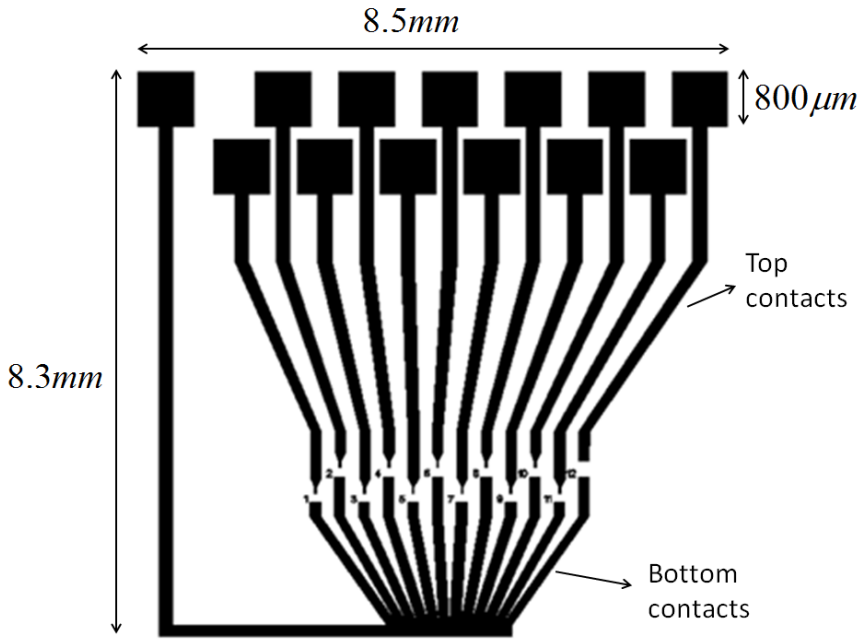

Figure 4.6: Third step of lithography: contacts definition.

is showed. All the bottom contacts are short-circuited and connected to ground, whereas the top contacts are independent, allowing the parallelization of the signals coming from the individual sensors. The size of the tracks has been studied to ensure a negligible resistance compared to the junctions one ($\approx k\Omega$), but also to avoid big parasitic capacitances.
All pads are much larger than the tracks, to avoid edge effects, and are positioned on the same side of the mask to be easily contacted by metallic retractable tips (having a diameter of 500 μm). The pads are squares of 800 μm side, placed at a distance of 400 μm between them, to avoid cross talking between the different signals.

As explained before, the first phase of the biological experiment is the selective functionalization of the sensors'active area. This requires a step of optolithography that simply consists in a reply of the junctions (fig.4.8). A spotter machine with a 80 μm size tip will be used to spot the probe DNA over the sensors. For this purpose, in order to take into account the uncertainty in the positioning of the tip during the spotting, the distance between the rectangles, and hence between the sensors, is chosen greater than 500 μm.

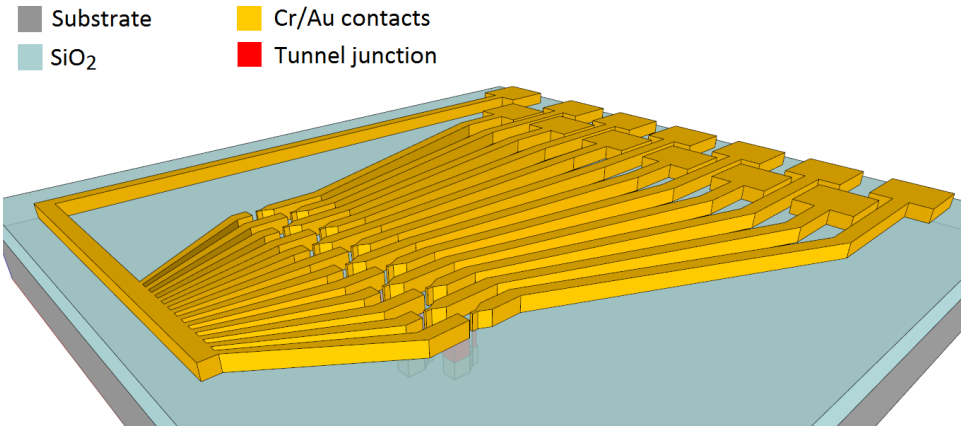

(a)

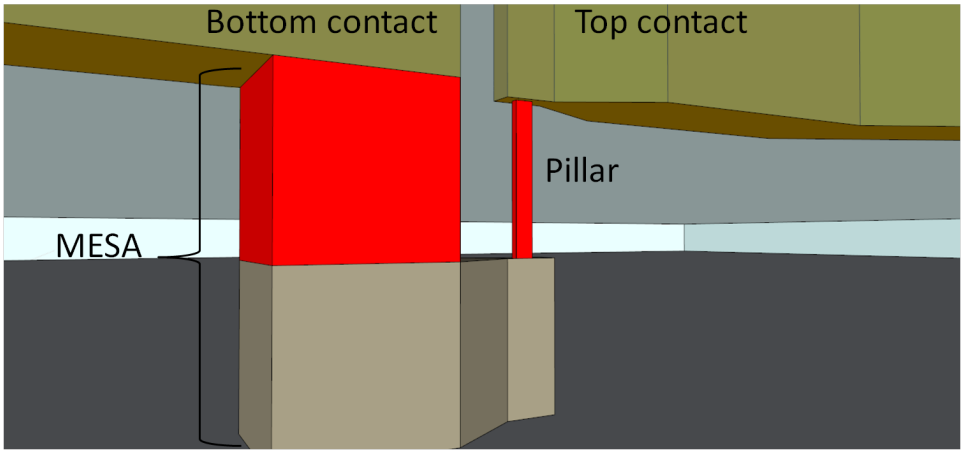

(b)

Figure 4.7: (a) 3D view of the patterned chip and (b) zoomed image of one sensor.

A temperature control is necessary to maintain the chip at about 50 °C, that is the temperature required for a typical hybridation process between target and probe DNA. For this purpose the chip can be mounted on a sample holder with an integrated heater (fig. 4.3), or the heater can be placed in a housing just inside the box (fig. 4.1). The heater, namely a flexible silicone heatermate with etched foil heating elements, will be controlled by a PID system and a thermocouple in thermal contact with the sample holder. Sensor number 12 is designed for the microchip's temperature control. Indeed its second step is a reply of the first step without carving the pillar in

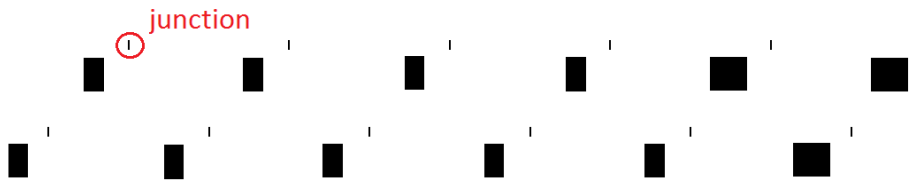

Figure 4.8: Sketch of the optolithographic process for the biofunctionalization of the sensors.

the MESA. In this way the area in which the current flows is so big that the sensor becomes purely a resistance, because the tunneling is negligible respect to the numerous available conductive channels. A variation of this resistance can be associated to a variation of temperature that can operate a control system on the heater. A uniform temperature profile throughout the whole chip is ensured by the use of a silicon substrate, which has a thermal conductivity higher than the glass substrates often used for the growth of MTJs, and by a suitable choice of the sample holder material, which can be aluminum or an appropriate ceramic (i.e. Macor).

4.2 The Electromagnet

The design of the electromagnet has been chosen taking into account all the geometrical requirements of the complete platform, first of all considering the necessary space for placing the chip, with the relative microfluidic cell. With this need, a horseshoe magnet has been designed, in such a way that the chip can be inserted in the upper gap between the poles, and immersed in a uniform magnetic field. With this configuration the plate for heating can be easly positioned inside the free space in the geometry, as in figure 4.1.

The electromagnet has been designed to produce a magnetic field of $\pm$ 50 Oe in DC, which is, to a good approximation, the value of the magnetic field required for biasing the sensors in their most sensitive point of the transfer curve (see the experiments of molecular recognition in chapter 6). All the sizes have been chosen in order to ensure a magnetic field as uniform as possible inside the air gap where the microchip will be positioned, with the minimum current required, lower than 500mA, for reducing the power dissipation and the heating by Joule effect.

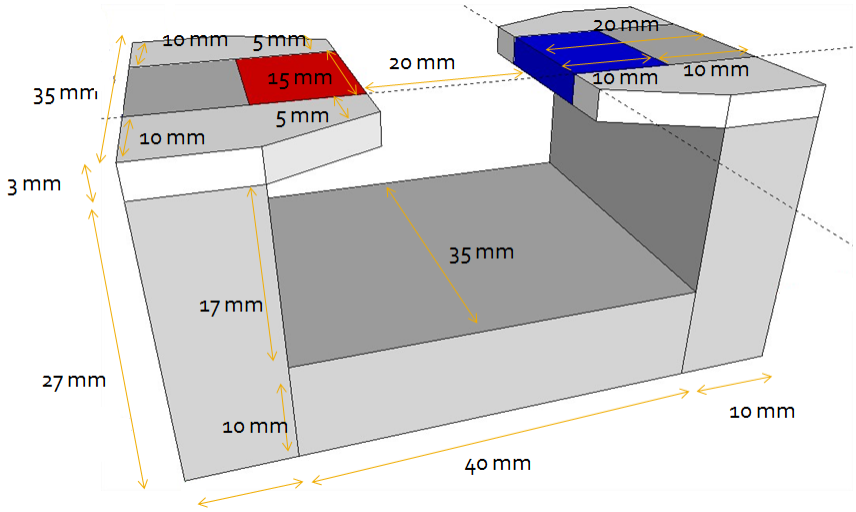

(a)

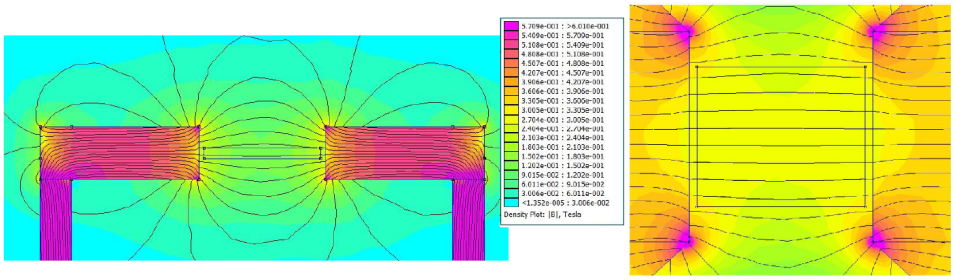

(b)

Figure 4.9: (a) Electromagnet with a horseshoe shape. All the dimensions are indicated. (b) On the left, side view of the distribution of the intensity of the magnetic field H calculated by FEMM; on the right, top view of the same distribution, only in the region of interest, where the sensors are positioned. The simulations and calculations have been carried out by Andrea Fogliani, for his thesis work [34].

In figure 4.9 (a) all the dimensions are presented, and the low panel (4.9 (b)) shows the distribution of the intensity of the magnetic field H calculated by the simulation program FEMM (Finite Element Method Magnetics). The simulations show an almost uniform field in the region of interest, as displayed by the flat field lines and by the uniformity of color in the region of the air gap of figure 4.9 (b).

The material chosen for the electromagnet is the stainless steel, grade 416, for its high magnetic permeability and low magnetic remanence (indeed the electromagnet, after being switched off, must return to the initial conditions

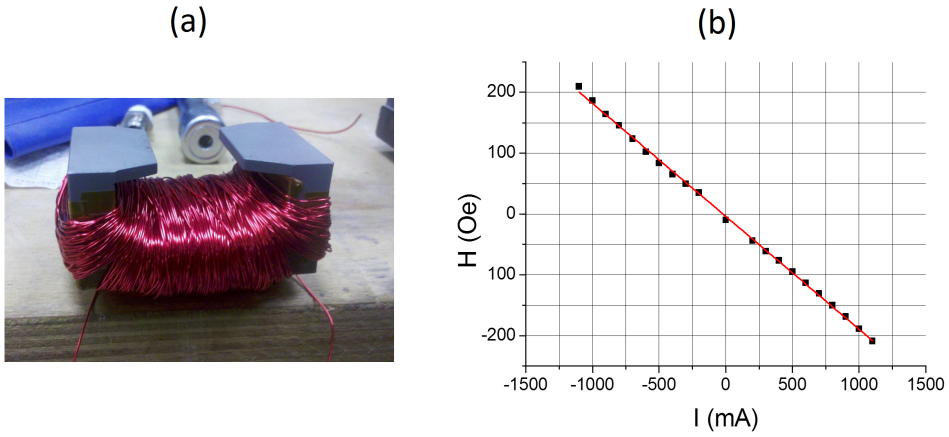

Figure 4.10: (a) Picture of the final electromagnet to be integrated into the platform. (b) Characterization curve of the electromagnet varying the current from -1.2 A to 1.2 A: a magnetic field of 50 Oe is obtained with a current of 300 mA. The electromagnet shows a remanence field of 10 Oe, which has to be compensated during all the calibrations and experiments, automatically via software.

in order to be used several times without invalidating the test). The current is generated by 480 windings of copper wire (diameter: d=0.5 mm), that wrap the magnet. In figure 4.10 the final electromagnet and its characterization curve are showed [34].

4.3 Microfluidic cell

The platform proposed includes a microfluidic system to confine the biological fluid volume to the sensing area, to control the flow rate of the experience and to improve the stability of the immobilized beads.
The microfluidic system is still being designed, and will be realized in collaboration with the Department of Chemistry, Materials and Chemical Engineering of Politecnico di Milano. Only two parts of the microfludic cell will be "disposable": the inlet and outlet tubes and the microfluidic chamber, defined by a gasket in Poly-DiMethylSiloxane (PDMS). PDMS is a flexible and transparent polymer and is one of the most widely used materials since it is cheap and biocompatible. The bearing structure of the system, showed in figure 4.11, consists of two separate parts in polycarbonate (PC) (all the

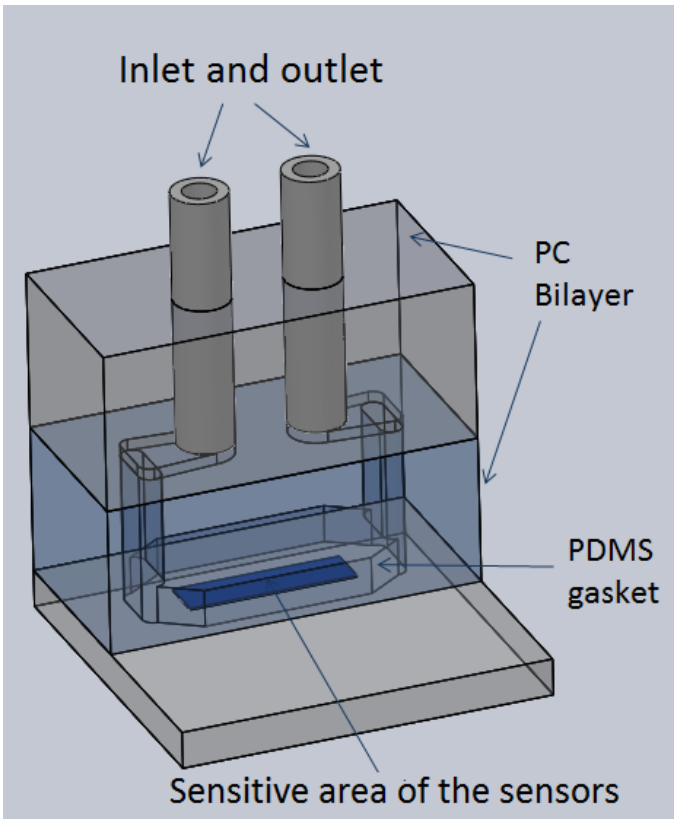

Figure 4.11: Microfluidic system with the two chambers in polycarbonate.

dimensions are showed in figure 4.12). The first layer works as a buffer chamber to contribute to the development of the flow prior to the arrival at the sensitive area. Indeed the type of flow occurring in a fluid is very important in fluid-dynamics problems. Depending on the the particular flow geometry and conditions the flow can be laminar or turbolent. The first occurs at lower velocities when a fluid flows in parallel layers, with no mixing between the layers. In this regime the flow is governed by the viscous forces, and its speed profile does not vary in time. A turbolent flow instead is a chaotic flow regime, in which rapid variations of pressure and velocity occur in space and time. In a microfluidic system, because of the dimensions involved, the flow can be considered laminar. It is therefore important to carefully design every component, in order to obtain a reduced and uniform velocity inside the area in which the sensors are placed, especially during the washing step. Indeed, in this phase of the experiment, a uniform washing flow across the

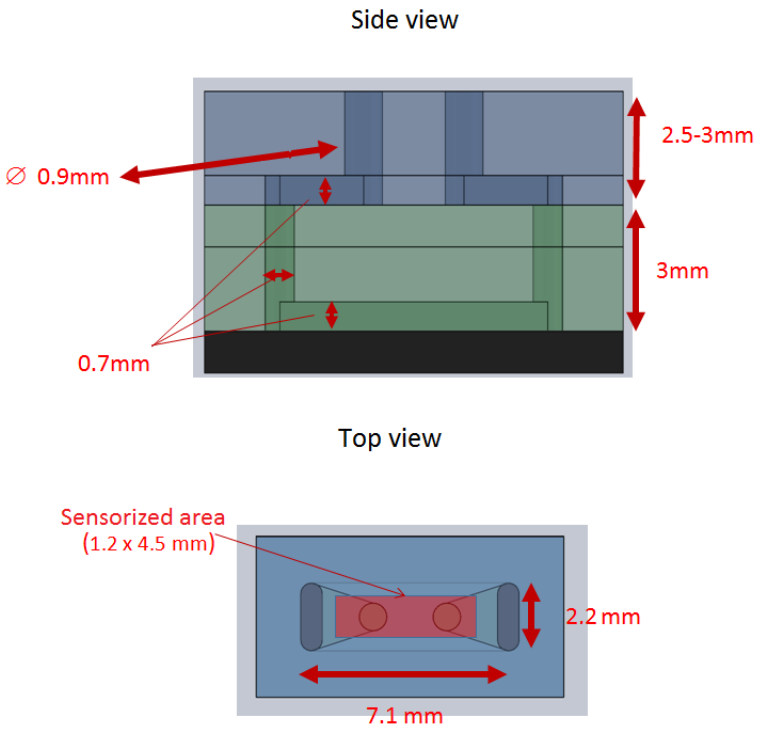

Figure 4.12: Side and top view of the microfluidic system. All the dimensions are indicated.

microfluidic cell is necessary to ensure the same effect on all the sensors. A different signal from the control sensors may in fact cause ambiguity, compromising the success of the experiment

From the color maps in figure 4.13, it is possible to observe that the sizing of the components allows to obtain a quite homogeneous velocity ($\pm 10\%$) in the area occupied by the sensors, as well as a homogenous shear stress on the surface of the latter ($\pm 6\%$).

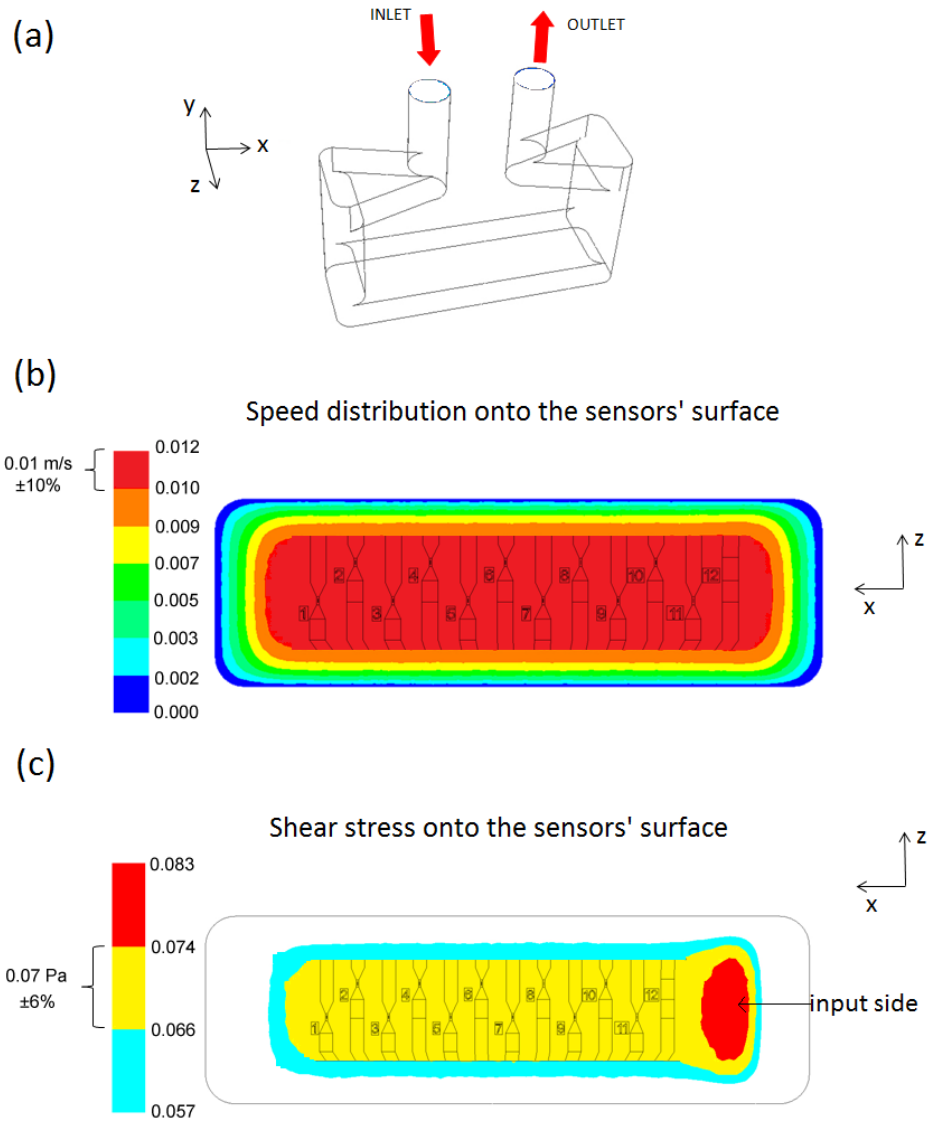

Figure 4.13: (a) 3D representation of the microfluidic channel. Color map of the velocity (b) and of the shear stress (c) onto the sensors' surface (Courtesy of E. Bianchi, F. Nason and G. Dubini (CMIC)).

4.4 Electronic platform

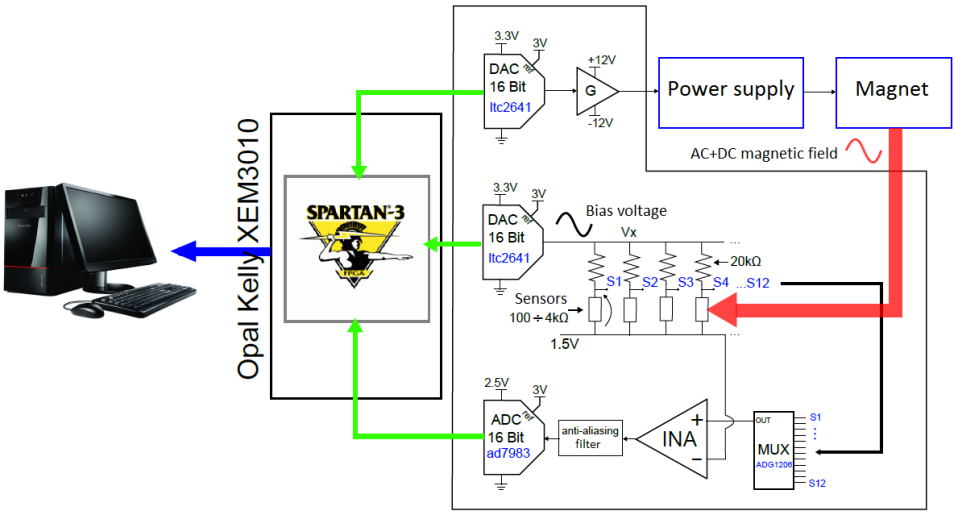

Figure 4.14: Schematic diagram of the electronic platform designed for the biological assay with the magnetoresistive sensors.

The electronic platform has been designed with these requirements: (i) providing the sensors multiplexing and the signals required to perform the magnetic and electric drive of the biochip; (ii) performing real-time signal processing; (iii) providing interfaces to transmit the signals to a smartphone or a laptop computer; (iv) to achieve a portable system, low power consumption, reduced size and weight.

Figure 4.14 shows a sketch of the complete electronic platform prototype. This includes the generation of the current signal for biasing the sensors (showed in the middle part of the image), the generation of the power supply for driving the magnet (in the top part of the image) and the signal acquisition (in the bottom). All the circuit is then connected to a control board (XEM3010) that integrates an FPGA Spartan-3 board which provides the interface to a PC or smartbox. Detailed circuitry design can be found in [40]. In figure 4.15 (a) a picture of the final electronic platform is showed. To illustrate the measurement capabilities of the developed system, an experiment of sedimentation beads has been performed (panel b of fig. 4.15). The details of the experiment are those described in chapter 6.

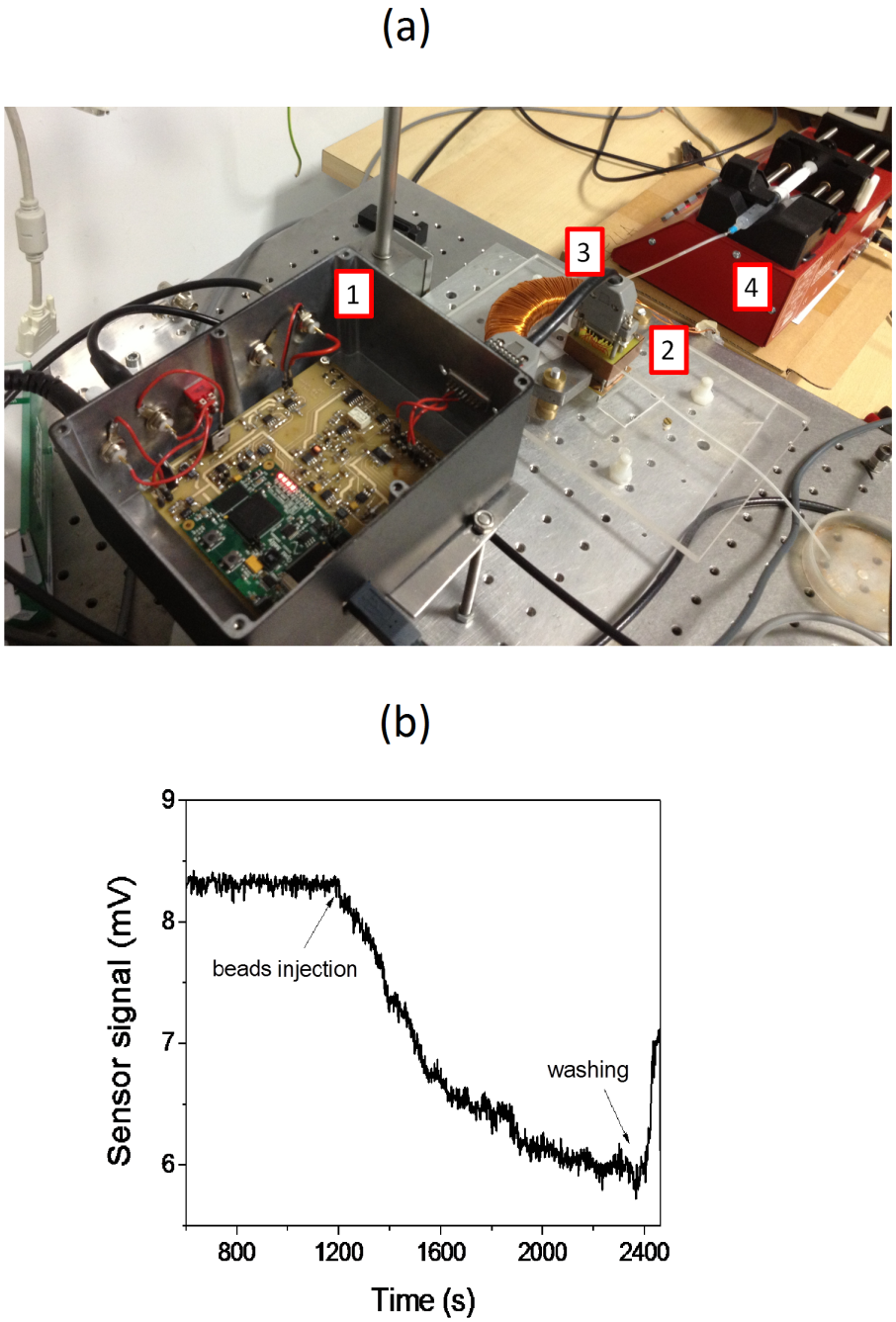

Figure 4.15: (a) Picture of the final electronic platform connected with our instrumental apparatus for the experiment of sedimentation beads: 1 is the electronic platform, 2 is the microfluidic system with the magnetic chip inserted between the poles of the electromagnet, 3 is the multiplexer, 4 the syringe pump. (b) Sedimentation beads signal which demonstrates the operation of the electronic platform.

Chapter 5

Sensors optimization and characterization

The platform project described in the previous chapter requires to reach limits of detection less than fM. In order to achieve such a high sensitivity, it is necessary to further improve the current state of the art of the sensors fabricated at LNESS. Indeed, despite in the last years, the work of my research group has led to the realization of MTJ-based sensors with good sensitivity and TMR ratio, compared to the state of the art [91], [3], more efforts have to be done. In particular, since we are dealing with a real biological system which obviously carries many problems by itself, a fundamental requirement is the reliability of the sensors. Because high TMR ratio can be usually obtained in small size junctions due to the reduction of defects in the barrier, the first step to enhance our sensors' performances has been to go down to smaller junction area, from $2.5 \times 120\ \mu m^2$ to $2.5 \times 30/50\ \mu m^2$.
However, since the product resistance-area (RA) is constant for a fixed barrier thickness, this choice has led, as expected, to an increase of the sensor resistance. According to calculations in paragraphs 2.1.3 and 2.4, thermal and 1/f noises increase for higher resistances, while the tunneling resistance-area product increases exponentially with respect to the barrier thickness. For this reason to riduce the intrinsic noise of the MTJ junctions, many sensors, having different MgO thicknesses, starting from 2nm down to 0.9nm, have been grown and characterized during this thesis work. The optimized sensor will be that with best sensitivity and linearity of transfer curve, less resistance and accordingly less noise.

5.1 Sensor's optimization

The first part of the work has dealt with the optimization of the sensor stack, starting from the most critical aspects of a TMR junction: the quality of the MgO barrier and the pinning of the bottom ferromagnetic layer.
In magnetic tunnel junctions the interface with the barrier greatly influences the performance of the sensors. From the considerations of the previous paragraph, in order to reduce the intrinsic noise of the sensors, very thin MgO barrier has to be used. This implies a very good control on its crystalline structure, to enhance the local spin-dependent tunneling, and to improve the TMR ratio. Since the high quality of the MgO film in our sensors has been already tested in different works [90] [91], the first step of the optimization process has regarded the SiO_2 substrate, since its roughness impacts directly on the overlying layers.
Regarding the optimization of the pinning of the bottom layer, in the first phase of the work the exchange bias at the antiferromagnet/ferromagnet interface has been studied, while in the second phase the otpimization process has focused on the synthetic antiferromagnet. The optimization and balance of the SAF structure is very important to pin the bottom layer in a large magnetic field range and to avoid magnetic coupling between the pinned and free layer, which would led to residual hysteresis and shift of the transfer curve. During this work some efforts have been done in this context, improving the state of the art of the sensors fabricated at LNESS.
In the next sections all the results obtained are presented.

5.1.1 Roughness optimization of the substrate and MgO

The MgO roughness has been checked by Atomic Force Microscopy (AFM) measurements (Veeco Innova) in different conditions. Single layers of MgO have been grown on two substrates of SiO_2 with different thicknesses of 100 nm and 1000 nm. The choice to use these different substrates will be justified later, in reference to the noise measurements performed in section 5.3.
From surface topology images acquired in tapping mode, the Root Mean Square Roughness values (R_{rms}) are obtained calculating the standard de-

Sample	SiO_2 thickness (nm)	MgO thickness (nm)	Substrate cleaning	R_{rms} (nm)
R1	100	9[1]	acetone and isopropanol	3.36
R2	100	2	piranha	1.05
R3	100	2	piranha + soft etch	0.7
R4	1000	2	piranha + soft etch	0.82

[1]Calibrated thickness.

Table 5.1: Samples grown and characteristics, including the SiO_2 and MgO thicknesses, the substrate cleaning and the roughness rms obtained.

viation of the surface height for the sample area:

$$R_{rms} = \sqrt{\sum_{n=1}^{N} \frac{(Z_n - \overline{Z})^2}{N}}, \tag{5.1}$$

where $\overline{Z}$ is the average height of the surface and N is the number of points in the area. All the calculations are performed with a sample area value $A = 100\mu m^2$.

In table 5.1 the various samples tested are listed, showing their differences and the corresponding rms roughness obtained. In the first case (sample R1) 20nm of MgO have been grown on the 100 nm SiO_2 substrate after a cleaning in acetone and isopropanol, with the main purpose of performing a calibration of the deposited thickness. Subsequentely, single layers of thickness comparable to those of the final stack (2 nm) have been grown in different conditions. In all these samples the rate of deposition obtained after the calibration has been used (1.58 Å/min). In sample R2 the substrate (100 nm SiO_2), first cleaned in acetone and isopropanol, has been cleaved with photoresist and than cleaned with piranha solution to clean organic residues. In the case of sample R3, after the same chemical treatment, a soft etch in the deposition chamber has been performed before the growth (10 minutes at 30W, with Argon pressure of 2mTorr), to further cleaning the substrate surface, removing the residues arising from the cleavage and from the exposure to air. In the last case (sample R4) the MgO film has been grown on the thicker substrate (1000 nm SiO_2), which as been treated as in the case of the previuos sample.

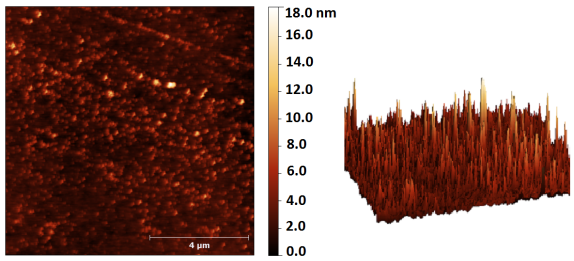

Sample R1

(a)

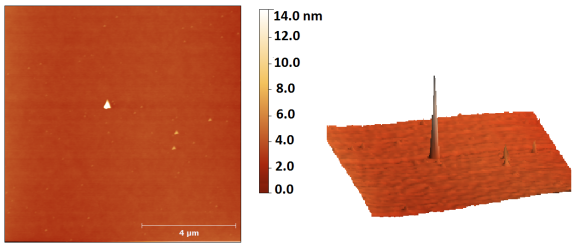

Sample R2

(b)

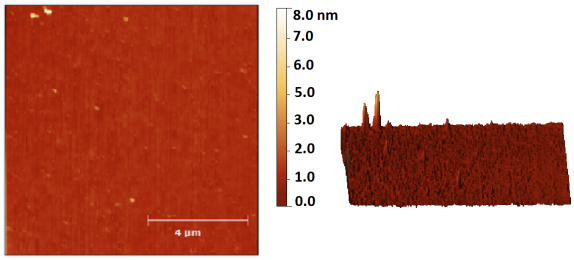

Sample R3

(c) .

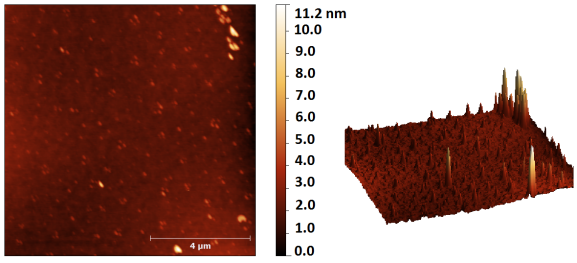

Sample R4

(d) .

Figure 5.1: AFM image and 3D view of MgO of Sample R1 (a), Sample R2 (b), Sample R3 (c) and Sample R4 (d).

Figure 5.1 shows surface topology images acquired through Atomic Force Microscopy for each sample (for an area of $10 \times 10 \mu m^2$ comparable with the junction area). Sample R1 shows a strong particle-like texturation of the surface, with a roughness of 3.36 nm rms. This fact has been imputed to the substrate, and not to MgO itself, since the presence of any defects or impurities impacts directly on the roughness of the overlying layers. Indeed AFM measurements of the substrate (figure not shown) reveals a higher roughness of 3.8 nm rms in an area of 100 μm^2, demonstrating that, even with only 2 nm of MgO we recover a higher degree of smoothness. This means that MgO films, alone, present a lower roughness.
Moreover a remarkable improvement is noticed, respect with the non optimized sample, when the substrate is cleaned. Indeed the strong particle-like texturation of the surface is removed with a reduction of the roughness from a value of about 3.36 nm rms to 1 nm rms, in the case of sample R2, and to 0.7 nm rms in sample R3. Sample R4 shows instead a slightly higher roughness of 0.82 nm rms.
Despite the improvements obtained during this characterization, the roughness still remains high in comparison with the MgO thickness of the sensor's stack, that in the course of this work will be reduced down to 0.9nm. However, it has to be considered that in the real junction the surfaces of the underlying layers result very smooth, reducing the impact of the defects' substrate on the roughness of the MgO film [91], [5].

5.1.2 Exchange Bias

In this part of the work the exchange bias at the antiferromagnet/ferromagnet interface has been studied.
The sample's structure is Si/ SiO_2(100nm)/ Ta(5nm)/ Ru(18nm)/ Ta(3nm)/ IrMn(20nm)/ $Co_{40}Fe_{40}$(2nm)/ Ru(1.3nm). During the stack deposition a field of $\sim 300Oe$ has been applied, defining a net exchange bias in the field direction in the as-deposited sample. Then the sample has been annealed for 1 hour raising the temperature, with a ramp of 5 °C/min, from room temperature to 300 °C, keeping the pressure at around 10^{-6} Torr. A magnetic field of 400 mT has been applied along the EB direction. Then the heating has been switched off and the sample field cooled back to room temperature. The MOKE measurements have been performed with a magnetic field H_{ext} applied parallel to the direction of the exchange bias. The main results are

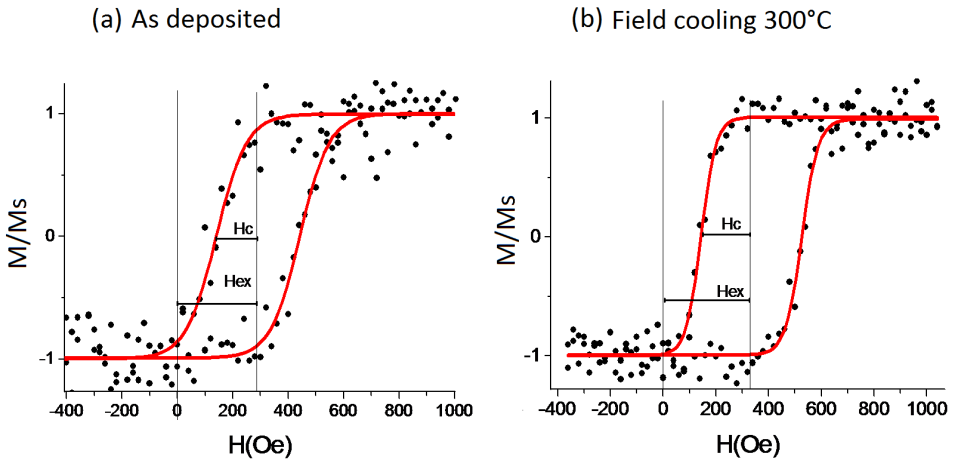

Figure 5.2: Hysteresis loops (black dots) and fitting of the data (solid red line), for Ta(5nm)/Ru(18nm)/Ta(3nm)/IrMn(20nm)/CoFe(2nm)/ Ru(1.3nm) before (a) and after (b) field cooling.

presented in figure 5.2 where the effect of the field cooling is evident on two main parameters: the exchange bias field H_{ex} and the coercive field H_c. The field cooling increases the exchange bias field from a value of $H_{ex} = 290Oe$ to $H_{ex} = 330Oe$, which is largely sufficient for our applications. This reflects the fact that the coupling between antiferromagnet IrMn and ferromagnet CoFe is strong. Moreover the coercive field increases from $H_c = 150Oe$ to $H_c = 180Oe$ because of the improvement in the structure crystallization. However, this could be a drawback in terms of magnetic stability, because, despite the increase of 40 Oe of the exchange bias field after the field cooling, the coercivity accordingly widens of 30 Oe, resulting in a distance (H_{ex}-H_c) only 10 Oe wider than before.

Moreover respect to the state of the art [5] in which the exchange bias is partially damaged by interdiffusion when the sample is heated above 250 °C, a good thermal stability has been obtained in this work, allowing a good crystallization of the MgO.

5.1.3 Optimization of the Synthetic antiferromagnet

As it has already been explained in chapter 2.1.2, the pinning of the botton layer is achieved through the synthetic antiferromagnet (SAF). Indeed CoFeB bottom layer is pinned antiferromagnetically to CoFe through a Ru spacer by

bilinear exchange coupling, while CoFe is in turn directly pinned by exchange bias with the antiferromagnet IrMn.
Two main aspects have to be considered for a good optimization of the synthetic antiferromagnet: the stability of the coupling and the balance of the SAF. The first has already been managed by this group and has been further optimized in this work. To achieve a strong coupling, necessary to maximize the exchange bias, to improve the thermal stability and to reduce the effective moment of the pinned layer, a study of the Ru thickness and of the best annealing temperature has been carried out. Regarding the second aspect, the balanced SAF configuration is obtained when the magnetizations of the two FM layers are compensated. In this case the stray field from the synthetic antiferromagnet is minimal and the field range for which the two magnetic layers are antiparallel is maximal, leading to achieve hysteresis free sensors because there are no interactions between the free top layer and the bottom layer. The problem of the unbalanced SAF has been observed in this work, for the first time in this group, and the study performed to reach the compensation condition is presented in the following.

Choice of the best Ru thickness

As already explained the first part of the optimization is a study of the best Ru thickness which maximizes the coupling. Four different heterostructures have been studied varying the thickness of Ru: Ta(5nm)/Ru(18nm)/Ta(3nm)/ IrMn(20nm) /$Co_{40}Fe_{40}$(2nm)/Ru(x)/$Co_{40}Fe_{40}B_{20}$(3nm)/MgO(2nm), where x corresponds to 0.7, 0.9, 1.1, 1.3nm. During the stack deposition a field of $\sim 300Oe$ is applied, and each sample has been then annealed for 1 hour raising the temperature from room temperature to 300 °C with a ramp of 5 °C/min, in a magnetic field of 400 mT applied along the EB direction.
The hysteresis loops have been recorded by employing a vibrating sample magnetometer (VSM) and are reported in figure 5.3. Here the important parameter to observe is the loops separation H_x that is proportional to the bilinear coupling. Starting from the higher Ru thickness, 1.1nm and 1.3nm (panel (b) and (d)) the coupling is ferromagnetic, as shown by the square hysteresis loops, slightly shifted towards negative field due to the exchange bias of the CoFe film. These results are in agreement with the oscillatory behavior of the bilinear coupling [86]. Note that for all these samples the unidirectional anisotropy axis of the exchange bias is in the positive direction

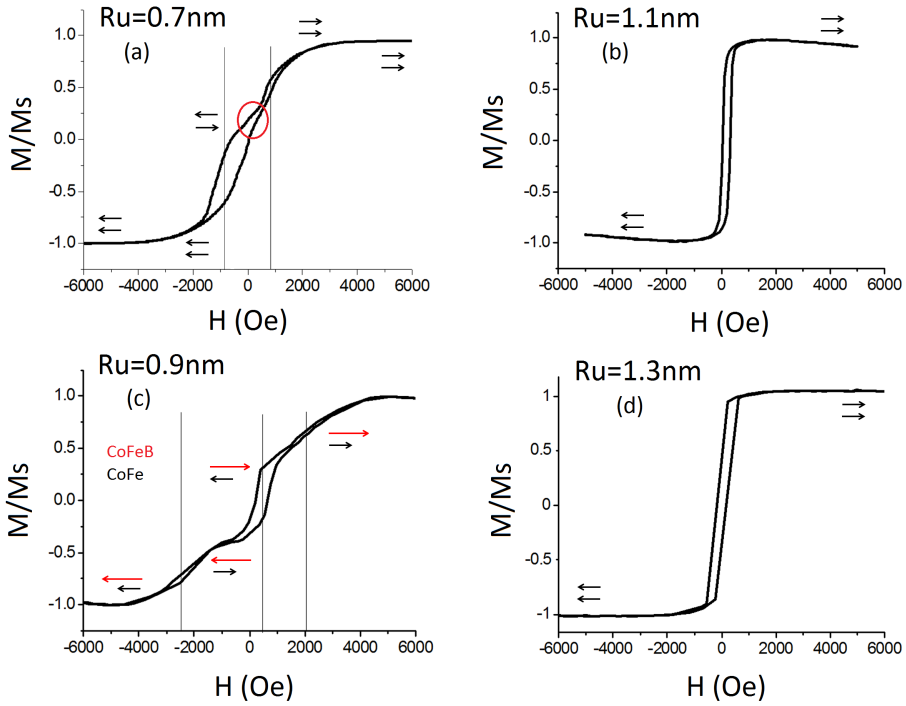

Figure 5.3: Hysteresis loops of SAF structures: Ta(5nm)/Ru(18nm)/Ta (3nm)/IrMn(20nm)/CoFe(2nm)/Ru(x)/CoFeB(3nm)/MgO(2nm), with different Ru thicknesses x=0.7 (a), 0.9 (c), 1.1 (b), 0.13 (d) nm, measured after a field annealing at T=300 °C. The arrows indicate the orientation of the magnetic moments of the two layers, CoFe and CoFeB.

of fig. 5.3, leading to a loop shifted towards negative values.

In the case of Ru=0.7nm the bilinear coupling is present but very weak (panel (a) in fig. 5.3). Indeed when the field swept from negative to positive the magnetization continuously increases, quite as in a single loop, as it happens for the loops with Ru=1.1 and 1.3 nm. However this is a mid-way condition between the previous ones and a real bilayer copuling. Indeed, in the opposite direction of the field, there is a weak antiparallel coupling between CoFe and CoFeB but the two cycles are not well separated. The asymmetry between back and forth sweeps is maybe ascribed to different spin rotation mechanism induced by the unidirectional anisotropy. Moreover, in the central region a small cycle (highlighted in red), is visible, and is probably due to a lack of compensation of the magnetizations of the two layers, which becomes more visible in figure 5.3 (c), in the case of Ru=0.9

nm. Here an antiferromagnet coupling is apparent even if three different cycles are visible. The magnetization curve is not symmetrical with respect to zero field. Starting from negative values of the magnetic field, the first cycle is mainly attributed to the rotation of the exchange biased CoFe which starts at about -2500 Oe, due to the combined effect of the exchange bias field and to the exchange coupling field. Then a plateau is reached at about -1000 Oe corresponding to an antiparallel configuration of the magnetizations. At about 680 Oe a jump and then a rotation towards saturation at +2000 Oe is observed. The loop centerd at +2000 Oe is attributed mainly to the rotation of CoFeB. The two lateral loops are separated of about 4500 Oe, a high value compared to that of 2000 Oe obtained in previous samples in this group [91].

Note that the cycles are very narrow and elongated, difficult to measure even with a sensitive technique like VSM. This is due to the limitated thickness of the FM layer and to the effect of the unbalanced bilayer coupling.

However, the central loop of figure 5.3 (c) reveals again the fact that the magnetization of the two FM is not compensated, leading to an unbalanced SAF. Looking at the plot, it is clear that the total magnetization crosses zero at positive field, which corresponds to a higher total magnetic moment of the CoFeB respect with that of CoFe. In order to better understand the rotation mechanisms leading to the plot of fig. 5.3 (c) a simple model can be developed. Following the same calculations in [109], [68], the angles of the magnetizations with respect to the applied field can be estimated by minimizing the energy of the system. In this model the total areal energy in the SAF structure can be written as follows:

$$E = -t_1 M_1 H \cos\theta_1 - t_2 M_2 H \cos\theta_2 - J_{ex} \cos\theta_1 - J_{inter} \cos(\theta_1 - \theta_2), \quad (5.2)$$

where M_1, M_2, t_1 and t_2 are the magnetic moments and the thicknesses of respectively CoFe and CoFeB, θ_1 and θ_2 are the angles of the magnetizations in the bottom and the top layers with respect to the applied field (see figure 5.4 (a)), J_{ex} and J_{inter} are respectively, the exchange coupling energy between CoFe and IrMn and the interlayer coupling energy induced by the Ru spacer between the two ferromagnets.

The two angles as a function of H, applied in the exchange bias direction, as in the experimental condition, have been calculated by minimizing eq. 5.2.

Despite the polycrystalline nature of the films, the model assumes only rotation of the magnetic moments rather than domain wall nucleation and propagation. Indeed this simplification is valid in case of strong antiferromagnetic coupling, as in the case of this SAF system. A further confirmation of the validity of this model is in the loops of figure 5.3 (c), which, apart from the central loop due to the uncompensated magnetizations, present very low hysteresis which normally is associated to the absence of domains.
For the calculations the following parameters have been used:

- $M_1 = \mu_0 \cdot 1.9 \cdot 10^6$ A/m, $M_2 = \mu_0 \cdot 7.96 \cdot 10^5$ A/m [12];
- $J_{ex} = 0.19$ mJ/m^2 and J_{inter} = -0.22 mJ/m^2, obtained from IrMn/CoFe bilayers and CoFe/Ru(0.9nm)/CoFeB sandwiches from [103].

The obtained curves are showed in figure 5.4 (b). Starting from saturation at high negative field, first the bottom CoFe rotates 180° towards an antiparallel orientation with respect to the top CoFeB layer. During the reversal, which occurs at H = - 1000 Oe, the top CoFeB tilts away about 60° from its equilibrium direction due to the strong antiferromagnetic coupling with the bottom CoFe layer. At a positive field of about 700 Oe a fast rotation occurs in the top layer, and the bottom tilts away from its stable condition of about 25° to maintain the relative antiparallel orientation of the two magnetic moments. When the field is further increased the antiferromagnetic coupling is overcome, and the two moments finally align parallel to the field at about 1900 Oe. These results are in perfect agreement with the hysteresis loop in figure 5.3 (c), which is showed for a direct comparison even in figure 5.4 (panel c).
It is possible to conclude that at low external magnetic field, antiparallel configuration is achieved tilting the magnetic moments of the two ferromagnets from the equilibrium direction along the magnetic field and the exchange bias, but always keeping the strong antiparallel coupling.
Finally the best result in terms of bilinear coupling has been obtained with 0.9nm of Ru, in agreement with leterature [107], despite CoFe and CoFeB are not balanced

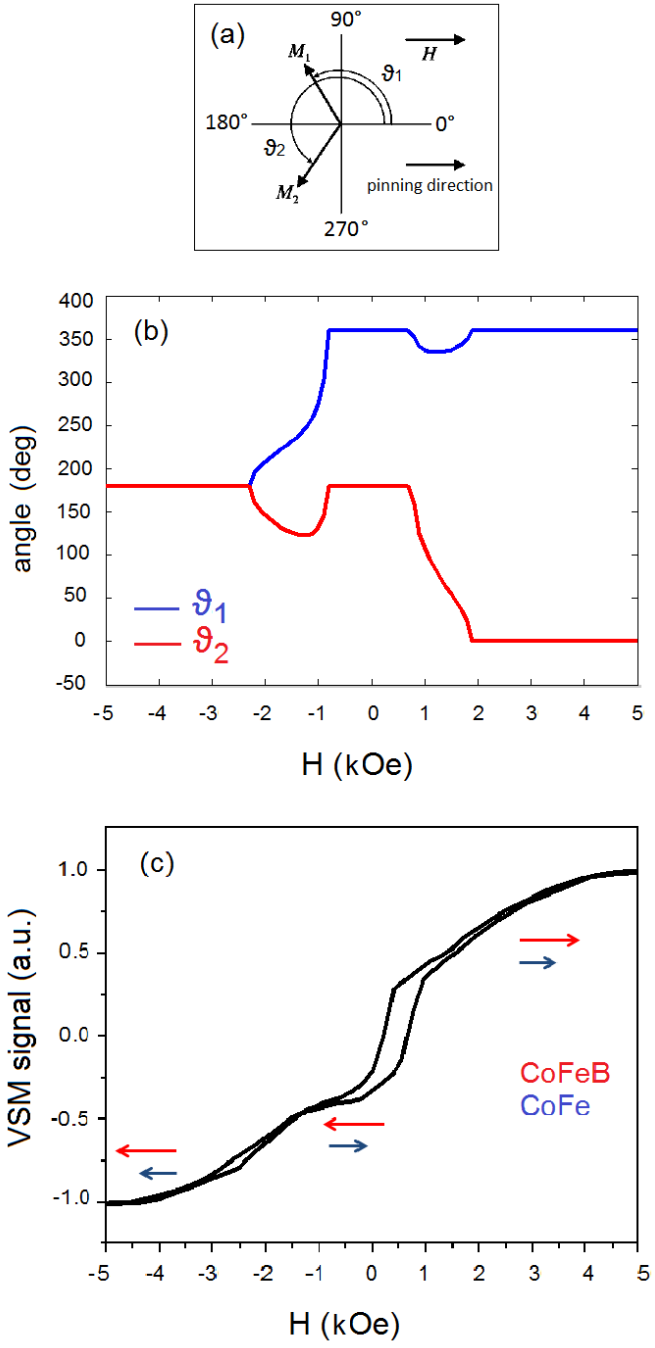

Figure 5.4: (a) Definition of the angles with respect to the applied field H and the pinning direction of the bottom CoFe layer. (b) Variation of the angle of the bottom CoFe (blu line) and of the top CoFeB (red line) as a function of the applied field. (c) Hysteresis loop of SAF structure (Ru=0.9 nm), corresponding to the rotation of the magnetic moments depicted in the upper panel.

Choice of the best annealing temperature and SAF compensation

In the second part of the optimization a study of the best annealing temperature is performed. In figure 5.5 the hysteresis loops for three different annealing conditions, 270 °C, 300 °C, 320 °C, and constant Ru thickness of 0.9 nm, are compared. The best result is obtained when an annealing at 270 °C is performed. Indeed in this case the loops separation is the largest (about 5550 Oe) and there is a net separation from the central loop. From now on, this sample will be named sample S1.

To overcome the problem of the compensation between the two layers, a

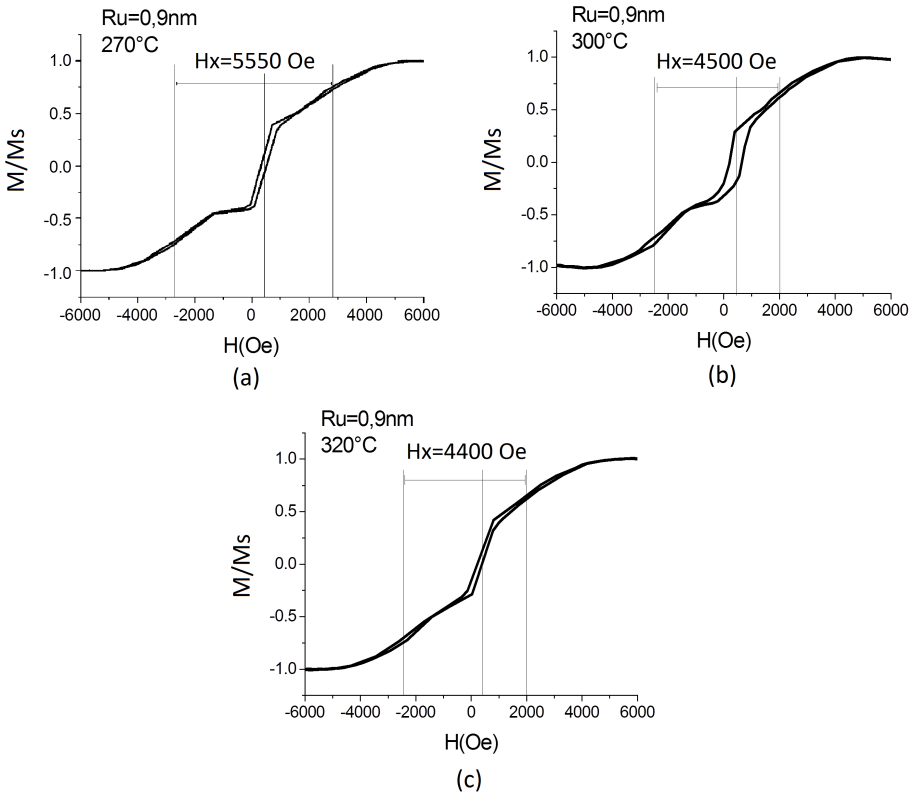

Figure 5.5: Hysteresis loops of SAF structures recorded by VSM: Ta(5nm)/ Ru(18nm)/Ta (3nm)/IrMn(20nm)/CoFe(2nm)/Ru(0.9nm)/CoFeB(3nm)/ MgO (2nm) annealed at 270 (a), 300 (b), 320 (c) °C.

new calibration of the deposition rates has been performed in order to study the balance of tha SAF as function of the thickness of the CoFeB and CoFe. In table 5.2 the different sample are listed and in figure 5.6 the corresponding

Sample	Thicknesses
S1	CoFe=2nm, CoFeB=3nm
S2, with "AFM calibration"	CoFe=2nm, CoFeB=3nm
S3, with "AFM calibration"	CoFe=2.5nm, CoFeB=2.5nm

Table 5.2: SAF samples grown and relative thicknesses of CoFe and CoFeB. In red the optimal condition.

hysteresis loops are showed (the optimal condition is showed in red).
Figure 5.6 (b) shows the hysteresis loop of sample S2 after the calibration of the two deposition rates. In this case the central loop is missing, even if this fact is ascribed to the increase of a ferromagnetic coupling between the two layers, which is attributed to the overall reduction of the thicknesses after the calibration. Indeed the two loops are much closer to each other then the previous sample (H_x = 1380 Oe). Moreover it is clear that the contribution of the CoFeB is still dominant (hysteresis loop shifted in the positive direction of the field). For this reason in sample S3 (fig. 5.6 (c)) the thickness of CoFeB has been reduced of 0.5nm, while the thickness of CoFe has been increased by the same amount (the deposition rates are maintained the same as that of the previous sample). Even if there is still a small loop in the central region of the hysteresis, the situation is greatly improved respect to the case of sample S2 in terms of bilinear coupling, and respect to sample S1 in terms of compensation. Moreover CoFe contribution has been increased, as showed by its wider coercivity, even if a further reduction in CoFeB's thickness would be necessary. Further improvements would be possible with a finer calibration of the thicknesses. However, MTJs with the SAF S3 result in a TMR with very low hysteresis and stray field, as will be discussed in the next section (see paragraph "TMR curves"). Moreover, it is worth to notice that despite the bilayer coupling is slightly lower, the stability of the pinned layer with the magnetic field is comparable with that of the other junctions with SAF S1.

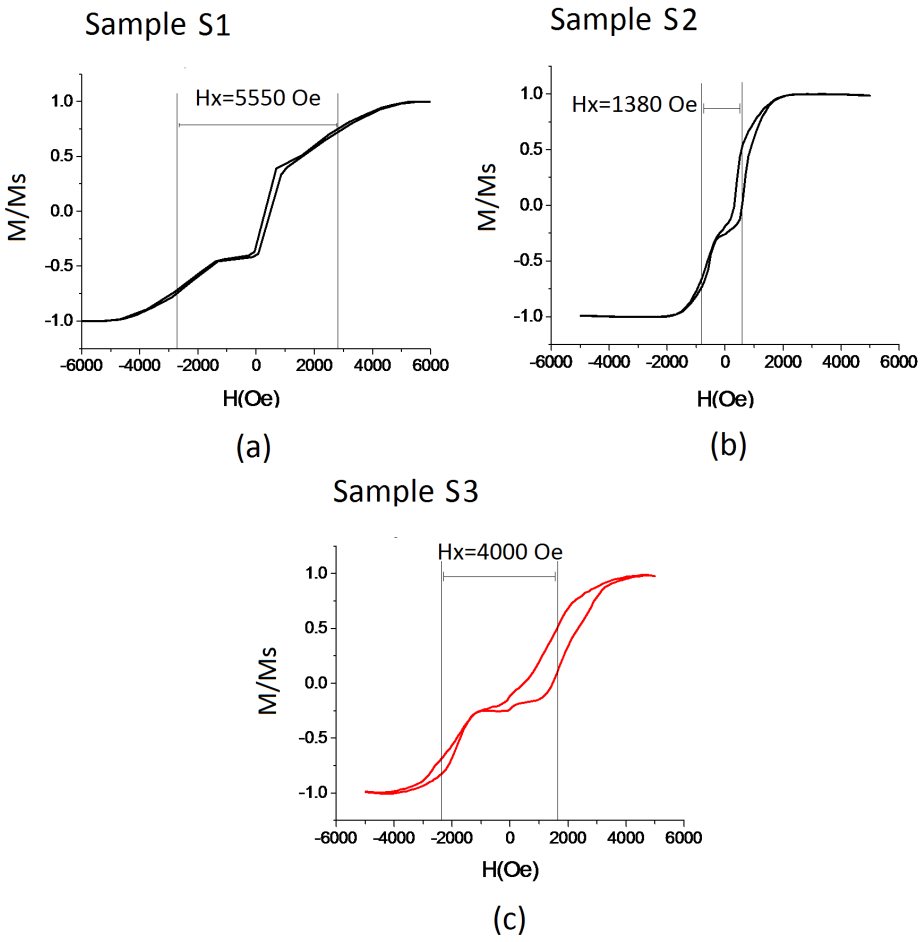

Figure 5.6: Hysteresis loops of SAF samples measured by VSM: Sample S1 (a), Sample S2 (b), Sample S3 (optimal condition) (c).

5.2 Sensors characterization

In this paragraph the characterization of the various samples fabricated as described in paragraph 3.1.6 during the thesis work is presented.
The main properties of the samples are summarized in table 5.3, and the multilayer stack of the sensors is shown in figure 3.11 in paragraph 3.1.6. Four kinds of stack have been tested, with different thicknesses of MgO (2nm, 1.23nm and 0.9nm) and of CoFe and CoFeB in the SAF structure (CoFe=2nm, CoFeB=3nm and CoFe=2.5nm, CoFeB=2.5nm). Thinner MgO thicknesses have been investigated in order to minimize the intrinsic noise of the MTJ which decreases with the barrier thickness, while the two kinds of SAF structure have been used to observe eventual changes in the hysteresis loops due to the optimization carried out in the previous section.
As mentioned before, during this work smaller junctions area have been tested, with respect to the case of the previous sensors grown at LNESS. The dimensions have been reduced from $2.5 \times 120\mu m^2$ to $2.5 \times 30/50\mu m^2$, and bigger contacts have been used ($20/40 \times 150\mu m^2$). Indeed high TMR ratio can be obtained in small size junctions due to the reduction of defects in the barrier. Bigger contacts on the oher hand prevents the formation of edge effects ensuring a uniform current to flow, thus improving the reproducibility of the devices. It is worth to notice that the chosen junction sizes are comparable to the ones of the platform project described in section 4.1, therefore, in first approssimation, the results obtained during this work can be considered valid even in that case.
In the first part of the characterization the study of RA product depending on the MgO thickness, is reported. Two points measurements have been performed for all the samples, using the instrumental apparatusas described in section 3.3. Then, the study of the TMR ratio and of the various hysteresis loops is carried out.
Finally the analysis of the noise spectra for two samples will be presented in section 5.3.

RA vs MgO thickness

In figure 5.7 (a) the RA product values for samples 1, 2, 3, 4 (with 2nm of MgO) are compared as a function of the sensor area. Figures 5.7 (b) and (c) show the RA values for samples 5 ,6 (1.23nm of MgO) and for sample 7

Sample	t_{SiO_2} (nm)	t_{MgO} (nm)	SAF structure CoFe, Ru, CoFeB	Sensors area (μm^2)	Contacts area (μm^2)	T_{ann} (°C)
1	100	2	2nm, 0.9nm, 3nm	2.5×50	20×150	300
2	100	2	2nm, 0.9nm, 3nm	2.5×30	20×150	300
3	100	2	2nm, 0.9nm, 3nm	2.5×30	40×150	300
4	100	2	2nm, 0.9nm, 3nm	2.5×50	40×150	300
5	100	1.23	2nm, 0.9nm, 3nm	2.5×30	40×150	300
6	100	1.23	2nm, 0.9nm, 3nm	2.5×30	20×150	270
7	1000	0.9	2.5nm, 0.9nm, 2.5nm	2.5×30	40×150	300

Table 5.3: Samples grown and critical parameters: SiO_2 substrate thickness, MgO thickness, SAF structure, sensors and contacts area, annealing temperature. In red the optimal condition of the SAF structure.

MgO thickness (nm)	Average RA ($k\Omega\mu m^2$)	Error bar
2	2201.7	±16%
1.23	419	±10.4%
0.9	14.03	±29%

Table 5.4: Average RA product and corresponding error bar for the three values of the barrier thickness.

(0.9nm of MgO).

As expected from the considerations in paragraph 2.1.3 sensors' resistance is reduced decreasing the oxide thickness. RA product increases by a factor of 100 increasing the MgO barrier thickness from 0.9 nm to 2nm. This change is quantitatively consistent with the values found in the literature [88], [51], revealing a good quality of the barrier and a good control over the MgO thickness.

In the table 5.4 the RA product and the corresponding error bar are showed for the three values of the barrier thickness (the RA values are obtained averaging the samples with the same value of the barrier thickness). In particular error bars of ±16% and ±10.4% are found for 2nm and 1.23 nm thick MgO, while a higher variability, ±29%, is found with 0.9 nm. Indeed all the samples, except for sample 7, show RA values that are approximately

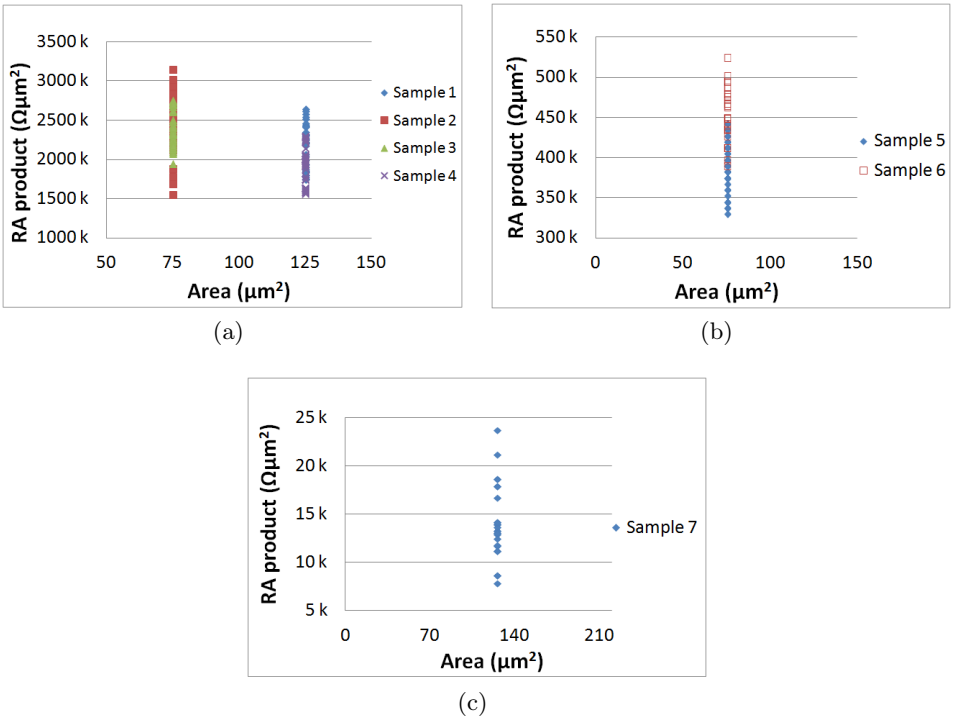

Figure 5.7: RA product versus junction area for Samples (a) 1, 2, 3, 4 (all with 2nm thick MgO) (b) 5, 6 (with 1.23nm thick MgO) (c) 7 (0.9nm thick MgO).

constant with the junction area (see panel a and b of figure 5.7). A part from the error bars coming from the intrinsic variability of measurements performed on different devices, this result demonstrates the reproducibility of the lithographic process and an improvement with respect to previous works, in which higher variability ($\approx \pm 30\%$) was obtained varying the MgO thickness from 1.5 nm to 2 nm [5]. This is a proof that the aforementioned problems of edge effects and current disuniformity have been overcome by the use of the new contacts and area dimension.

Regarding the variability of sample 7 (fig. 5.7 (c)), it can be ascribed to the very thin thickness of MgO that can lead to defects and pinning sites inside the barrier causing a not uniform flow of current. Indeed this assumption is in agreement with the roughness value found after the optimization for Sample R4 (table 5.1): 2nm of MgO, grown on 1000 nm of SiO_2 (which is the same substrate of sample 7), showed R_{rms}= 0.82 nm. Although this roughness value is overestimated, it remains comparable to the MgO thickness of the

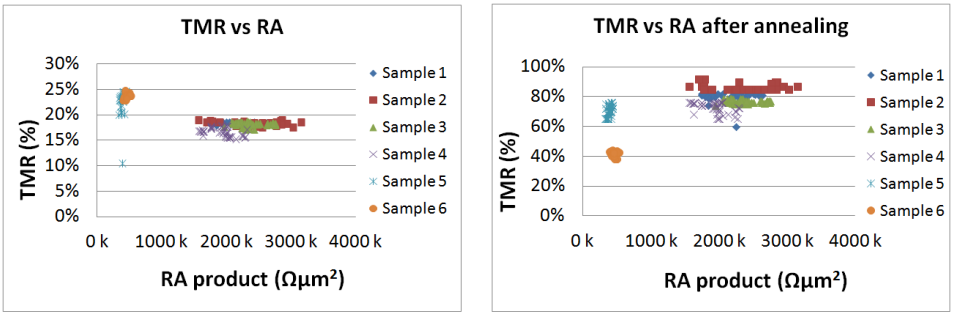

(a)

(b)

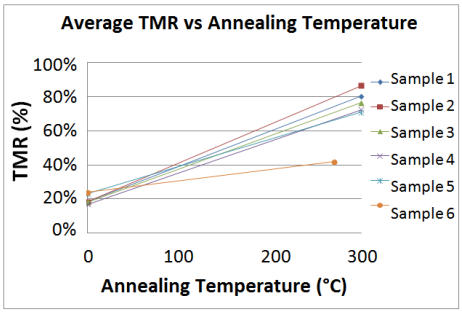

(c)

Figure 5.8: TMR ratios as a function of RA product for as-deposited Samples 1, 2, 3, 4, 5, 6 (a) and after annealing (all samples annealed at 300 °C except for Sample 6 annealed at 270 °C). (c) Average TMR ratios with the annealing temperature.

sample 7. Despite higher statistic with different junction areas is needed, from this finding is clear that too small thicknesses of MgO are limited by the surface roughness at the interface, worsening the quality of the barrier and the reproducibility of the devices.

TMR curves

Almost all of the junctions show a magnetoresistive behavior, even those with resistance lower than the nominal one due to the presence of parallel conductive channel, as discussed in the next paragraph. In figure 5.8 (a) and (b) the TMR ratios for all samples (except for sample 7) are plotted as a function of RA product before and after annealing. First of all it is worth to notice that in both the panels, the TMR is quite constant for all RA values, indicating that the lithographic process does not introduce any problem or

artifact. Moreover, as discussed in the next paragraph, this is a proof of the uniform distribution of the current through the junction area, due to the optimized design of the contacts. Secondly, one expects that a decrease of MgO thickness should lead to lower TMR values, due to the fact that a thinner barrier is more influenced by the surface roughness, and presents a lower crystalline quality with more defects and pinholes. However, this trend is only slightly visible in panel 5.8 (b), with the slightly higher TMR values of samples 1, 2, 3 (2nm of MgO), respect to samples 5 (MgO=1.23nm). However this difference is almost included in the scattering of the values visible in the plot. Morover an opposite trend is shown in the as-deposited samples, in figure 5.8 (a), due to the measurement uncertainty introduced by the use of two different experimental setup with different electronic equipment.
Finally, a comparison between graph (a) and (b) reveals a slightly increase of the scattering of the TMR values after the annealing. Apart from sample 6 which is annealed at lower temperature (see panel c in fig. 5.8), this higher dispersion can be attributed to some temperature gradient presents on the sample surface during the annealing process.
From figure 5.8 (c) which presents the average TMR value as a function of the annealing temperature for all the samples, one can evince that, as expected, the annealing procedure enhances the TMR because of the improvement in the stack crystallization and consequentely in the coherent tunneling. Indeed an increasing from about 20% to 80% is evident.
All samples have been annealed at 300 °C except for the sample 6 annealed at 270 °C. In this case a lower annealing temperature was chosen because it is expected that a lower MgO thickness require less energy (and hence lower temperature) to crystallize, and because 270 °C was selected to maximize the SAF. However, this has led to TMR values limited to 40% respect with $70 - 80\%$ of sample 5 annealed at 300 °C, as it can be seen in figure 5.8 (b) and (c). Therefore, although the optimum temperature for the bilinear coupling results to be 270 °C, it is preferable to reach the temperature of 300 °C because it is a good compromise between the magnetic stability of the bottom electrode and a high crystalline quality of the barrier, leading to high values of TMR. This is even more critical with thicker barriers.
Moreover this choice does not affect the shape of the hysteresis loops in terms of coercivity and stray field, as shown in figure 5.10, from which no substantial difference between the samples emerges.

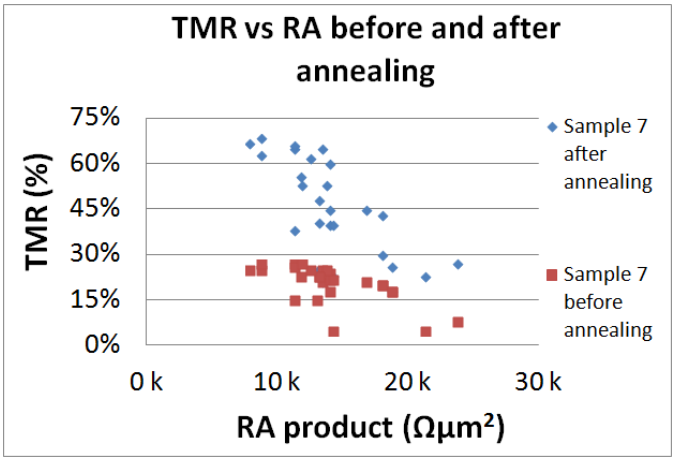

Figure 5.9: TMR ratios as a function of RA product for Sample 7 before (red squares) and after (blue squares) annealing at 300 °C.

Regarding sample 7, the TMR ratios for all the junctions are showed in figure 5.9 as a function of RA, before and after the annealing. For the previous considerations we have decided to anneal also this thinner sample at 300 °C. Even in this case the annealing enhances the TMR ratio.
As expected the variability in the junctions' resistance is transferred to the TMR values that vary from 5% to 28% in the as-deposited samples, and from 20% to 66% with annealing.
To conclude, while the thickness of the barrier does not affect the TMR values from thickness ranging from 2 to 1.2 nm, in this case of 0.9 nm the defects and corrugation of the barrier play a major role in determining the magnetoresistive behavior. It is worth to note that lower TMR values, are compansated even if not totally, at least partially, by the low noise of these devices as will e shown in the next section.

Regarding the R(H) behaviour, in figure 5.10 and 5.11 the TMR loops of the most rapresentative junction for each sample, are reported. All the fabricated devices have the characteristics of sensors: the transfer curves have an almost linear shape, and, even in the case of unbalanced SAF (Samples 1-6) the bottom layer is pinned in a quite large magnetic field range.
All the junctions in fig. 5.10 show a coercive field $H_c \approx 10Oe$ and all loops result to be shifted of about 40 Oe respect to the origin of the magnetic

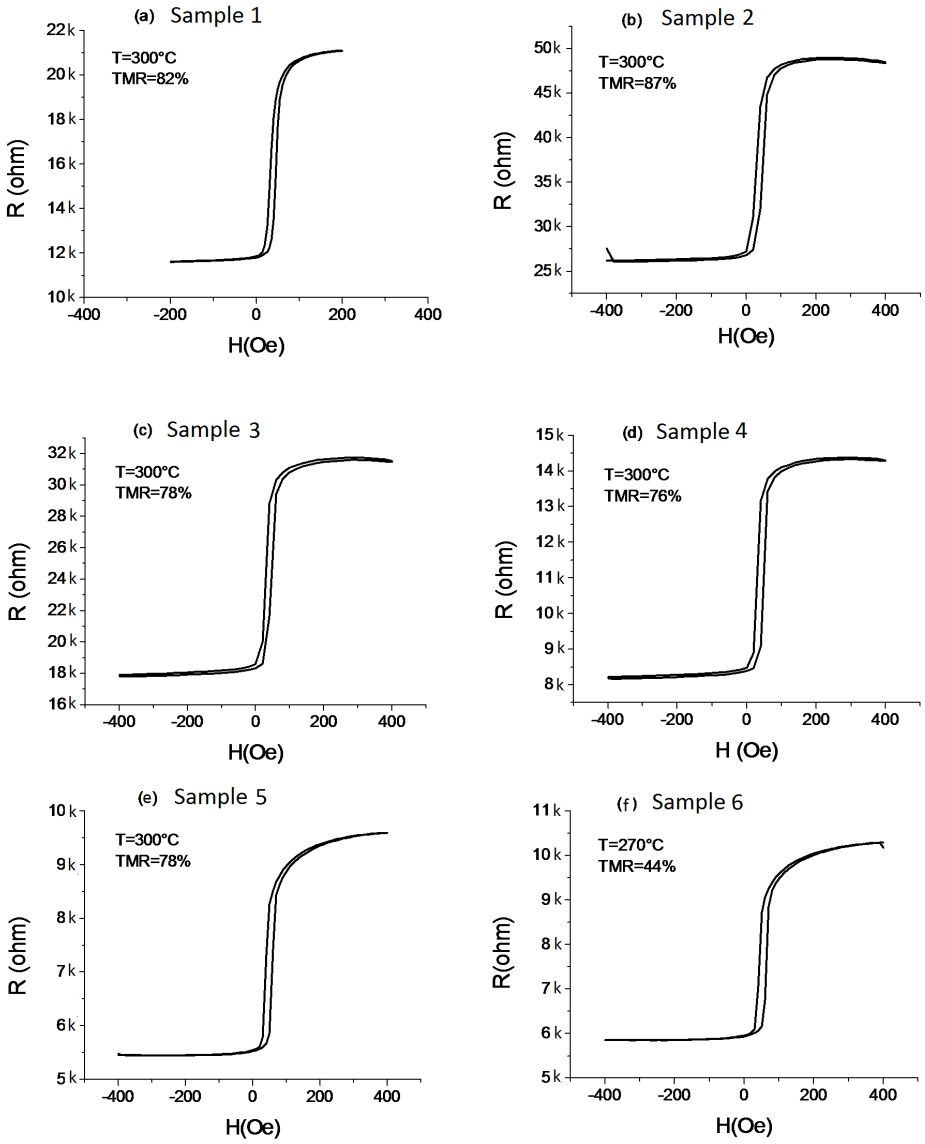

Figure 5.10: TMR loops of the junctions which provided the highest TMR values: (a) Sample 1 (b) Sample 2 (c) Sample 3 (d) Sample 4 (e) Sample 5 (f) Sample 6.

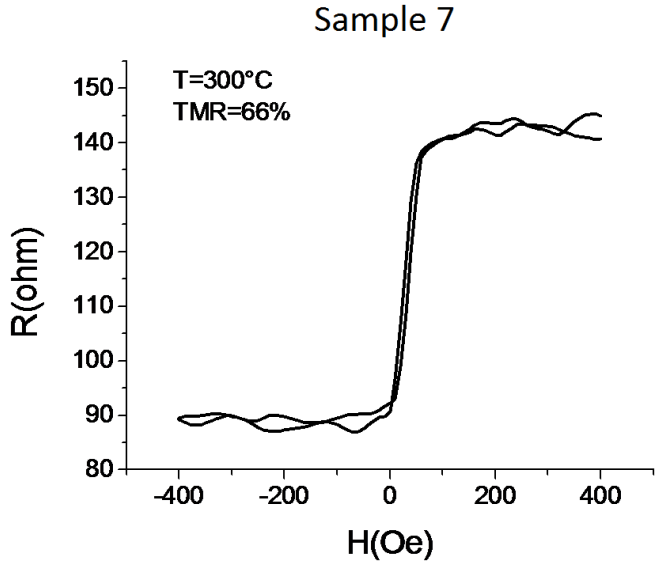

Figure 5.11: TMR loops of the most performing junction of sample 7 in terms of coercivity and reduced stray field.

field axis. As about the residual hysteresis which compromises the ideal linearity of the curves many aspects could be taken into account. First of all, a non-perfect superparamagnetic condition of the FeCoB free layer due to some uncertainty in the calibration of the thickness (the transition between ferromagnetism and superparamagnetism happens in few angstrom). Secondly, the roughness of such thin barriers could induce a magnetic coupling between pinned and free layer, e.g. Néel coupling. Moreover, some non-idealities can be introduced during the fabrication process, making the condition of crossed anisotropy not perfectly verified. For example during the first step of lithography the short side of the junctions could not be perfectly aligned with the direction of the exchange bias, or the annealing procedure could be performed with the magnetic field slightly misaligned respect to the exchange bias direction. Finally, the stray field induced by an unbalanced SAF may cause a magnetic coupling between pinned and free layer.
The not centered curves can be also attributable to the extra stray field due to the not optimized SAF structure. Only samples 7 has been grown with the right thicknesses of CoFe and CoFeB for the balanced SAF structure (see table 5.3). Indeed the best result concerning minimization of the stray field

is obtained in sample 7.
Figure 5.11 shows the hysteresis loop of one of the best performing sensors of sample 7. It shows a TMR of about 66%, a coercivity of 4 Oe and a shift of 28 Oe. In this case the reduction of the shift can be due to the balanced SAF (H_x=4000 Oe, sample S3 in fig. 5.6) that ensures the pinning of the bottom CoFeB. Moreover the decrease of the stray field seems to have reduced the hysteresis of the free layer. Indeed, from the inspection of the loops of fig. 5.10, which show the same coercivity for all the samples, it is clear that the misalignment problems occurring during lithography are unavoidable systematic errors. The Néel coupling due to the roughness can be even higher in sample 7 due to the low thickness of the barrier. Therefore, the good result of 4 Oe of coercivity is attributable to the balance of the SAF, which results the main cause of hysteresis. Note that 4 Oe is a good results considering that the measurement setup has a resolution of 1-2 Oe due to the electromagnet hysteresis.

Fabrication Yield

As explained in the previous paragraph, even if some efforts have to be done in order to improve the crystalline quality of the sensors when thin barries are used (less than 1 nm), during this thesis some important results have been obtained regarding the repetatibility of the sensors. A direct proof of this improvement is the high fabrication yield obtained, i.e. the number of working sensors devided by the total, that has been on average of about 83% within each sample, with a very low deviation from this medium value of 0.24%. Another important aspect to be considered, as an indication of the repeatability and reliability of our sensors, is the low variability of the TMR ratio obtained within each sample, compared to previous works of this group [5]. To confirm this assumption in figure 5.12 the TMR loops of the sensors used for the experiments of molecular recognition of synthetic DNA (see next chapter) are shown. Before performing the experiment all the sensors have been characterized, obtaining 5/8 working sensors and a great repeatability of the hysteresis loops, that show very similar shapes with only a slight variation of the TMR ratio ($\approx 3.6\%$), attributable to the disuniformities of the magnetic field produced by the electromagnet. It is worth to note that in this case the non working sensors are junctions damaged during the functionalization procedure, which consists of thermal treatments in

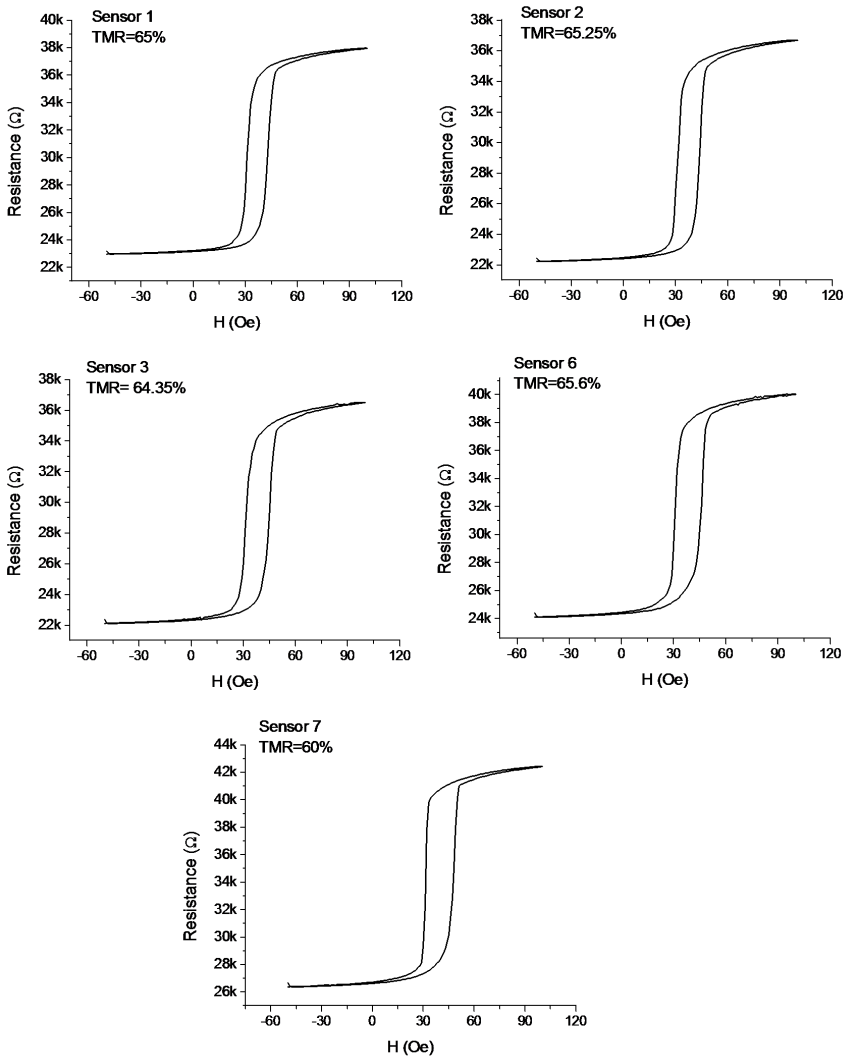

Figure 5.12: TMR loops of the sensors of sample 4 enabled for the experiment of molecular recognition (COCU).

humid/saline ambient leading to a damage of the contacts/barrier even in presence of capping layers (see chap. 6).

The small percentage of non-working samples obatined during this thesis work, and the resistance variation from its nominal value, are attributable to different causes. First of all at critical thicknesses of the insulating barrier, or at big junction areas, pinholes or defects can form resulting in ballistic

electrical conduction instead of tunneling. Moreover, reduced contact area can cause disuniformity and edge effects in the current flow, causing a reduction of the sensor resistance. As previously discussed, important efforts have been done to overcome, at least partially, these two problems, thanks to the use of bigger contacts and smaller junction area. Other causes can be instead found in the lithographic process. Indeed, despite all the phases and the parameters of the process are carefully optimized, some errors can be possible, compromising the sensors functionality. For example an insufficient etching procedure, or a detachment of the deposited SiO_2 from the sample due to a prolonged ultrasounds treatment, can cause shortcuts between top and bottom layer, resulting in a drop of the resistance. Otherwise a prolonged etching procedure can increase the sensor resistance, or residual photoresist, remained attached to the junctions after the lift off procedure, can isolate the FeCoB layer from the top electrode, increasing dramatically the sensor resistance.
In this context the future perspectives are related with a better control of the various step of the lithographic process.

5.3 Noise vs MgO thickness

Noise measurements in magnetic tunnel junctions are important since they indicate the ultimate field resolution that can be achieved at any particular frequency. Noise in MTJs can be associated to various mechanism, in particular the main contributions are shot noise at nonzero bias currents, thermal or Johnson-Nyquist noise at zero bias currents, and 1/f noise (nonmagnetic 1/f noise and magnetic 1/f noise). The 1/f noise manifests itself as resistance fluctuations in the low frequency range, while the magnetic noise is produced by magnetization oscillations [98] [8] [45].

The noise measurements have been performed at the department of Electronics and Information of Politecnico di Milano by the research group led by Marco Sampietro. The instrumental setup used for the measurements has been previously described in chapter 3 (see paragraph 3.2.5).
In order to study any significant differences sample 1 and sample 7 of tab. 5.3 have been chosen for the noise measurements. For an immediate visualiza-

Sample	t_{MgO} (nm)	t_{SiO_2} (nm)	RA product ($k\Omega\mu m^2$)	TMR ratio
1	2	100	1750	82%
7	0.9	1000	16.75	66%

Table 5.5: Summary of sample 1 and sample 7.

tion the characteristics of the two samples have been reported here in the table 5.5.
Because of the different thickness of MgO and because the two samples have been grown on different substrates, we expect to observe eventual differences. In the next paragraphs the noise spectrum of one junction for each sample is reported. The other junctions of each chip do not present any significant differences, so they are not reported in this work.
First, the measurements have been carried out withouth applying magnetic field, than, in the second sample, for a direct comparison with the literature, the measurement is repeated with the operating point in the linear region of the transfer curve by applying a non zero magnetic field, created with external permanent magnets. Indeed, observing the figure 5.10, it can be seen that, as an effect of the shifted hysteresis loops, at zero applied field the magnetization is very close to saturation. This is a situation of equilibrium for the spins which definitely is not affected by magnetic noise that in general is due to magnetic fluctuations. This situation is comparable to that of our molecular recognition experiments that, as explained in section 3.3, are performed with the operation point in the non-linear zone of the R(H) curve. Indeed, the most performant characterizations have been carried out by this group at zero field, which appears to be one of the possible operating points.

Noise spectra of Sample 1

In figure 5.13 (a) the noise spectra of the sample are showed. The noise spectra are measured and analyzed varying the current flowing through the sensor, from 0 to $8\mu A$. To understand the obtained data, three types of noise have been considered, for each one the power spectral density is showed:

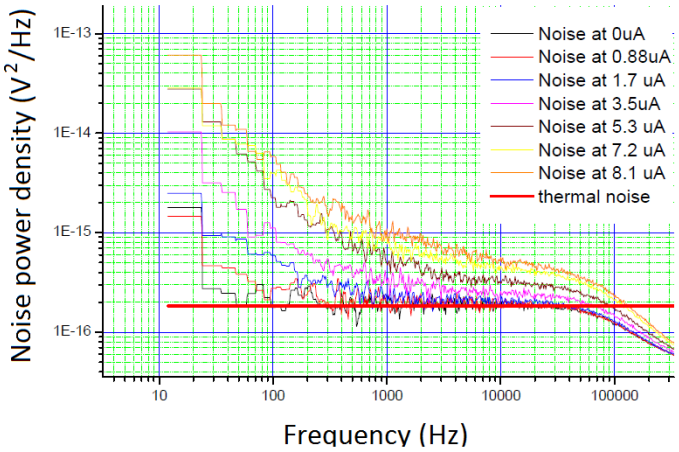

(a)

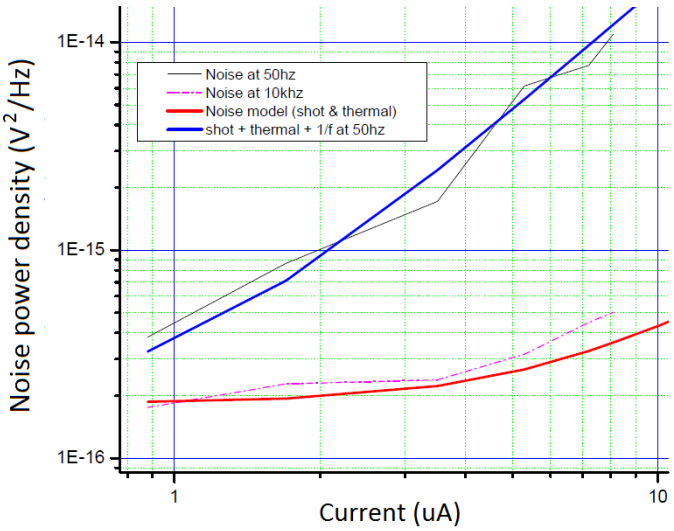

(b)

Figure 5.13: (a) Noise power density V^2/Hz varying the current flowing through one sensor of Sample 1. All the other sensors are kept to ground; (b) Noise power density V^2/Hz, as a function of the current, measured at two different frequencies, 50 Hz and 10 kHz.

1. Thermal noise: $P_{noise}/Hz = 4K_bTR$;
2. Shot noise: $P_{noise}/Hz = 2qI$;
3. 1/f noise: $P_{noise}/Hz = kI^2/f$.

The presence of the shot noise is evident in fig. 5.13 (a), where the noise, once exhausted the 1/f noise, leans towards different asymptotic levels as a function of the current.
In figure 5.13 (b) the noise spectrum as a function of the current, for two different frequencies (50 Hz and 10 kHz), is shown. While the thermal noise contribution is dominant around I = 0, at finite bias the increasing in noise indicates the crossover from the thermal to the shot noise. Indeed at higher frequencies the noise fits with the theoretical model which includes contributions of both thermal and shot noise (see section 2.4, equation 2.20). At lower frequencies the results obtained are in agreement with the 1/f noise, which would impose a quadratic dependence from the current.
In fig. 5.13 (a) a capacitive effect at about 90 kHz can be noted. The origin of this limit has been attributed to capacitive parasitism between the gold paths and the substrate. In figure 5.14 (a) a simplified model of the single sensor is represented. The Si substrate can be modelized with a resistance of about 2 kΩ (resistivity of $\rho = 10$ Ω·cm and a substrate depth of 300 μm), while the SiO_2 can be modelized with a capacitance of about 270 pF. This situation is equivalent to an impedance that corresponds to the parallel between the sensor resistance R_{sens} and $[C_{par}/2+R_{si}]$. The evaluation of the

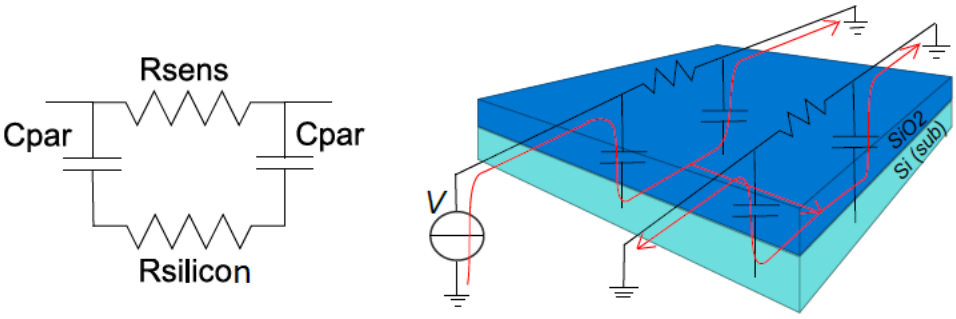

(a) (b)

Figure 5.14: (a) Simplified model of the single sensor with the parasitic capacitances (C_{par}) and the substrate resistance ($R_{silicon}$). (b) Simplified model of a chip with only two sensors that have a common substrate.

pole of the single sensor would indicate a frequency of about 90 kHz:

$$f_p = \frac{1}{2\pi(R_{sens} + R_{si})C_{par}/2} \approx 90\ kHz. \tag{5.3}$$

This results seems to be in perfect agreement with experiments. One has to mention that the spectra of figure 5.13 (a) have been measured keeping all the other sensors to ground. In this case, since all the sensors have a common substrate (fig. 5.14(b)), their parasitic capacitances also contribute to the overall impedance resulting in a lower frequency pole. This disagreement has been attributed to the rough estimation of the parasitic capacitance and of silicon resistance.

For most applications, in particular for biological studies, it is important to work in a frequency region where the noise associated is stable and minimum. In addition, working at high frequencies increases the effect of the ionic currents within the solution, where the magnetic beads are dispersed, on the sensor output signal. This gives rise to spurious effects independet from the magnetism of the beads but related only to the conductibility of the medium flowing over the sensors, thus affecting the reliability of the measurement. For this reason it is necessary to move the corner frequency of the 1/f noise at a frequency that should be as low as possible
Moreover in this case it would be preferable to shift the pole due to the parasitic capacitance of the substrate towards higher frequency, in order to have a "flat" response of the sensor as a function of the frequency. For this reason Sample 7 (see table 5.5) has been grown on 1000 nm of SiO_2. In this case, referring to the simple model presented before, the SiO_2 substrate can be modelized with a parasitic capacitance C_{par} an order of magnitude lower than in the case of sample 1. This fact, combined with the reduced thickess of the barrier (that leads to a lower sensor resistance R_{sens}), could act positively on the pole moving it towards higher frequencies (see equation 5.3). Moreover a low resistance can reduce the 1/f noise, which is the most critical in case of MTJ.
Indeed better results are obtained in the noise measurements of the next sample.

Noise spectra of Sample 7

In figure 5.15 (a) the noise spectra of the sample are showed. In this case, because of the low resistance of the junctions ($R_{sens} \approx 90\Omega$) the noise spectra

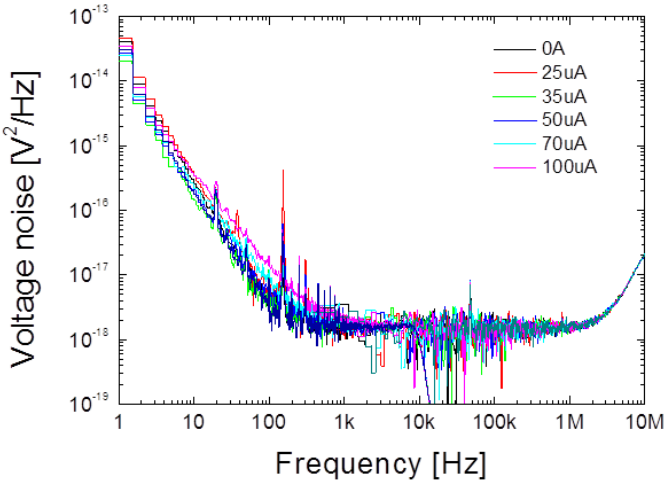

(a)

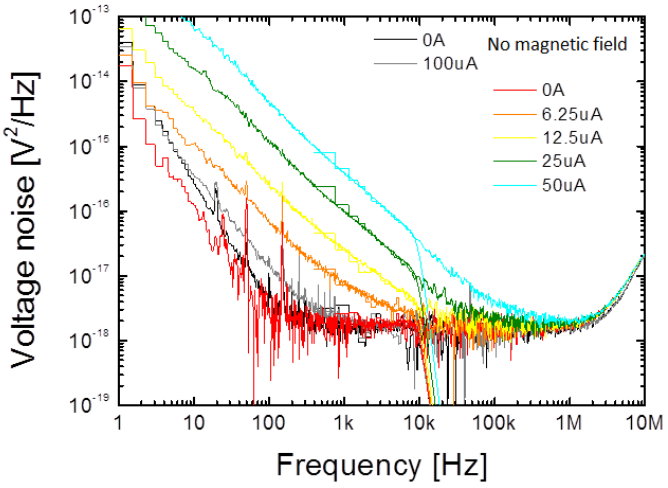

(b)

Figure 5.15: Noise power density V^2/Hz varying the current flowing through Sample 7: (a) withouth applying magnetic field and (b) applying magnetic field (linear region of the transfer curve). For a direct comparisong the cases of 0 and 100μA in absence of magnetic field have been shown (black and gray curves).

have been measured with a maximum voltage of 10mV to avoid possible damages of the device. The current flowing through the sensor has been varied from 0 to 100μA. Using these low voltages, extracting information about the shot noise results more difficult, because it would require voltages higher than $2K_bT/q \approx 50$mV to clearly manifest itself.
For each set of measurements it is possible to observe an instrumental noise at low frequencies, as can be noted observing the spectrum at zero current (in this condition the spectrum must be flat, and any changes in the frequency is attributable to the instrument) and at high frequencies, as can be noted observing the anomalous increase of the noise above 1MHz.
There are three main improvements respect with the case of the previous sample:

1. Because of the low resistance, the thermal noise has been reduced by about two orders of magnitude, from about $5 \cdot 10^{-16}$ V^2/Hz to about $5 \cdot 10^{-18}$ V^2/Hz;

2. The corner frequency of the 1/f noise has shifted from about 1000 Hz to about 100 Hz. This is a very good result, considering that the measure has been carried out at higher currents than in the case of sample 1, and that during the experiments of molecular recognition we work at a frequency of 1.14 kHz (see section 3.3), that is an order of magnitude higher than this corner frequency.

3. The capacitive parasitism has disappeared: this is certainly due to the lower junction resistance and to the thicker substrate.

This is a good result compared to other works in literature. For example similar results have been obtained in [35] by Freitas et al. In [81] a higher 1/f contribution has been measured in a range of 100 and 1000 Hz for MgO-based tunnel junctions with a comparable resistance, in the state of parallel magnetizations between free and pinned layer.
In figure 5.15 (b) the preliminary results concerning noise spectra under applied magnetic field are shown.
The effect of the magnetic field is definitely clear in particular on the corner frequency of the 1/f noise that has shifted dramatically towards higher frequencies, in agreement with other works [45], [35]. Moreover in this case the presence of shot noise is more visible, even if still weak: once exhausted

the 1/f noise, the white noise leans on different levels as a function of the current. According to [98] and [8], the dramatic increase of noise has a magnetic origin, due to the fact that the external magnetic field has changed the magnetic configuration of the sensor, leading to a midway condition between the two saturations. This is probably a more instable magnetic configuration, which leads to an extra magnetic noise.
It is worth to notice that the presence of the static magnetic field does not contribute to an increase of the noise background of the instrumentation, as checked by measurements on reference non-magnetic samples. However, more work has to be done in order to disentangle the noise contribution arising from the intrinsic magnetic configuration of the sample, and those arising from some instabilities of the experimental setup that can influence the sample behaviour (i.e. some mechanical vibration of the permanent magnet located under the sample and generating the magnetic field).
Despite the worsening observed in the latter measure, attributed to the reasons described above, the results obtained can be considered satisfactory. Indeed during the experiments of molecular recognition, the working point is set in condition of negligible magnetic noise, as in the case of the first measure performed for this sample, which displays a "flat" response of the sensor as a function of the frequency, and a 1/f noise with a quite low frequency corner (around 100 Hz). This is an important achievement in view of the realization of the platform of chapter 4, which will consists of several elements each contributing with its intrinsic noise level.

5.4 Summary

In the course of this work, significant achievements have been obtained, demonstrating the applicability of our sensors to the biological system of chapter 4. The main purpose of the work presented in this chapter can be summarized in the following points:

1. Improving the current state of the art of the MTJ sensors fabricated at LNESS reducing the coercivity and the stray field of the hysteresis loops.

2. Showing that the reliability and the repeatability of the sensors can be improved using smaller junctions and bigger contacts.

3. Reducing the MgO thikness, maintaining its high quality, in order to obtain a reduced resistance and consequenly a reduced noise.

In the first section the optimization of the sensor stack, starting from the most critical aspects of a TMR junction, has been carried out. First of all an optimization of the substrate roughness has been performed in order to ensure good quality of the MgO barrier inside the junction stack. A roughness of about 0.7 nm rms has been obtained on a sample of 2 nm thick MgO grown on a SiO_2 substrate of 100 nm. Then, after studying the exchange bias at the IrMn/CoFe interface, the pinning of the bottom ferromagnetic layer has been improved optimizing the SAF structure, in terms of its stability and balance. Good achievements have been reached with respect to the initial condition: a strong exchange coupling has been measured, with a loops separation of about 4000 Oe, and a better, even if not complete, compensation of the magnetizations of CoFe and CoFeB layers.
In the second part of the chapter the characterization of the various sensors fabricated at LNESS has been carried out. The most important result obtained concerns with the repeatability and reliability of the sensors, in terms of RA product, hysteresis loops and TMR ratios, overcoming the problems of edge effects and current disuniformity thanks to the use of smaller junction area with bigger contacts. On the other hand, sensors with thin MgO thickness (down to 1nm) are found to be limited by the surface roughness at interface. For this reason the future perspectives are related to the improvement of the quality of thin MgO film. In addition another important result corncerns with the reduction of the coercivity and the stray field of the hysteresis loops, attributed to the use of the balance SAF structure.
Finally, in the last section the noise measurements performed on two samples have been presented. As expected, a big improvement has been obtained reducing the MgO thickness from 2 to 0.9 nm: the thermal noise is reduced ($\approx 10^{-18}$ V^2/Hz), the corner frequency of the 1/f noise has shifter towards lower frequency ($\approx$ 100 Hz) and a flat response of the sensor as a function of the frequncy is obtained. These can be considered important achievements for biological applications, and also with respect to the actual state of the art.

Chapter 6

Biological experiments

This final chapter describes the most important result of this thesis work, which concerns the biological experiments. During this work, an experiment of molecular recognition of pathogen DNA, the HEV virus, has been successfully completed. This is a remarkable achievement for our research group, since, after the first hybridization assays with synthetic DNA, the operation of the devices fabricated at LNESS has been tested on natural DNA for the first time.

6.1 Study of bio-functionalized surfaces labeled with magnetic nanospheres

Before starting with the biomolecular recognition experiments with the magnetoresistive sensors, hybridization tests have been performed in order to find the best assay conditions. For this reason, this section deals with the study of surfaces functionalized with 3 different types of pathogen DNA: Enterobacter, HEV virus and Aureus. As previously explained in chapter 4, in this project all the functionalities required for the bioassay will be integrated in the platform, including the hybridization between the probe and the amplified target DNA, that will take place in a controlled microfluidic environment. For this reason it is important, for the success of the experiment, that the whole process runs under well controlled and optimized conditions. In this context, the study carried out in this paragraph has allowed to test different important aspects of an experiment of molecular recognition: the amplification of the target DNA by means of PCR, the hybridization process

between probe and target DNA, and the binding between biotinylated DNA and streptavidin-coated magnetic beads. The first is an important aspect to keep into account during an experiment of biomolecular recognition because affects the binding signal ΔS_H which is directly related to the concentration of target DNA.

The samples under test, consisting of silicon substrates, have been functionalized with the following procedure:

- First the surface has been coated with a functional copolymer, named copoly (DMA-NAS-MAPS), which provides reactive groups suitable for immobilization of the probe molecules and, at the same time, prevents non specific adsorption of biological fluids components.
- Then the oligonucleotides specific for the particular pathogen (modified with an amine group, which covalently binds the oligonucleotides to the surface) have been spotted on the sample.
- Then a blocking buffer (ethanolamine, 50mM in a Tris/HCl buffer 0.1 M, 50 °C) has been used to prevent nonspecific binding during the subsequent hybridization step.
- Biotinylated target DNA has been amplified by means of PCR, and then placed above the surface for the hybridization. This process first requires the denaturation of the amplified DNA, i.e. the separation of the single strands, at a temperature of 95 °C, and then the hybridization at a temperature of 40 °C.
- The sample has been incubated with streptavidin-coated magnetic beads (Micromod Nanomag-D, diameter of 250 nm, and a core of 75-80% magnetite in a shell of dextran) to allow the reaction biotin-streptavidin with the target DNA.
- At the end of the procedure the sample has been washed to remove the unbound beads.

First of all, a typical experiment with fluorescent detection has been performed in order to compare the results obtained with the hybridization of the magnetic beads with a well established technique. Then the samples surface has been observed with optical microscope and checked with AFM,

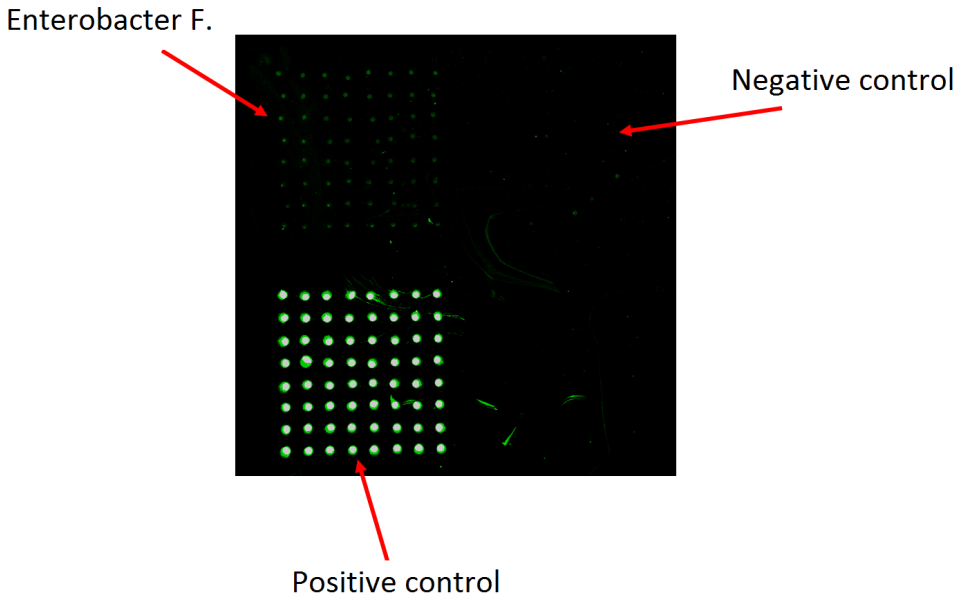

Figure 6.1: Fluorescence image of the sample spotted with Enterobacter faecalis. The bottom left part of the image, and the top right, show respectively the positive and negative control of the sample.

in order to get image of its profile in corrispondence of the DNA spots, where clusters of beads are supposed to be found if the binding between biotin and streptavidin correctly occurs. All the AFM measurements have been performed using our Veeco Innova system, scanning a sample area of $100\mu m^2$ in tapping mode.

The first sample under test has been functionalized with Enterobacter faecalis, a bacterium inhabiting the gastrointestinal tracts of humans and other mammals, which can cause life-threatening infections [94]. The concentration of the probe DNA is 20 μM, while that of the amplified target DNA is 7 ng/μL, corresponding to 210 nM.

The sample has been provided with positive and negative controls to check the binding reaction between biotin and streptavidin. The positive control is the biotinylated target DNA, while the negative control is the probe DNA. The sample is then incubated with Cy3-streptavidin (cyanine3 is a dye which fluoresces yellow-green). The fluorescence image in figure 6.1 shows very bright spots for the positive control and, in contrast, no fluorescence for the negative control, indicating that the binding between biotin and streptavidin

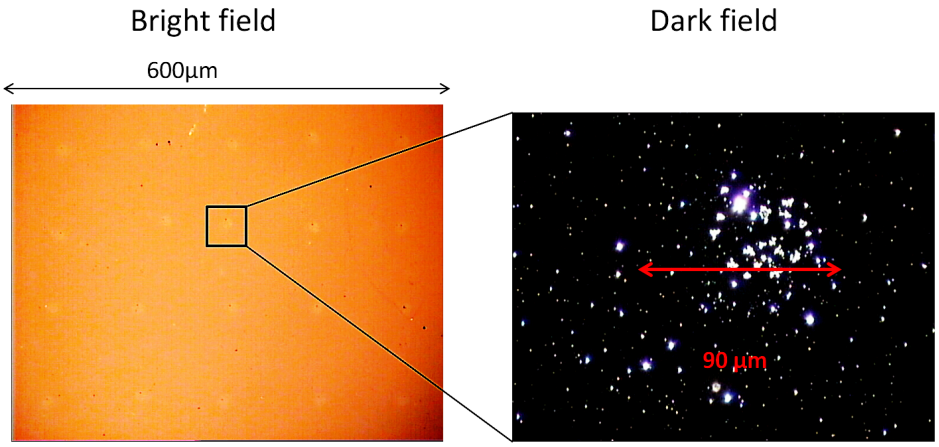

Figure 6.2: Optical microscope images of the DNA spots (Enterobacter F.). The figure on the left shows a bright field image of the sample and figure on the right a dark field image of a single spot.

successfully occurs. However, the optical images of the sample (figure 6.2) show that the spots, having a diameter of about 90 μm, are not well defined and visible neither in bright field nor in dark field, and do not have a clearly defined shape and boundary.

To better understand if the hybridization has worked, an AFM image of the sample hybridized with enterobacter has been acquired. The AFM image shows, inside the hybridizated spots, only few bright features having height of about 50 nm (figure 6.3 (a)), and, outside the spots, smaller features, about 35 nm height (figures 6.3 (b)). The first ones can be attributed to fragmented nanoparticles immobilized inside the spots through the streptavidin-biotin interaction, while the latter correspond to fragments of beads remained attached to the surface also outside the spots (unspecidic bonding). The roughness inside and outside the spot are respectively 3.8nm rms and 2nm rms, in a scanning area of 100 μm^2. No clear difference between the two cases is detectable, and to exclude a failure in the hybridization with the magnetic beads through the straptividin-biotin binding, an AFM image has been acquired scannign an area of 100μm^2 in the positive control (figure 6.3 (c)). In this case it is possible to see a big concentration of nanoparticles inside the spots, having height of about 100 nm, with a roughness of about 40 nm rms in an area of 100 μm^2. Outside the spots a roughness of about 13 nm rms is measured (figure not shown).

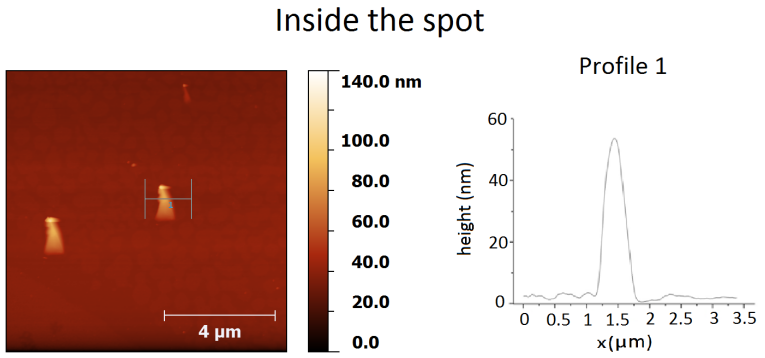

(a)

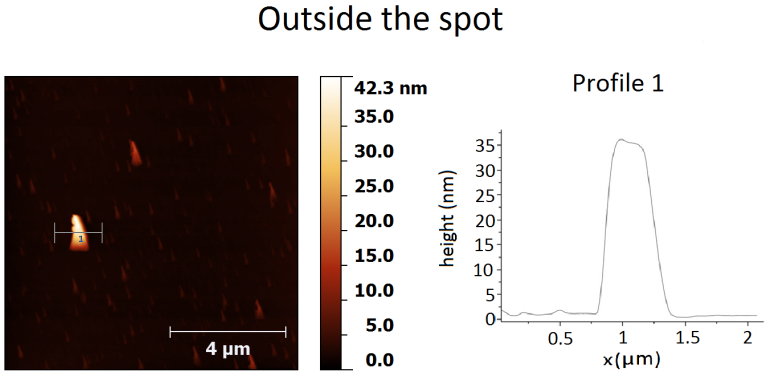

(b)

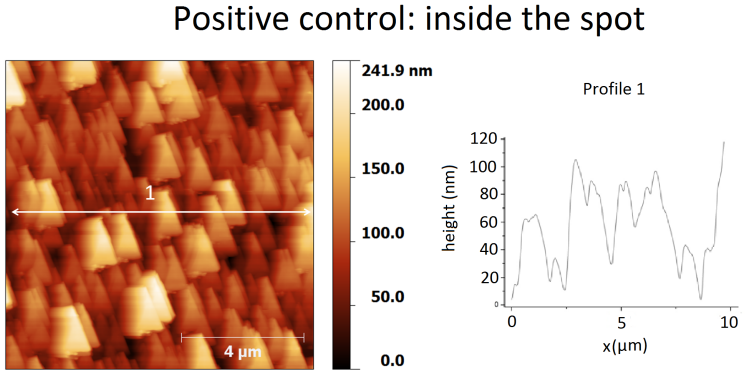

(c)

Figure 6.3: (a) AFM image of magnetic particles immobilized inside and outside (b) the spot. (c) AFM image of magnetic particles immobilized inside the spot in the positive control. The panels on the right show the height profiles measured along the white lines of the figures on the left.

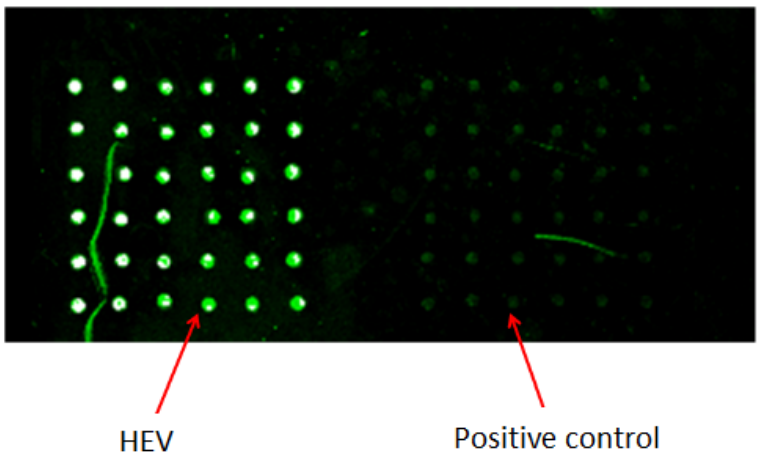

Figure 6.4: Fluorescence image of the positive control of the sample spotted with HEV.

From both the fluorescence and AFM tests it is possible to conclude that, as expected, while the biotin-strepatividin binding process in itself is not a major issue, in this case too low DNA concentration has been produced by PCR. A longer PCR process, involving a greater number of cycles, should be used to improve the efficiency of the hybridization.

Better results have been obtained in the second sample analyzed, that has been functionalized with the Hepatitis E virus (HEV), using the previously described procedure (probe DNA: 100 bp, 20 μM, amplified target DNA: 9 ng/μL corresponding to 275 nM).
Even in this case the binding reaction between biotin and streptavidin has been successfully checked with fluorescent detection, as showed by the image in figure 6.4. The fluorescent signal coming from the positive control results to be weaker compared to the same signal in the previous sample (see figure 6.1). This fact is imputed to the different positive controls used in the two samples. Indeed in the previous sample (Enterobacter) the target DNA was directly incubated with fluorescent streptavidin, while in this case the probe oligonucleotides have been first hybridized with biotinylated complementary target and finally incubated with the fluorescent streptavidin. Therefore the biotin-streptavidin binding is mediated by the hybridization between probe and target DNA, and this explains the lower fluorescent signal coming from

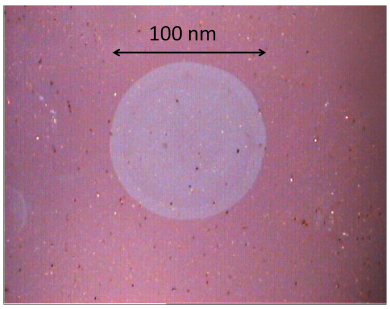

(a)

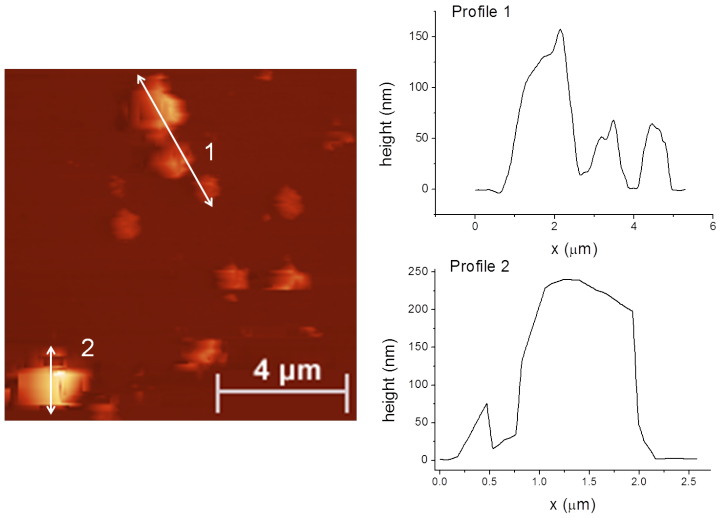

(b)

Figure 6.5: (a) Optical microscopic image of the HEV spot in bright field. (b) AFM images of magnetic particles immobilized inside the spots. The panel on the right shows the height profiles measured along the white lines of the figure on the left.

the positive control, which becomes at the same time more predictive and reliable. The optical image of the sample in figure 6.5 (a) confirms the effectiveness of the hybridization process with the magnetic beads, showing defined spots with a diameter of about 100nm. This finding is confirmed by the AFM image of the hybridized spot which shows a higher concentration of nanoparticles compared to the previous case. In panel (b) of figure 6.5 bright features are evident inside the spot, with a height ranging from about 50 to 250 nm (Roughness = 32.8 nm rms in a scanning area of $100\mu m^2$). These results can be considered a good achievement if we take into account

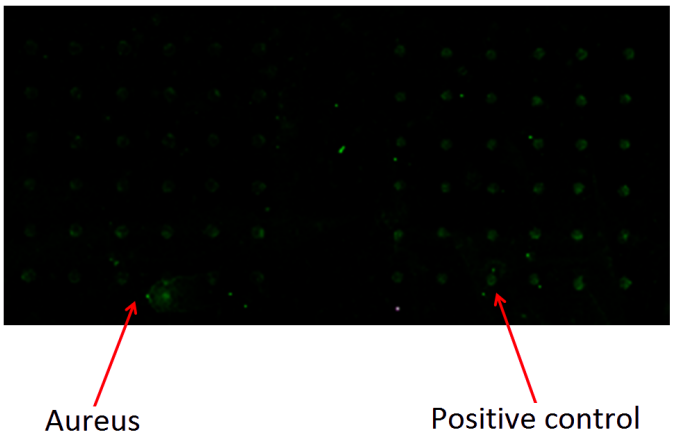

Figure 6.6: Fluorescence image of the sample spotted with Staphylococcus Aureus.

that the steric hindrance resulting from the relative dimensions of a single DNA molecule (100 bp) could be a disadvantage for the hybridization with the magnetic beads.

The last sample analyzed has been functionalized with Staphylococcus Aureus, a bacterium that is a common cause of skin infections, respiratory disease and food poisoning. The results obtained in this case are not satisfactory. The fluorescence image of the sample (fig. 6.6) shows a weak signal from the spots, indicating a poor biotin-streptavidin binding. Moreover outside the spots fragments and even agglomerates of nanoparticles are spread everywhere (figures not shown), showing the inefficiency of the washing step. The successful of the washing step is an important aspect to keep into account during an experiment of molecular recognition because the beads distribution over the sample surface is determinant for the evolution of the output signal, affecting the performances of the sensors during the biological assay. Indeed, as discussed in section 1.4, the average magnetic field generated by the beads depends drammatically on their position, and a maximum response of the sensor occurs when the beads are immobilized only over the bio-funcionalized spots, in corrispondence of the sensors area.

In conclusion, the best hybridization results have been obtained with the sample spotted with the HEV virus. For this reason the first experiment of

molecular recognition on natural DNA has been carried out with this kinf of pathogen (see section 6.2.3).

6.2 Biomolecular recognition with magnetic sensors

The instrumental apparatus and the methods used for an experiment of molecular recognition have been already described in section 3.3. In this case the post hybridization approach has been chosen and here the main phases of the bioassay are summarized (see figure 6.7):

1. First the baseline signal is acquired for each sensor until the signal gets stable.

2. Streptavidin-coated magnetic beads are injected through a syringe pump in the microfluidic cell, and, once arrived over the sensors surface, the flux is stopped till their full sedimentation.

3. After sedimentation, the beads are left to interact with the immobilized biotinilate target for 15 minutes.

4. In the last step of the experiment the sensors are washed until the control signal recovers completely its baseline.

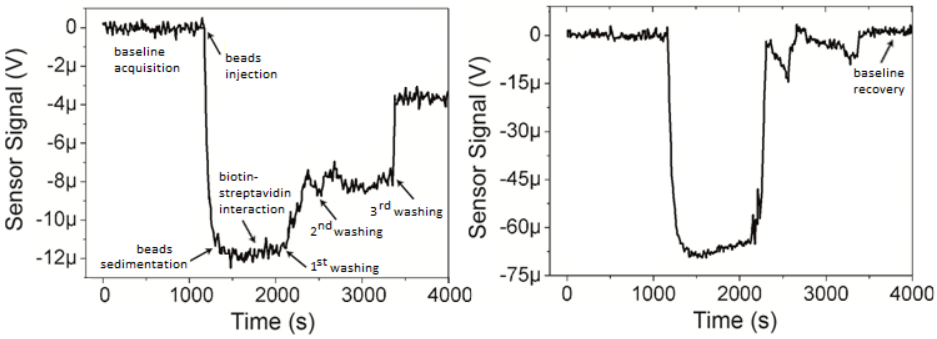

Figure 6.7: Typical experiment of molecular recognition: signal from one sensor (left panel) and from a reference (right panel) sensor [4].

Before carrying out the experiment of molecular recognition of the HEV virus, the operation in the wet enviroment of the sensors bench developed during this thesis work, and all the phases of the experiment have been

tested, from the choise of the optimum working point (see paragraph 3.3.2 for the approach used), to the washing step, that must be well optimized for the success of the experiment. For this purpose, preliminary experiments of beads detection and of molecular recognition with synthetic DNA have been performed.
All the samples under test have been capped to prevent them from damages due to the fluids dispensed during the experiments. The capping consists of the following multilayer: SiO_2(50nm)/Al_2O_3(60nm)/SiO_2 (180nm), deposited by Magnetron Sputtering. The top layer of SiO_2 also allows the adhesion of the copolymer used for the bio-functionalization of the sensors surface. The latter has been carried out in the chemical laboratory of ICRM (Chemistry Institute of Molecular Recognition).
The beads used in this work are Micromod Nanomag-D streptavidin-coated magnetic beads (having a diameter of 250 nm, and a core of 75-80% magnetite in a shell of dextran), while the washing solution of the last step consists of a phosphate buffer, 0.1 M pH 7.4 in 0.1% Tween 20.
In the next paragraphs the various experiments performed and the results obtained are described.

6.2.1 Beads detection

The device tested in this experiment is Sample2 of table 5.3. In figure 6.8 (a) the transfer curve R(H) of one sensor is reported, showing a resistance of about $25k\ \Omega$ in the low state, a tunnelling magnetoresistance of 87% and a sensitivity S = 17.3 %/mT in the linear region.

The chip containing the 8 sensors is integrated in the microfluidic cell showed in figure 3.24 and the parameters of the double modulation have been set:

- V_{in} = 50mV, modulated at frequency f_1 = 1.101kHz
- H_{AC} = 6 Oe, modulated at frequency f_2 = 39Hz
- H_{DC} = 20 Oe

In figure 6.9 the signal coming from one sensor is shown as a function of time. For the first 400 s the baseline signal is acquired in order to stabilize possible drift. Once the signal is stable, the magnetic beads, diluited in a PB-Tween solution with a concentration of 3mg/mL, is flushed at rate of 50

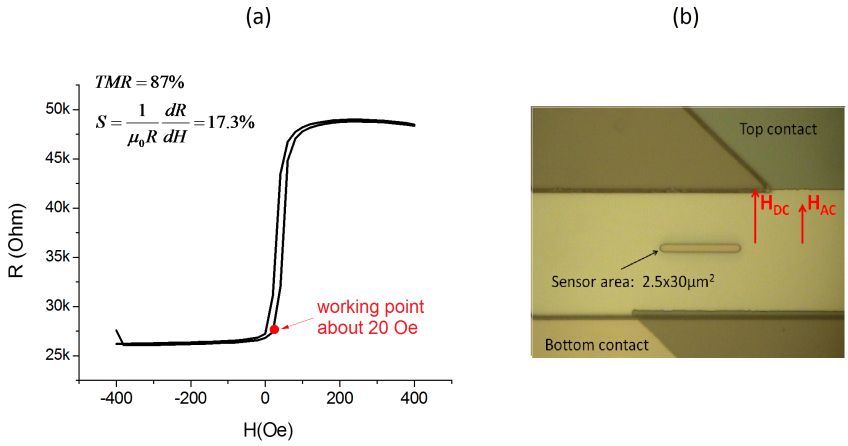

Figure 6.8: (a) Sensor response to the external magnetic field (R(H)) (Sample 2 of table 5.3) (b) Optical microscope image of the MTJ-based sensor, the sensing direction (i.e. the direction of the applied magnetic field) is shown.

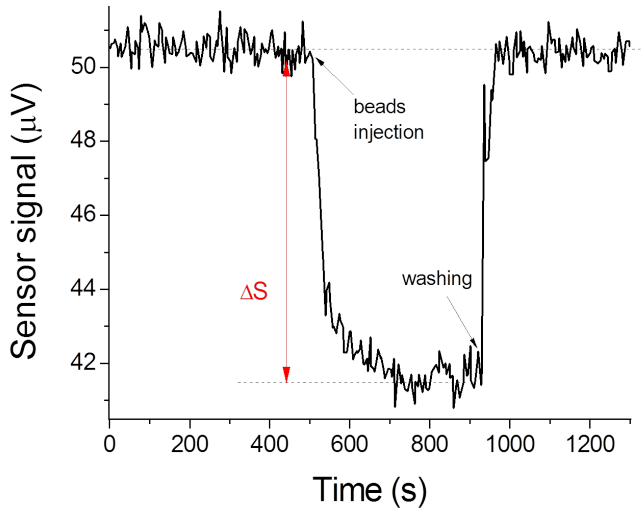

Figure 6.9: Output signal from one sensor as a function of time during the experiment of beads detection: beads injection is around t = 500 s, washing is around t = 950 s.

μL/min. No variation in the signal is visible, until when the beads reach the microfluidic cell with the sensors and a drop in the sensor signal is visible due to the beads sedimentation. At this point the syringe pump is stopped

to allow the beads sedimentation, and after 10-15 minutes, i.e. when the sensor signal is stable again, the washing solution is introduced at a rate of 450 μL/min.
The bead sedimentation is visible, with a signal variation ΔS of about 9 μV, and a signal to noise ratio $\Delta S/N \approx 28$, where the noise N has been calculated as the standard deviation of the signal baseline before sedimentation. The pronounced signal decrease during sedimentation is due to the focusing action of the stray field arising from the sensor, which attracts the beads mainly over its area, giving rise to a negative contribution to the total magnetic field sensed [3]. The little pronounced rise in the signal around t = 800 s after the sedimentation drop, is due to the bead rearrangement on the sensor surface. At the end, after only one washing step, the signal recovers completely the baseline.
Although the experiment has successfully worked, the signal arising from the beads sedimentation ΔS results to be small compared to other results obtained at LNESS by my research group [3]. This signal can be maximized essentially through the optimization of the working point and of the lock-in settings, and in the next experiments better results have been obtained.

6.2.2 Molecular recognition of synthetic DNA

A further test has been performed through the hybridization of synthetic oligonucleotides (COCU). This model system has been already used with these sensors [3], [89], [4]. This experiment has the main purpose to check the capping effectiveness in protecting the sensors during the DNA hybridization process and to calibrate the washing flows.
The device under test is Sample 4 of table 5.3. In figure 6.10, the sensor transfer curve R(H) of one sensor is reported, showing a resistance of about 11 $k\Omega$ in the low state, a tunnelling magnetoresistance of 75% and a sensitivity S = 17 %/mT in the linear region.

Before starting with the experiment the sensors surface has been functionalized with the following procedure. First the chip has been coated with the functional copolymer (DMA-NAS-MAPS) which prevents non specific adsorption of biological fluids components. Then the entire sensor area has been spotted with the biomolecules (a 23-mer synthetic oligonucleotide with the sequence 5'-NH2-GCCCACCTATAAGGTAAAAGTGA-3), which covalently bind to the functional polymer. The spotting procedure has been

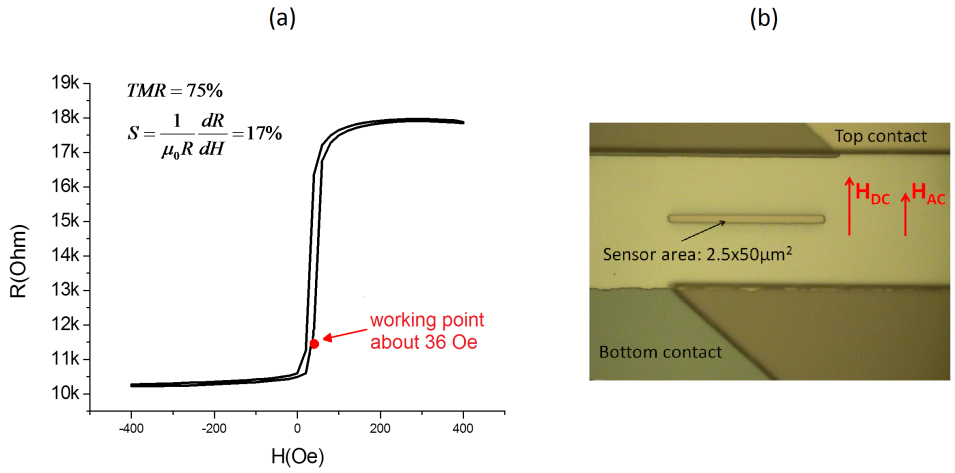

Figure 6.10: (a) Sensor response to the external magnetic field (R(H)) (Sample 4 of table 5.3). (b) Optical microscope image of the MTJ-based sensor, the sensing direction (i.e. the direction of the applied magnetic field) is shown.

performed employing a SciFlexarrayer S5 by Scienion spotter machine with an 80 μm noozle. Spot volume, temperature and humidity are 400 pL, 22 °C and 50%, respectively. To enable a positive-control study, half of the sensors (sensors 1-4 in fig. 6.12 (a)) have been spotted with a biotinylated complementary target (5'-TCACTTTTACCT TATAGGTGGGC-3', labelled with biotin at the 5' end, at 1 μM concentration), the other half with a negative control (non-complementary probe oligonucleotide, sensors 5-8 in fig. 6.12 (a)). After binding the oligonucleotides, the surface has been blocked with epoxy-polydimethylacrylamide (EPDMA), which prevents unspecific binding during the subsequent DNA hybridization phase. The DNA-DNA hybridization has been carried at room temperature in a saline-sodium citrate (SSC) buffer.

At this point the sensor chip has been integrated in the microfluidic system (figure 3.24) and the parameters of the double modulation have been set:

- V_{in} = 100mV, modulated at frequency f_1 = 1.101kHz
- H_{AC} = 7 Oe, modulated at frequency f_2 = 39Hz
- H_{DC} = 36 Oe

After acquiring the baseline signal for each sensor, the streptavidin-coated beads (3mg/mL solution of magnetic beads, diluited in PB-Tween) have been injected with a syringe pump at a rate of 50 μL/min, and stopped once the microfluidic cell has been completely filled. At this point the beads have been left to settle down, till their full sedimentation. This corresponds to a decrease in the voltage signal as shown by the signals coming from a positive and control sensors in figure 6.11 (a) and (b), respectively. After their complete sedimentation, the beads have been left to interact with the immobilized biotinilate target for about 15 minutes, and, at t=3400 s, the first washing solution has been introduced at a rate of 450 μL/min. After 200 s the flow has been accelerated up to 950μL/min, and around t = 4000 s another washing syringe has been injected at a rate of 1040μL/min.
The difference between the two baselines, before beads insertion and after the washing step, gives a signal $\Delta S_H \approx 28\mu V$. After normalizing to the sedimentation signal ΔS, the binding signal $\Delta S_H/\Delta S$ results $\approx 0.4 \pm 0.01$. This result is quite similar to that obtained in a previous work by this group (see the article [89]), in which the same concentration of synthetic DNA was used.
Despite the appreciable binding signal detected by the sensor, the optical image of the sensor after the experiment (see fig. 6.12 (c-d)) reveal low beads concentration immobilized on its surface in comparison with previous experiments performed with the same analyte concentration of 1 μM [89]. Since the synthetic DNA is the same, this can be probably ascribed to the excessive washing procedure, which has washed away also some hybridized beads. For this reason the washing of the next experiments will be performed with lower fluxes.
Regarding the control signal showed in figure 6.11 (b), it increases after the first washing up to the baseline ($t \approx 4000$ s) and then slightly decreases again. This effect has been attributed to a drift of the instrumentation. Indeed the effectiveness of the washing procedure can be proved comparing the microscope images of the control before and after the molecular recognition (see panels (e) and (f) of figure 6.12). The control appears quite clean, as proved by the color of the junction area which is the same in the two images. The slight difference between the two baselines in the control signal can be included in the limit of detection (LOD), which is defined as three times the standard deviation of the normalized signals coming from the reference

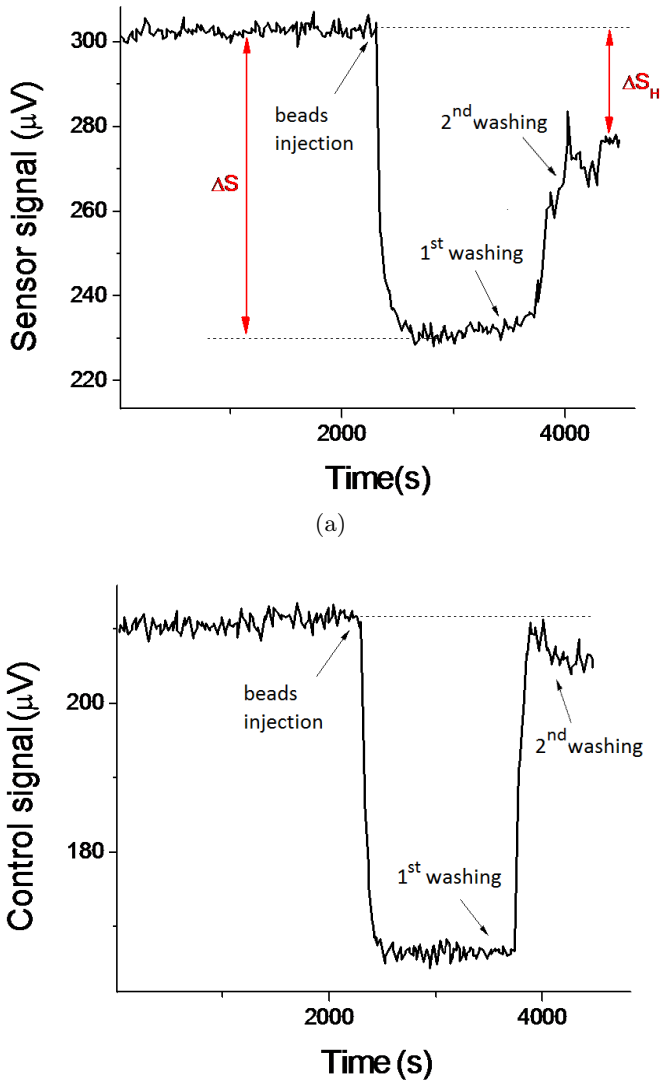

Figure 6.11: (a), (b) Sensor and control signals, respectively, as a function of time: bead injection is around t = 2200 s, the first washing is around t = 3400 s, the second around t = 4000 s.

sensors. In this case it can be easly estimated to be 0.024.

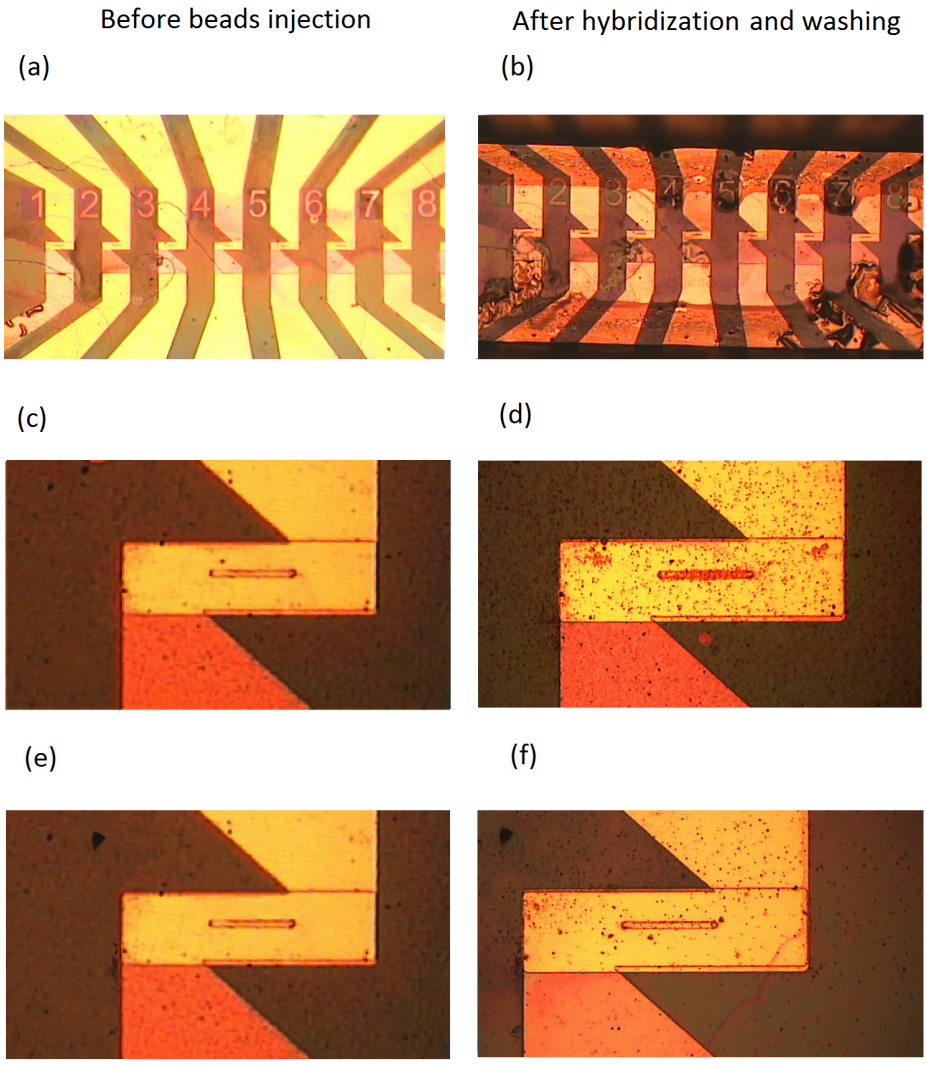

Figure 6.12: Microscope images before (on the left) and after (on the right) the molecular recognition experiment of synthetic DNA: (a), (b) bio-functionalized sensor chip; (c), (d) positive sensor; (e), (f) control sensor.

6.2.3 Molecular recognition of Hepatitis E virus

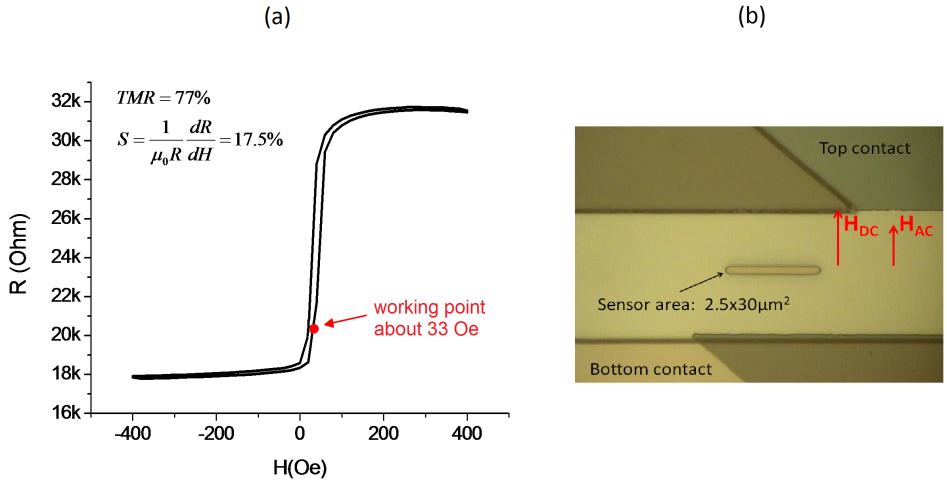

Figure 6.13: (a) Sensor response to the external magnetic field (R(H)). (b) Optical microscope image of the MTJ-based sensor, the sensing direction (i.e. the direction of the applied magnetic field) is shown.

Before starting with the experiment, the sensors surface has been bio- functionalized, using the same procedure of section 6.1 (probe DNA: 100 bp, 20 μM, amplified target DNA: 9 ng/μL corresponding to 275 nM). The spotting procedure has involved only the sensors 1-3 in fig. 6.15 (a), in order to use the other ones as controls.
The device used in this experiment is the Sample 3 of table 5.3. In figure 6.13 (a) the transfer curve R(H) of one sensor is reported (it shows a resistance of about 18 $k\Omega$ in the low state, a tunnelling magnetoresistance of 77% and a sensitivity S = 17.5 %/mT in the linear region).
The parameters set for the double modulation detection are described below:

- V_{in} = 100mV, modulated at frequency f_1 = 1.101kHz
- H_{AC} = 7 Oe, modulated at frequency f_2 = 39Hz
- H_{DC} = 33 Oe

The results of the experiment are summarized in figure 6.14, showing the signals coming from a positive sensor (a) and a control sensor (b), as a function of time. The beads (3mg/mL solution of magnetic beads, diluited

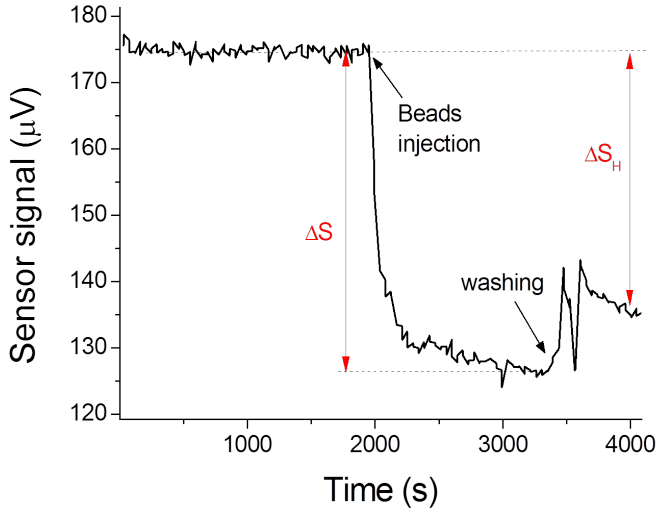

(a)

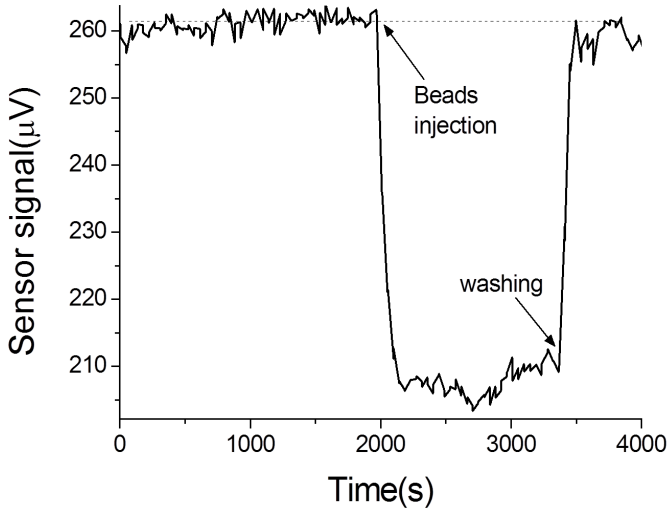

(b)

Figure 6.14: (a), (b) Sensor and control signals, respectively, as a function of time: bead injection is around t = 2000 s, washing is around t = 3400 s.

in PB-Tween) have been injected into the microfluidic cell at a rate of 50 μL/min, and, after sedimentation and biotin/streptavidin interaction, have been washed at a rate of 450 μL/min, till the control signal recovers completely the baseline (fig. 6.14 (b)). In figure 6.14 (a) the difference between

the two baselines, before beads insertion and after the washing step, gives a signal $\Delta S_H \approx 40\mu V$ related to the concentration of target DNA in the spotted sensor. After normalizing to the sedimentation signal ΔS, the binding signal $\Delta S_H/\Delta S$ results $\approx 0.8 \pm 0.01$. The limit of detection (LOD) has been estimated to be 0.014.

In figure 6.15 (a-f) the optical microscope images of the sample, before and after the experiment, are shown. As expected, only in correspondence of the spotted sensors there is a great concentration of beads, as it can be seen in figure 6.15 (b) that shows the first three sensors covered by a big brown spot of beads. In the two figures 6.15 (c) and 6.15 (d) the zoomed images of a spotted sensor before and after the molecular recognition are compared. The beads are accumulated within and outside the sensor area, and are arranged aligning with the direction of the magnetic field. This is a proof of the focusing action of the sensor stray field that promotes the beads sedimentation and the biotin-streptavidin hybridization. Compared to the study carried out in section 6.1, the current result clearly demonstrates that the process of hybridization is much more efficient when it takes place in a controlled microfluidic system.

Finally the optical microscope images of figure 6.15 (e) and (f), showing a zoom of a reference sensor, confirm that the washing has been effective in removing all the unspecific bounds, since no residual beads are present over the sensor surface: the sensor and the surrounding area are the same color, both before and after the experiment.

The results obtained are very satisfactory in comparison with previous works carried out by this group [3]. These improvements can be attributed to the different sensor's structure used in this thesis with respect to the reference [3]. Indeed here the junction pillar results to be higher, resulting in a non-planar system. Since the magnetic particle position over a magnetoresistive sensor directly depends on the sensor structure influencing the overall signal, in this case the non-planarity of the system allow to reduce the fringe field produced by the particles outside of the sensor. These would contribute in opposite way with respect to the beads over the sensors, reducing the overall signal. Moreover, since the sensed magnetic field increases as the magnetic particle is closer to the free layer, a stronger magnetic attraction of the beads could be attributable to the thinner capping layer used during this work compared to the reference [3].

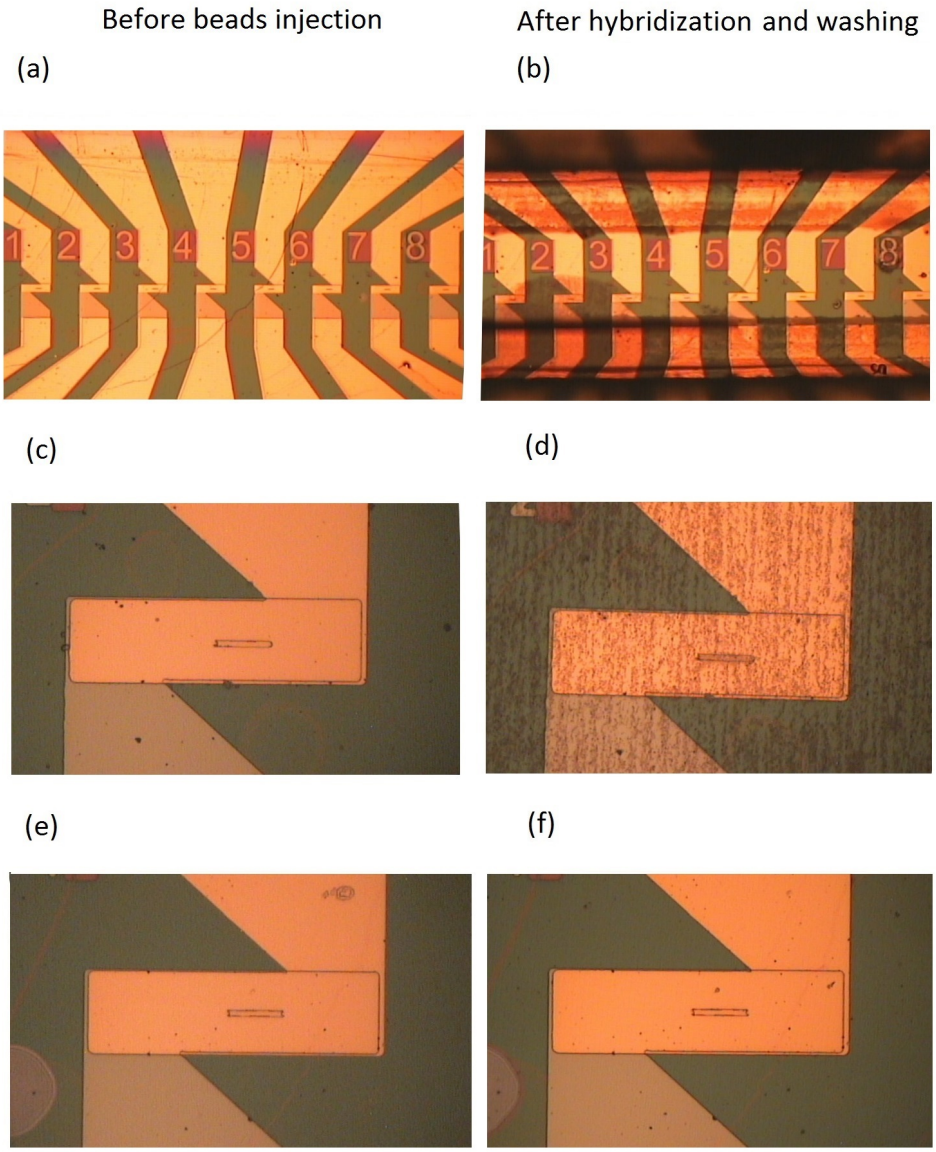

Figure 6.15: Microscope images before (on the left) and after (on the right) the molecular recognition experiment of HEV virus: (a), (b) bio-functionalized sensor chip; (c), (d) positive sensor; (e), (f) control sensor.

6.3 Summary

In this final chapter the results of the biological experiments carried out during the thesis work have been presented.
The first part of the chapter has dealt with the study of surfaces functionalized with three types of pathogen DNA: Enterobacter faecalis, Hepatitis E (HEV) and Aureus. The samples surface has been spotted with the DNA and then magnetic beads have been bound to the surface thanks to biotin-streptavidin binding. While the experiments with Enterobacter and Aureus have shown a low distribution of magnetic nanoparticles inside the spots and the necessity of optimizing the washing step to remove all the unbound beads from the surface, better results have been obtained with the HEV virus. For this reason the first experiment of molecular recognition has been carried out with this kind of DNA.
In the second section, after the preliminary experiments of beads detection and molecular recognition of synthetic DNA, the experiment performed with the HEV virus, is presented, showing a remarkable achievement in the current state of the art. This is the most important result of this thesis work, since it has demonstrated the application of the MTJ sensors fabricated at LNESS in a real biological system. The next step, currently under development, is to demonstrate the hybridization between the probe and target strands of natural DNA out of a chemical lab, in the microfluidic cell.
The future perspective is to perform multi-target analysis and further experiments with different concentrations of pathogen DNA, in order to calibrate the system before the realization of the final platform. It is worth noting that during this thesis work only a single experiment of molecular recognition has been carried out, mainly because of the difficulty of obtaining the biochemical material, which is typically an issue, because of the complexity of the required treatment (extraction and purification of the pathogen nucleic acids and the PCR amplification of the identified target sequences).

Conclusions and perspectives

This thesis work has dealt with the realization of an on-chip magnetic-based platform for diagnostic. Easy-to-use portable lab-on-a-chip devices are expected to take over many of today's standard laboratory tasks in biomedicine. The requirements for these devices are sensitivity, portability, rapidity, low cost and user-friendliness, and by combining magnetic labels with magnetoresistive sensing technology, it is possible to fulfill all these conditions.
The prototype of the diagnostic tool has been designed during this thesis, and the main components of the platform have been developed. A step towards portability has been achieved by integrating the magnetoresistive biochip in a portable electronic platform, which performs the control and acquisition of the signals generated by the sensors.
Some important achievements have been obtained during this research work. The first concerns the optimization process of the sensors' structure and dimensions, which has led to achieve better performances with respect to previous works performed by this group. These are related to the following aspects:

- Higher repeatability and reliability of the developed devices, with a fabrication yield of 85%
- Higher TMR ratio (up to 90%)
- Reduction of the sensor noise
- Better linearization of the sensors' response.

The second important result concerns the biological experiments. For the first time in the current state of the art, MTJ based sensors have been successfully tested in a molecular recognition experiment with natural pathogen DNA (HEV virus, 275 nM). Relatively little work exists in literature on DNA

based biosensors, and the most important results have been obtained with giant magnetoresistive (GMR) sensors [117] [70]. Despite the higher sensitivity of the TMR at low magnetic field, GMR devices have been proved to be most suitable for this type of applications, for their robustness, better temperature stability and fluid resistance. This thesis work, on the contrary, has demonstrated the capabilities of MTJs and their application in a real biological problem, allowing to exploit the higher performances in term of sensitivity of these devices with respect to the current state of the art of magnetoresistive sensors.

The importance of the obtained result lies in the difficulty of the experiment, mainly related to the steric hindrance of natural DNA, in this case 100 bp, which is a potential disadvantage for the hybridization process with the magnetic beads. Reduced binding capacity for large DNA fragments is the main issue for an experiment of biomolecular recognition. Indeed, due to the tendency of long DNA strands to curl, it might be possible that the region of the capture probe, labeled with the biotin, is less available for the streptavidin-coated bead surface, resulting in a poor interaction with the magnetic microbeads. Indeed the next challenging step in this work will be to carry out experiments with longer DNA strands, such as *Listeria monocytogenes*.

The future perspectives are related to the fine optimization of the system in order to obtain multi-target analysis, and the subsequent integration of the sensors in the final platform, in which all the functionalities required for the assay will be integrated allowing point-of-care testing. The final step will be to carry out field-tests at a lab or agrifood industry.

To conclude, a further optimization of the sensors could be carried out in view of other applications such as magnetic platform for neuronal activity sensing, in which high sensitivity is necessary for the detection of low magnetic fields down to picoTesla [21].

Bibliography

[1] In: *Advanced Healthcare Materials* 2 (2003), pp. 43–56.

[2] In: *Chemical Society Reviews* 42(8) (2013), pp. 3185, 3194.

[3] E. Albisetti et al. "Conditions for efficient on-chip magnetic bead detection via magnetoresistive sensors." In: *Biosensors and Bioelectronics* 47 (2013), pp. 213–217.

[4] E. Albisetti et al. "Photolithographic bio-patterning of magnetic sensors for biomolecular recognition." In: Submitted for consideration to *Lab on a chip* (2013).

[5] E. Albisetti. "Spintronic transducers based on magnetic tunnel junctions for biomolecular recognition." Tesi di laurea magistrale. Politecnico di Milano, 2010.

[6] F.G. Aliev et al. "Very low 1/f noise at room temperature in fully epitaxial Fe/MgO/Fe magnetic tunnel junctions." In: *Applied Physics Letters* 91 (2007), p. 232504.

[7] J.M. Almeida et al. "Low-frequency noise in MgO magnetic tunnel junctions: Hooge's Parameter Dependence on Bias Voltage." In: *IEEE Transactions on Magnetics* 44 (2008), p. 2569.

[8] T. Arakawa et al. "Sub-Poissonian shot noise in CoFeB/MgO/CoFeB-based magnetic tunneling junctions." In: *Applied Physics Letters* 98 (2011), p. 202103.

[9] P. Arbault et al. "Study of an ELISA method for the detection of E. coli O157 in food." In: *Progress in biotechnology* 17 (2000), pp. 359–368.

[10] A. Barry et al. "A CrO2-based magnetic tunnel junction." In: *Journal of Physics: Condensed Matter* 12(8) (2000), p. L173.

[11] D.R. Baselt et al. "A biosensor based on magnetoresistance technology." In: *biosensors and Bioelectronics* 13 (1998), pp. 731–739.

[12] G.S.D. Beach et al. "High resistivity of soft magnetic thin films using CoFe metal/native oxide multilayers (invited)." In: *Intl. Conf. Proc. San Francisco California* (2005), pp. 791–801.

[13] P.A. Besse et al. "Detection of a single magnetic microbead using a miniaturized silicon Hall sensor." In: *Applied Physics Letters* 80 (2002), pp. 4199–4201.

[14] J.A.C. Bland and B. Heinrich. *Ultrathin Magnetic Structures III*. 2005.

[15] A.M. Bratkovsky. "Assisted tunneling in ferromagnetic junctions and half-metallic oxides." In: *Applied Physics Letters* 72 (1997), p. 2334.

[16] A.M Bratkovsky. "Tunneling of electrons in conventional and half-metallic systems: Towards very large magnetoresistance." In: *Physical Review B* 56 (1997), p. 2344.

[17] P. Bruno. "Theory of interlayer magnetic coupling." In: *Physical Review B* 52(1) (1995), 411–439.

[18] P. Bruno and C. Chappert. "Oscillatory coupling between ferromagnetic layers separated by a nonmagnetic metal spacer." In: *Physical review letters* 67(12) (1991), 1602–1605.

[19] B. Cappella and G. Dietler. *Force-distance curves by atomic force microscopy*. Vol. 34. 1999, pp. 1–104.

[20] F.A. Cardoso. "Design, optimization and integration of magnetoresistive biochips." Ph.D. thesis. Instituto Superior Técnico, Lisbon, Portugal, 2011.

[21] R.M.d.C. Chaves. "PicoTesla Magnetoresistive Sensor and Single Bead Actuation and Detection On-Chip Platform." Ph.D. thesis. Universidade Técnica de Lisboa Instituto Superior Técnico, 2012.

[22] Y.S. Choi et al. "Transmission electron microscopy study on the polycrystalline CoFeB/MgO/CoFeB based magnetic tunnel junction showing a high tunneling magnetoresistance, predicted in single crystal magnetic tunnel junction." In: *Journal of Applied Physics* 101 (2007), p. 013907.

[23] D. Craik. *Magnetism: Principles and applications*. 1995.

[24] C.D. Damsgaard et al. "Theoretical study of in-plane response of magnetic field sensor to magnetic beads in an in-plane homogeneous field." In: *Journal of Applied Physics* 103 (2008), p. 6.

[25] R. De Palma et al. "Magnetic partcles as labels in bioassays: interactions between a biotinylated gold substrate and streptavidin magnetic particles." In: *The Journal of Physical Chemistry* 111(33) (2007), pp. 12227–12235.

[26] Z. Diao et al. "Reduced low frequency noise in electron beam evaporated MgO magnetic tunnel junctions." In: *Applied Physics Letters* 96 (2010), p. 202506.

[27] D.D. Djayaprawira et al. "230% room-temperature magnetoresistance in CoFeB/MgO/CoFeB magnetic tunnel junctions." In: *Applied Physics Letters* 86 (2005), p. 092502.

[28] M. Donolato et al. "On-chip measurement of the Brownian relaxation frequency of magnetic beads using magnetic tunneling junctions." In: *Applied Physics Letters* 98 (2011), p. 073702.

[29] V. Drewello et al. "Evidence for strong magnon contribution to the TMR temperature dependence in MgO based tunnel junctions." In: *Physical Review B* 77 (2008), p. 014440.

[30] B.R. Eggins. *Chemical Sensors and Biosensors*. 2002.

[31] L. Fasoli et al. "Spectrum analyzer with noise reduction by cross-correlation technique on two channels." In: *Review Of Scientific Instruments 70* 5 (1999), pp. 2520–2525.

[32] H.A. Ferreira et al. "Effect of spin-valve sensor magnetostatic fields on nanobead detection for biochip applications." In: *Journal of Applied Physics* 97 (2005), p. 10.

[33] F. Fixe et al. "An on-chip thin film photodetector for the quantification of DNA probes and targets in microarrays." In: *Nucleic Acids Research* 32 (2004), p. 70.

[34] A. Fogliani. "Progettazione di un elettromagnete nell'ambito del progetto Locsens." Tesi di laurea triennale. Politecnico di Milano, 2013.

[35] P.P. Freitas et al. "1/f noise in linearized low resistance MgO magnetic tunnel junctions." In: *Journal of Applied Physics* 99 (2006), 08B314.

[36] P.P. Freitas et al. "Spin valve sensors." In: *Sensors and Actuators A: Physical* 81 (2000), pp. 2–8.

[37] T. Geng et al. "Detection of low levels of *Listeria monocytogenes* cells by using a fiber-optic immunosensor." In: *Applied and Enviromental Microbiology* 70 (2004), pp. 6138–6146.

[38] W.A. Geoffrey et al. "Spin-Valve Thermal Stability: Interdiffusion versus Exchange Biasing." In: *IEEE Transactions On Magnetics* 36 (2000), p. 5.

[39] P.K. George. "Shot noise in low resistance magnetic tunnel junctions." In: *Applied Physics Letters* 80 (2002), p. 682.

[40] G. Gervasoni. "Progetto e realizzazione di uno strumento a doppio lock-in per la rivelazione in tempo reale di beads magnetiche." Tesi di laurea magistrale. Politecnico di Milano, 2013.

[41] A.L. Ghindilis et al. "CombiMatrix oligonucleotide arrays: Genotyping and gene expression assays employing electrochemical detection." In: *biosensors and Bioelectronics* 22 (2007), pp. 1853–1860.

[42] D. Graham et al. "Magnetoresistive-based biosensors and biochips." In: *TRENDS in Biotechnology* 22 (2004), p. 9.

[43] D.L. Graham et al. "Single magnetic microsphere placement and detection on-chip using current line designs with integrated spin valve sensors: Biotechnological applications." In: *Journal of Applied Physics* 91 (2002), pp. 7786–7788.

[44] P. Grünberg et al. "Layered Magnetic Structures: Evidence for Antiferromagnetic Coupling of Fe Layers across Cr Interlayers." In: *Physical Review Letters* 57(19) (1986), 2442–2445.

[45] R. Guerrero et al. "Low-frequency noise and tunneling magnetoresistance in Fe(110)/MgO(111)/Fe(110) epitaxial magnetic tunnel junctions." In: *Applied Physics Letters* 87 (2005), p. 042501.

[46] R. Guntupalli et al. "A magnetoelastic resonance biosensor immobilized with polyclonal antibody for the detection of *Salmonella typhimurium*." In: *Biosensors and Bioelectronics* 22 (2007), pp. 1474–1479.

[47] S.-J. Han et al. "Giant magnetoresistive biochip for DNA detection and HPV genotyping." In: *Biosensors and Bioelectronics* 24 (2008), pp. 99–103.

[48] T.B.G. Hansen et al. "Theoretical study of in-plane response of magnetic field sensor to magnetic beads magnetized by the sensor self-field." In: *Journal of Applied Physics* 107 (2010), p. 124511.

[49] U. Hardman. *Magnetic Thin Film and Multilayer Systems: Physics, Analysis and Industrial Applications*. 1996.

[50] G. Harsanyi. *Sensors in Biomedical Applications: Fundamentals, Technology and Applications*. 2000.

[51] J. Hayakawa et al. "Dependence of Giant Tunnel Magnetoresistance of Sputtered CoFeB/MgO/CoFeB Magnetic Tunnel Junctions on MgO Barrier Thickness and Annealing Temperature." In: *Japanese Journal of Applied Physics* 44 (2005), p. 19.

[52] J. Hayakawa et al. "Effect of high annealing temperature on giant tunnel magnetoresistance ratio of CoFeB/MgO/CoFeB magnetic tunnel junctions." In: *Applied Physics Letters* 89 (2006), p. 232510.

[53] D.E. Helm and S.S. Parkin. "Magnetoresistive spin valve sensor with improved pinned ferromagnetic layer and magnetic recording system using the sensor." In: *US Patent* 5465185 (1995).

[54] R.E. Herbert and T. Hesjedal. "Calculation of the magnetic stray field of a uniaxial magnetic domain." In: *Journal of Applied Physics* 97 (2005), p. 074504.

[55] A. Hierlemann et al. "Microfabrication techniques for chemical/ biosensors." In: *Proceedings of the IEEE* 91 (2003), pp. 893–863.

[56] F.N. Hooge. "1/f Noise." In: *Physica B* 83 (1976), p. 14.

[57] F.N. Hooge. "1/f Noise is no surface effect." In: *Physics Letters A* 29 (1969), p. 139.

[58] T. Ibusuki et al. "Lower-temperature crystallization of CoFeB in MgO magnetic tunnel junctions by using Ti capping layer." In: *Applied Physics Letters* 94 (2009), p. 062509.

[59] S. Ikeda et al. "Tunnel magnetoresistance of 604% at 300K by suppression of Ta diffusion in CoFeB/MgO/CoFeB pseudo-spin-valves annealed at high temperature." In: *Physics Letters* 93 (2008), p. 082508.

[60] AJA international. *What is sputtering?* URL: http://www.ajaint.com/whatis.htm.

[61] Y. Jang et al. "Magnetic field sensing scheme using CoFeB/MgO/CoFeB tunneling junction with superparamagnetic CoFeB layer." In: *Applied Physics Letters* 89 (2006), p. 163119.

[62] J.B. Johnson. "Thermal agitation of electricity in conductors." In: *Physical Review* 32 (1928), p. 97.

[63] M. Jullièere. "Tunneling between ferromagnetic films." In: *Physics Letters A* 54 (1975), p. 225.

[64] J.C.S. Kools et al. "Effect of finite magnetic film thickness on Néel coupling in spin valves." In: *Journal of Applied Physics* 85 (1999), p. 4466.

[65] K.M. Krishnan. 2010. URL: http://www.magneticmicrosphere.com/Kannan_nanomagnetics_review_2010.pdf.

[66] K. Kriz et al. "Advancements toward magneto immunoassays." In: *biosensors and Bioelectronics* 13 (1998), pp. 817–823.

[67] P. Leonard et al. "Advances in biosensors for detection of pathogens in food and water." In: *Enzyme and Microbial Technology* 32 (2003), pp. 3–13.

[68] H.Y. Li et al. "Asymmetrical dependence of exchange coupling in synthetic antiferromagnets FeMn/Co/Ru/Co on the ferromagnetic layer thickness." In: *Physica Status Solidi (a)* 191 (2002), pp. 583–589.

[69] Yu Lu et al. "Shape-anisotropy-controlled magnetoresistive response in magnetic tunnel junctions." In: *Applied Physics Letters* 70 (1997), p. 2610.

[70] V.C. Martins et al. "Femtomolar Limit of Detection with a Magnetoresistive Biochip." In: *biosensors and Bioelectronics* 24 (2009), p. 2690.

[71] Van der Merwe P. "Surface Plasmon Resonance." In: *Available from http://users.path.ox.ac.uk/ vdmerwe/Internal/spr.PDF* (2011).

[72] R. Meservey and P.M. Tedrow. "Spin-polarized electron tunneling." In: *Physics Reports* 238 (1994), p. 173.

[73] R.L. Millen et al. "Giant magnetoresistive sensors and superparamagnetic nanoparticles: a chip-scale detection strategy for immunosorbent assays." In: *Analytical Chemistry* 77(20) (2005), pp. 6581–6587.

[74] M.M. Miller et al. "A DNA array sensor utilizing magnetic microbeads and magnetoelectronic detection." In: *Journal of Magnetism and Magnetic Materials* 225 (2001), pp. 138–144.

[75] M.M. Miller et al. "Detection of a micron-sized magnetic sphere using a ring-shaped anisotropic magnetoresistance-based sensor: a model for a magnetoresistance-based biosensor." In: *Applied Physics Letters* 81 (2002), pp. 2211–2213.

[76] J.S. Moodera and G. Mathon. "Spin polarized tunneling in ferromagnetic junctions." In: *Journal of Magnetism and Magnetic Materials* 200 (1999), 248–273.

[77] J. Musil and M. Misina. "Low pressure radio frequency and microwave discharges for d.c. sputtering of ferromagnetic materials." In: *Czechoslovak Journal of Physics* 50 (2000), p. 6.

[78] N. Néel. "On a new mode of coupling between the magnetizations of two thin ferromagnetic layers." In: 255 (1962), p. 1676.

[79] M. Ngoepe et al. "Integration of Biosensors and Drug Delivery Technologies for Early Detection and Chronic Management of Illness." In: *Sensors* 13 (2013), pp. 7680–7713.

[80] L.B. Nie et al. "Enhanced DNA detection based on the amplification of gold nanoparticles using quartz crystal microbalance." In: *Nanotechnology* 18 (2007), p. 305501.

[81] A.F.M. Nor et al. "Low-frequency noise in MgO magnetic tunnel junctions." In: *Journal of Applied Physics* 99 (2006), 08T306.

[82] H. Nyquist. "Thermal agitation of electric charge in conductors." In: *Physical Review* 32 (1928), p. 110.

[83] A. Ozbay et al. "Low frequency magnetoresistive noise in spin-valve structures." In: *Applied Physics Letters* 94 (2009), p. 202506.

[84] M. Ozsoz et al. "Electrochemical Genosensor Based on Colloidal Gold Nanoparticles for the Detection of Factor V Leiden Mutation Using Disposable Pencil Graphite Electrodes." In: *Analytica Chemistry* 75(9) (2003), pp. 2181–2187.

[85] S. S. Parkin et al. "Current-driven magnetization switching in CoFeB/ MgO /CoFeB magnetic tunnel junctions." In: *Nature Materials* 3 (2004), p. 862.

[86] S.S.P. Parkin et al. "Oscillations in Exchange Coupling and Magnetoresistance in Metallic Superlattice Structures: Co/Ru, Co/Cr, and Fe/Cr." In: *Physical Review Letters* 64 (1989), p. 19.

[87] S.S.P. Parkin et al. "Oscillations in exchange coupling and magnetoresistance in metallic superlattice structures: Co/Ru, Co/Cr, and Fe/Cr." In: *Physical Review Letters* 64(19) (1990), 2304–2307.

[88] D. Petti et al. "Giant tunneling magnetoresistance effect in low resistance CoFeB/MgO(001)/CoFeB magnetic tunnel junctions for readhead applications." In: *Applied Physics Letters* 87 (2005), p. 072503.

[89] D. Petti et al. "Optimization of the bio-functionalized area of magnetic biosensors." In: *The European Physical Journal B* 86 (2013), p. 261.

[90] D. Petti et al. "Storing magnetic information in IrMn/MgO/Ta tunnel junctions via field-cooling." In: *Applied Physics Letters* 102 (2013), p. 19.

[91] Daniela Petti. "Magnetic Tunneling Junctions for biosensors: From the growth to the detection." In: *Il Nuovo Cimento* 35C (2012), p. 5.

[92] G. Pirri et al. In: *Analytical Chemistry* 76 (2004), pp. 1352–1358.

[93] J. Richardson et al. "The use of coated paramagnetic particles as a physical label in a magneto-immunoassay." In: *biosensors and Bioelectronics* 16 (2001), pp. 9–12.

[94] K.J. Ryan and C.G. Ray. *Sherris Medical Microbiology.* 2004.

[95] M. Sampietro et al. "Correlation spectrum analyzer for direct measurement of device current noise." In: *Review Of Scientific Instruments 73* 7 (2002), pp. 2717–2723.

[96] W. Schottky. "Small-shot effect and flicker effect." In: *Physical Review* 28 (1926), p. 74.

[97] W. Schottky. "Uber spontane stromschwankungen in verschiedenen elektrizittsleitern." In: *Annals of Physics* 23 (1918), p. 541.

[98] K. Sekiguchi et al. "Observation of full shot noise in CoFeB / MgO / CoFeB-based magnetic tunneling junctions." In: *Applied Physics Letters* 96 (2010), p. 252504.

[99] L. Serna-Cock and J.G. Perenguez-Verdugo. *Environmental Biosensors*. 2011.

[100] K. Shimazawa et al. "Evaluation of front flux guide-type magnetic tunnel junction heads." In: *IEEE Transactions On Magnetics* 36 (2000), p. 2542.

[101] K. Shimazawa et al. "Frequency response of common lead and shield type magnetic tunneling junction head." In: *IEEE Transactions On Magnetics* 37 (2001), p. 1684.

[102] J.G. Simmons. "Generalized Formula for the Electric Tunnel Effect between Similar Electrodes Separated by a Thin Insulating Film." In: *Journal of Applied Physics* 34 (1963), p. 1793.

[103] W. Skowronski et al. "Interlayer exchange coupling and current induced magnetization switching in magnetic tunnel junctions with MgO wedge barrier." In: *Journal of Applied Physics* 107 (2010), p. 093917.

[104] J.C. Slonczewski. "Conductance and exchange coupling of two ferromagnets separated by a tunneling barrier." In: *Physical Review B* 39 (1989), 6995–7002.

[105] N. Smith and P. Arnett. "White-noise magnetization fluctuations in magnetoresistive heads." In: *Applied Physics Letters* 78 (2001), p. 1448.

[106] L. Sola et al. In: *Journal of Chromatography A* 1270 (2012), pp. 324–329.

[107] V.P. Srinivas et al. "Exchange Coupling Control and Thermal Endurance of Synthetic Antiferromagnet Structures for MRAM." In: *IEEE Transactions On Magnetics* 40 (2004), p. 4.

[108] M.D. Stiles. "Exchange coupling in magnetic heterostructures." In: *Physical Review B* 48 (1993), p. 10.

[109] G.J. Strijkers et al. "Magnetic characterization and modeling of FeMn/ Co/ Ru/ Co artificial antiferromagnets." In: *Physical Review B* 62 (2000), p. 21.

[110] M. Su et al. "Microcantilever resonance-based DNA detection with nanoparticle probes." In: *Applied Physics Letters* 82 (2003), pp. 3562–3564.

[111] S. Swann. "Magnetron sputtering." In: *Physics in Technology* 19 (1988), p. 67.

[112] F.R.R. Teles and L.P. Fonseca. "Trends in DNA biosensors." In: *Talanta* 77 (2008), pp. 606–623.

[113] L.A. Terry et al. "The Application of Biosensors to Fresh Produce and the Wider Food Industry." In: *Journal of Agricultural and Food Chemistry* 53 (2005), pp. 1309–1316.

[114] J. Unguris et al. "Oscillatory exchange coupling in Fe/Au/Fe(100)." In: *Journal of Applied Physics* 75 (1994), p. 6437.

[115] H.A.M. Van Der Berg et al. "GMR sensor scheme with artificial antiferromagnetic subsystem." In: *IEEE Transactions on Magnetics* 32 (1996), p. 4624.

[116] J. Wang et al. "Particle-based detection of DNA hybridization using electrochemical stripping measurements of an iron tracer." In: *Analytica Chimica Acta* 482 (2003), pp. 149–155.

[117] S. X. Wang et al. "Quantification of protein interactions and solution transport using high-density GMR sensor arrays." In: *Nature Nanotechnology* 6 (2011), p. 314.

[118] S.X. Wang et al. "nanoLAB: An ultraportable, handheld diagnostic laboratory for global health." In: *The Royal Society of Chemistry* (2011).

[119] M.B. Weissman. "1/f noise and other slow, nonexponential kinetics in condensed matter." In: *Review of Modern Physics* 60 (1988), p. 537.

[120] P. Wisniowski et al. "Effect of free layer thickness and shape anisotropy on the transfer curves of MgO magnetic tunnel junctions." In: *Journal of Applied Physics* 103 (2008), 07A910.

[121] P. Wisniowski et al. "Influence of buffer layer texture on magnetic and electrical properties of IrMn spin valve magnetic tunnel junctions." In: *Journal of Applied Physics* 100 (2006), p. 013906.

[122] L. Xu et al. "Giant magnetoresistive biochip for DNA detection and HPV genotyping." In: *Biosensors and Bioelectronics* 24 (2008), pp. 99–103.

[123] L. Xu et al. "Giant magnetoresistive sensors for DNA microarray." In: *IEEE Transactions on Magnetics* 44(11) (2008), pp. 3989–3991.

[124] C.-Y. You and S.C. Shin. "Generalized analytic formulae for magnetooptical Kerr effects." In: *Journal of Applied Physics* 84.1 (1998), pp. 541–546.

[125] S. Yuasa et al. "Giant room-temperature magnetoresistance in single-crystal Fe/MgO/Fe magnetic tunnel junctions." In: *Nature Materials* 3 (2004), pp. 868–871.

[126] J. Zhang and R.M. White. "Topological coupling in spin valve type multilayers." In: *IEEE Transactions on Magnetics* 32(5) (1996), 4630 – 4635.

[127] J. Zhang and R.M White. "Voltage dependence of magnetoresistance in spin dependent tunneling junctions." In: *Journal of Applied Physics* 83 (1998), p. 6512.

[128] S. Zhang et al. "Quenching of magnetoresistance by hot electrons in magnetic tunnel junctions." In: *Physical Review Letters* 79 (1997), p. 3744.

[129] X. Zhang et al. "Spin-polarized tunneling and magnetoresistance in ferromagnet/insulator(semiconductor) single and double tunnel junctions subjected to an electric field." In: *Physical Review B* 56 (1997), p. 5484.